

Award Number: W81XWH-12-1-0074

TITLE: Dissecting and Targeting Latent Metastasis

PRINCIPAL INVESTIGATOR: Joan Massagué, PhD

CONTRACTING ORGANIZATION: Sloan Kettering Institute for Cancer Research
New York, NY 10065

REPORT DATE: September 2015

TYPE OF REPORT: Annual

PREPARED FOR: U.S. Army Medical Research and Materiel Command
Fort Detrick, Maryland 21702-5012

DISTRIBUTION STATEMENT: Approved for Public Release;
Distribution Unlimited

The views, opinions and/or findings contained in this report are those of the author(s) and should not be construed as an official Department of the Army position, policy or decision unless so designated by other documentation.

REPORT DOCUMENTATION PAGE

Form Approved
OMB No. 0704-0188

Public reporting burden for this collection of information is estimated to average 1 hour per response, including the time for reviewing instructions, searching existing data sources, gathering and maintaining the data needed, and completing and reviewing this collection of information. Send comments regarding this burden estimate or any other aspect of this collection of information, including suggestions for reducing this burden to Department of Defense, Washington Headquarters Services, Directorate for Information Operations and Reports (0704-0188), 1215 Jefferson Davis Highway, Suite 1204, Arlington, VA 22202-4302. Respondents should be aware that notwithstanding any other provision of law, no person shall be subject to any penalty for failing to comply with a collection of information if it does not display a currently valid OMB control number. **PLEASE DO NOT RETURN YOUR FORM TO THE ABOVE ADDRESS.**

1. REPORT DATE September 2015			2. REPORT TYPE Annual		3. DATES COVERED 09/01/2014-08/31/2015
4. TITLE AND SUBTITLE Dissecting and Targeting Latent Metastasis					5a. CONTRACT NUMBER W81XWH-12-1-0074
					5b. GRANT NUMBER BC112391
					5c. PROGRAM ELEMENT NUMBER
6. AUTHOR(S) Joan Massagué, PhD E-Mail: j-massague@ski.mskcc.org					5d. PROJECT NUMBER
					5e. TASK NUMBER
					5f. WORK UNIT NUMBER
7. PERFORMING ORGANIZATION NAME(S) AND ADDRESS(ES) Sloan Kettering Institute for Cancer Research New York, NY 10065					8. PERFORMING ORGANIZATION REPORT NUMBER
9. SPONSORING / MONITORING AGENCY NAME(S) AND ADDRESS(ES) U.S. Army Medical Research and Materiel Command Fort Detrick, Maryland 21702-5012					10. SPONSOR/MONITOR'S ACRONYM(S)
					11. SPONSOR/MONITOR'S REPORT NUMBER(S)
12. DISTRIBUTION / AVAILABILITY STATEMENT Approved for Public Release; Distribution Unlimited					
13. SUPPLEMENTARY NOTES					
14. ABSTRACT Award DOD W81XWH-12-1-0074 is designed to address this problem. In Year 01 of this award, we developed models of latent metastasis of breast cancer and lung cancer. We isolated latency competent cancer (LCC) cells by <i>in vivo</i> selection of early-stage human tumor cell populations in mice. In Year 02, we investigated the metastatic properties of these models. In parallel, we discovered the roles of Serpins and L1CAM in the early seeding of the brain and other organs by breast cancer cells. In Year 03 of this award, we have achieved the first level of completion of the tasks set forth in our DOD W81XWH-12-1-0074 application. We have used our newly developed models of metastatic latency to show that LCC cells are a distinct class of stem-like cancer cells, which primed to enter quiescence and evade innate immunity after infiltrating distant organs. LCC cells express SOX transcription factors that impart tumor-initiating stem/progenitor cell identity. It has been long believed that dormant DTCs enter quiescence by the action of growth inhibitory signals from the host stroma. However, organs that host DTCs support cell proliferation as part of normal tissue homeostasis and regenerative processes, raising questions as to whether growth inhibitory signals from the stroma alone could explain latent metastasis. Indeed, our work shows that LCC cells actively enter a slow-cycling state by producing DKK1, an inhibitor of the stem cell growth factor WNT, leading to withdrawal and the cells from the proliferative cycle. The WNT signaling pathway is a key driver of proliferation of stem and progenitor cells, both normal and neoplastic. Moreover, we show that this self-imposed slow-cycling state involves the downregulation of ULBP ligands and other activators of natural killer (NK) lymphocytes, thus leading to evasion of NK cell-mediated cancer cell clearance. By expressing a Sox-dependent stem-like state and actively silencing WNT signaling, LCC cells can enter quiescence and evade innate immunity to remain latent for extended periods. These findings raise the possibility of eliminating latent metastatic disease by reactivating the expression of NK receptors in the cancer cells.					
15. SUBJECT TERMS Breast cancer; latent metastasis; disseminated cancer cells; circulating cancer cells; cancer stem cells; metastatic niche; SOX genes; WNT pathway; NK lymphocytes					
16. SECURITY CLASSIFICATION OF:			17. LIMITATION OF ABSTRACT UU	18. NUMBER OF PAGES -53	19a. NAME OF RESPONSIBLE PERSON USAMRMC
a. REPORT U	b. ABSTRACT U	c. THIS PAGE U			19b. TELEPHONE NUMBER (include area code)

CONGRESSIONALLY DIRECTED MEDICAL RESEARCH PROGRAM

Award DOD W81XWH-12-1-0074

Principal Investigator: Joan Massagué, PhD

ANNUAL REPORT

9/1/14 – 8/31/15

Table of Contents

	<u>Page</u>
Introduction.....	2
Keywords.....	2
Overall Project Summary.....	2
Key Research Accomplishments.....	10
Conclusion.....	10
Changes in Personnel.....	10
Publications, Abstracts, and Presentations.....	10
Inventions, Patents and Licenses.....	12
Reportable Outcomes.....	12
Other Achievements.....	12
References.....	13
Appendices.....	18

INTRODUCTION

Cancer patients with no clinical evidence of disease after the initial treatment frequently relapse with distant metastasis years later. Prior to diagnosis and treatment, primary tumors may release large numbers of cancer cells into the circulation. Although a majority of the dispersed cells perish in the bloodstream or soon after infiltrating distant organs, a minority may survive as latent seeds in host tissues (1). As a result, cancer patients who are clinically considered disease-free carry thousands of disseminated tumor cells (DTCs) in the bone marrow and other organs(2, 3). DTCs are frequently negative for proliferation markers, suggesting that they survive in a quiescent state that is resistant to cytotoxic adjuvant treatments(4, 5). Little is known about the nature of dormant DTCs and the mechanisms that allow them to remain quiescent, evade immunity, and retain tumor-initiating capacity. Latent metastasis therefore remains a largely unknown biological process as well as a major concern in the clinic, and very particularly in breast cancer.

Our ability to address these questions and to gain an urgently needed understanding of the molecular basis for latent metastasis have been limited by a scarcity of preclinical models that recapitulate key features of this metastatic stage, including a propensity of DTCs to enter proliferative quiescence, to survive long-term as quiescent DTCs, and to have a finite probability of initiating macrometastatic growth (6, 7). The goal of this innovative award is to address this important unmet need by dissecting and targeting the biology of latent metastasis.

KEYWORDS

Breast cancer; latent metastasis; disseminated cancer cells; circulating cancer cells; cancer stem cells; metastatic niche; SOX genes; WNT pathway; NK lymphocytes.

OVERALL PROJECT SUMMARY

Progress under Task 1: To develop experimental models of latent metastasis.

Progress Item 1.1. Latency competent cells isolated from early-stage breast and lung cancers. We isolated cancer cells that are competent to seed relevant organs with latent metastasis (latency competent cancer cells, LCC cells). As sources, we used cell lines derived from early-stage human breast and lung adenocarcinomas. The H2087 line was established from a stage I lung adenocarcinoma(8), and the HCC1954 line from a stage IIA HER2+ breast cancer (9). Nearly half of early-diagnosed (stage I and II) lung adenocarcinoma patients develop distant relapse despite surgical resection of the primary tumor, implying the presence of latent disseminated disease (10). The HER2+ breast cancer patient population is experiencing a marked increase in the incidence of brain metastasis after anti-HER2 targeted therapies that effectively suppress extracranial relapse and extend survival (11). Thus, both cancer types are important sources of latent metastasis in the clinic.

H2087 and HCC1954 cells transduced with a GFP-luciferase reporter and antibiotic resistance vectors were intracardially injected into the arterial circulation of *Foxn1^{tm1}* mice. The mutation in *Foxn1* renders the mice athymic, severely blunting the maturation of effector T cells but preserving innate immunity components including macrophages and NK cells (12). As monitored by bioluminescence imaging (BLI), the luciferase signal became undetectable 7 days

after inoculation, indicating extensive clearance of the cancer cells from the circulation or after organ infiltration. Most mice remained signal-free and healthy for 3 months. Organs from these mice were dissociated into single-cell suspensions in culture to recover antibiotic-resistant cancer cells. We were able to recover these cells from lung (H2087-LCC1) and kidney (H2087-LCC2) of mice injected with H2087, and from brain of mice injected with HCC1954 (HCC1954-LCC1). The tumorigenic activity of LCC cells after orthotopic implantation was similar to that of the parental populations. Thus, LCC cells retained tumor initiating potential after months of latency in mouse tissues.

Of 20 athymic mice injected with H2087-LCC cells, one developed overt metastasis, one developed a spinal metastasis after 4 months and did not progress, two developed incipient lesions after 7 months, and 16 remained free of detectable BLI signal for over 8 months (Figure 1A,C). Only 1 out of 8 mice injected with HCC1954-LCC1 developed overt metastasis, and the rest remained metastasis-free for over 4 months (Figure 1B-C). In comparison, aggressive metastatic lines that we previously isolated from late-stage human breast carcinoma (MDA-MB-231) and lung adenocarcinoma (H2030) formed extensive metastases within 3 weeks in all mice (13, 14).

We were able to histologically detect and recover cancer cells from 20 of 26 (77%) LCC-injected mice that remained metastasis-free, but only from 2/14 (14%) of mice injected with the parental lines. H2087-LCC1 and -LCC2 targeted both the lungs and the kidneys, suggesting that the latent phenotype of these cells was not strictly organ specific (Figure 1D-G). Cells isolated from rare macrometastatic tumors arising in LCC-injected mice (H2087-LCC-M and HCC1954-LCC-M lines) showed a latent phenotype upon reinjection, with no increase in macrometastatic activity, arguing that LCCs stochastically form overt metastases.

Progress Item 1.2. LCC cell localization in infiltrated organs. We chose H2087-LCC1, H2087-LCC2, HCC1954-LCC1, and the HCC1954-LCC2 line derived from LCC1 injected mice, for further analysis. Two weeks after inoculation, approximately 20% of disseminated GFP⁺ HCC1954 LCC cells in the brain were found in small clusters (>10 cells) and the rest as single cells. The proportion of cell clusters remained stable or progressively decreased over time. After 3 months, more than 90% of the DTCs were single cells and the rest were small clusters of approximately 20 cells, as determined by anti-GFP immunostaining (Figure 1D-E), H&E staining (Figure 1F), and human Vimentin immunostaining (Figure 1G). In the kidney, LCC cells were detected between the renal tubules, adjacent to capillaries, or within glomeruli (Figure 1F-G). A few LCC cells were observed within the adrenal gland cortex. In the lung, LCC cells were invariably found within the alveolar walls (Figure 1G). In the brain and other organs, LCC cells were closely associated with the vasculature (Figure 1D). Aggressive brain metastatic cells rapidly spread over the abluminal surface of microcapillaries, and this spreading is required for colony outgrowth (15). In contrast, LCC cells infiltrating the brain parenchyma spread along capillaries only transiently (days 1-3 after inoculation), and subsequently adopted a rounded morphology (Figure 1H-I).

Progress Item 1.3. LCC cell entry into quiescence. To monitor proliferation in the first days after inoculation, we labeled LCC cells with 5-ethynyl-2'-deoxyuridine (EdU) prior to intravenous injection into athymic mice (Figure 2A-B). Proliferation would dilute the amount of EdU retained in these cells. After 14 days, approximately 60% of LCC cells that reached the

lungs still retained EdU versus 15-25% in the parental populations (Figure 2C-D), indicating that LCC cells entered quiescence more readily. Three months after inoculation, approximately 90% of the H2087-LCC1 cells in lung and HCC1954-LCC1 cells in brain were negative for the proliferation marker Ki-67. Ki-67+ LCC cells detected were largely confined to cell clusters (Figure 2E-F). To determine the effect of a mitogen-poor environment we cultured LCC cells in mitogen-low media (MLM, 2% serum) or regular mitogen-rich media (MRM, 10% serum). Under MLM conditions, LCC cells underwent a rapid decrease in proliferation, as determined by dye retention (Figures 2G), whereas the parental line showed little (H2087) or no decrease (HCC1954) in proliferation. LCC cells accumulated with a G0/G1 DNA content (Figure 2H) and no change in apoptosis marker (cleaved caspase-3) levels.

Progress Item 1.4. Stem cell nature of LCC cells. Gene Set Enrichment Analysis of differentially expressed genes in HCC1954-LCC cells compared to parental HCC1954 identified a mammary stem cell signature (MaSC) as a top-scoring gene set, under both MLM and MRM conditions. Principal component analysis revealed strong clustering of HCC1954-LCC cells with human and mouse mammary stem and progenitor cells, away from mature luminal and stromal compartments (Figure 3A) (16). Parental HCC1954 clustered with the mature luminal compartment. Moreover, HCC1954-LCC cells were enriched for the surface marker profile CD44^{Hi}/CD24^{Lo}, which is typical of human breast cancer stem cells (Figure 3B) (17). Based on gene expression profiles associated with molecularly distinct cell types of the mouse lung epithelium (18), H2087-LCC cells clustered with the stem-like alveolar type I (AT1) and bipotent progenitor (BP) cells. Parental H2087 clustered with alveolar type II (AT2) and Clara cell lineages under MRM and MLM conditions, respectively, (Figure 3C). These results suggested that our LCC isolation protocol enriched for cancer cells with stem/progenitor cell markers.

In sum, LCC cells recapitulate key features of the latent metastatic state, including a propensity to enter proliferative quiescence, an ability to survive as latent entities in relevant organs for months, and to retain tumorigenic capacity and metastasis-initiating potential.

Progress under Task 2: Identify genes that are specifically active in latent metastatic cells.

Progress Item 2.1. Sox2 and Sox9 association with the LCC phenotype. Progenitor cell identity is determined by lineage-specific transcription factors (19). Notably, two master regulators of stem and progenitor cell identity, Sox2 (20) and Sox9 (21), ranked high among transcription factors whose expression was prominently associated with the LCC phenotype. Sox2 was predominant in H2087-LCC cells whereas HCC1954-LCC cells showed high Sox9 expression and low Sox2 expression (Figures 3D-E). Sox2 and Sox9 regulate stem and progenitor cells in adult tissues (19) and Sox2 mediates pluripotency reprogramming in differentiated cells (22). Both genes are implicated in cancer. Sox2 is genetically amplified in squamous carcinomas and small cell lung cancers (23, 24). Sox9 is upregulated in brain tumors and basal cell carcinomas (25), and confers stem cell phenotype to breast cancer cells (21). Analysis of TCGA datasets confirmed a high incidence of Sox2 and Sox9 genetic alterations (amplifications) in different tumor types, including breast and lung cancers.

Progress Item 2.2. Metastatic seeding by LCC cells requires Sox factors. We generated H2087 and HCC1954-LCC cell lines expressing shRNAs targeting *Sox2* and *Sox9* respectively.

Sox2 knockdown in H2087-LCC and Sox9 knockdown in HCC1954-LCC cells did not alter the growth rate of these cells in monolayer culture. We inoculated H2087-LCC cells into athymic mice by tail vein injection, and monitored mice by whole body BLI imaging weekly for 60 days. No BLI signal was detected during this time period or on sacrificing the mice and imaging lungs *ex vivo*. Further analysis of the lungs showed a marked decrease in the metastatic seeding capacity of Sox2 depleted H2087-LCC cells compared to cells expressing a control vector (Figure 3F). Similarly, Sox9 depleted HCC1954-LCC1 cells showed a marked decrease in the ability to seed the brain (Figure 3G). The ability of tumor-initiating cells to form colonies (oncospheres) in suspension provides a test of their capacity to initiate tumor growth under restrictive conditions (26). Parental H2087 and HCC1954 cells generated the same number of oncospheres as their LCC counterparts. Interestingly, Sox2 expression was enriched in H2087-LCC oncospheres, but not oncospheres formed by parental H2087 (Figure 3H). Sox2 knockdown inhibited oncosphere formation in H2087-LCC but not in parental (Figure 3I). Thus, LCC cells are distinct subpopulations of stem-like cancer cells characterized by high expression of Sox2 or Sox9 and a dependence on these transcription factors for growth under restrictive conditions *in vitro* and for seeding of latent metastasis in mice.

Progress under Task 3: Identification of key stromal components in latent metastasis.

Progress Item 3.1. Metastatic latency balanced by NK cell immune surveillance. Although LCC cells were superior at seeding various organs, they still suffered massive attrition in athymic mice. The elimination of disseminated cancer cells may be due to metabolic and mechanical stresses (6, 7), but also to immune surveillance (27-29). *Foxn1^{nu}* athymic mice retain functional NK cells and other components of the innate immune system, raising the possibility that immune surveillance restricts the expansion of LCC cells in these mice. To test this possibility, we inoculated LCC cells into NOD.Cg-*Prkdc^{scid}* *Il2rg^{tm1Wjl}*/SzJ mice (NOD/SCID Gamma, NSG mice), which are defective for both adaptive and innate immune responses (30). Strikingly, H2087-LCC and HCC1954-LCC cells gave rise to overt metastasis with high penetrance (Figure 4A-B) and in multiple organs in NSG mice (Figure 4C-D). These organs included the liver, a site normally rich in NK cells (31). To test the role of NK cells as candidate inhibitors of LCC expansion, we depleted athymic mice of NK cells by administration of polyclonal anti-asialo-GM1 antibody or the anti-NK1.1 monoclonal antibody PK136 (32, 33). Both NK cell depletion strategies resulted in permissive outgrowth of LCC cells, as manifested by a marked increase in whole body BLI signal, and in the ability to grow in the brain as shown by *ex vivo* brain imaging and quantification of average brain lesion size (Figures 4E-F). Similar results were observed upon NK cell depletion in mice injected with H2087-LCC2, which resulted in bone metastasis (Figures 4G).

Progress Item 3.2. NK cell-enforced latency in syngeneic models. We also investigated the role of NK cells as suppressors of DTC expansion in syngeneic immunocompetent mouse models. One model was based on lung adenocarcinoma cell lines derived from tumor-bearing *Kras^{G12D}/p53^{Del}* mice (34). The 482T1 (T-Met) cell line readily metastasizes to the liver when injected into the spleen of syngeneic B6129SF1 mice, whereas the 368T1 (T-nonMet) line does not form overt metastases in these assays (34). We conducted these experiments in control B6129SF1 mice or mice that were treated with anti-asialo-GM1 antibody to deplete NK cells. NK cell depletion resulted in a 100-fold increase in the liver metastatic activity of T-nonMet cells, reaching a level that was comparable to that of T-Met cells (Figure 4H-I). We obtained

similar results in 4TO7 cells, a non-metastatic cell line derived from a spontaneous BALB/c mouse mammary tumor (35).

Collectively, these results suggested that LCC cells can proliferate after infiltrating distant organs, but NK cell immune surveillance prevents the accumulation of progeny and only spares LCC cells that enter quiescence.

Progress under Task 4: Establish the functional relevance of LCC genes and pathways.

Progress Item 4.1. Downregulation of NK cell activators in quiescent LCC cells. A balance of activating and inhibitory signals regulates the ability of NK cells to target cancer cells for elimination (36, 37). Oncogenic transformation leads to loss of NK cell inhibitory receptors and upregulation of NK cell activating ligands in tumor cells, which in turn promotes NK cell-mediated clearance of cancer cells. During tumor progression, cancer cell evolve to escape NK cell mediated recognition (38-41). As LCC cells survived NK cell-mediated immune surveillance in athymic mice, we queried LCC gene expression profiles for potential mechanisms of immune evasion.

We examined gene expression signatures associated with immune recognition and clearance by macrophages, T, B, or NK cells. Genes signatures associated with NK cell-mediated cytotoxicity, in particular, were downregulated in LCC cells compared to parental H2087 and HCC1954 populations. Moreover, quiescence-inducing (MLM) conditions induced additional changes in the expression of NK cell activators in LCC cells. The genes that were further downregulated in quiescent LCC cells encode key NK cell activators (Figure 5A-B). These genes include UL16-binding proteins (ULBP; also known as retinoic acid early transcript, RAET) ULBP2/RAET1H, ULBP3/RAET1N, and ULBP5/RAET1G, are frequently expressed by malignant cells and stimulate anti-tumor responses mediated by the NK activating receptor NKG2D/CD314 (42), and PVR/CD155 is a ligand for the NK cell receptor CD226/DNAM-1 (DNAX accessory molecule-1) that activates cancer cell killing (43). The pro-apoptotic cytokine receptors FAS and TRAILR, which are critical for NK cell-mediated target killing (44, 45), were also downregulated in LCC cells under quiescence conditions (Figure 5A-B). To determine if LCC cells entering quiescence are intrinsically resistant to the cytotoxic action of NK cells, we incubated parental and LCC cells in low-mitogen media and then added freshly isolated, IL-2 activated mouse spleen NK cells to the cultures (Figure 5C). Compared to parental populations, LCC cells showed resistance to cytolysis when incubated with NK cells (Figure 5D). Thus, LCC cells that enter quiescence undergo a striking downregulation of a set of NK cell activators, and acquire resistance to NK mediated cell killing.

Progress Item 4.2. Attenuated WNT signaling associated with LCC quiescence. To identify what primes LCC cells to enter a quiescent state, we applied signaling pathway classifier analysis to the transcriptomic data sets (46). Under quiescence conditions, all H2087-LCC cell lines showed a marked reduction in WNT, MYC and NF- κ B signaling activity, and an increase in TGF- β signaling activity (Figure 6A). WNT signaling response was also attenuated in HCC1954 LCC cells under these conditions. MYC is a downstream target of WNT signaling (47), and TGF- β is a known mediator of cytostasis (48). A high ratio of phospho-p38 to phospho-ERK kinases, previously described in dormant cancer cell models (49), was present in HCC1954-LCC but not in H2087-LCC cells.

WNT is a potent mitogen for stem and progenitor cells, and is implicated in metastatic outgrowth in lung adenocarcinoma (14) and breast cancer stem cells (50, 51). H2087-LCC cells demonstrated a clear resistance to pathway activation by WNT3A addition, as determined by *Axin2* expression (Figure 6B) (52), and TCF transcriptional reporter activation (53). Therefore, we investigated the possibility that LCC cells produce a WNT inhibitor. We observed that the WNT signaling inhibitor dickkopf-related protein 1 (DKK1) was highly expressed in LCC cell lines compared to parental counterparts, both at the mRNA and protein levels (Figure 6C). DKK1 expression by LCC cells *in vivo* was confirmed by immunofluorescence staining (Figure 6D).

Progress under Task 5: Establish the clinical relevance of LMBC genes and pathways

Progress Item 5.1. We have started this task with work on a set of breast cancer patient derived xenografts (PDXs), which recapitulate the histopathology, heterogeneity and metastatic properties of the primary tumor (54, 55). Surgical orthotopic implantation of hormone receptor-negative breast cancers PDX models HCI-001 and HCI-002, and HER2+ breast cancer PDX model HCI-008, gave rise to tumors with no visible metastasis (Figure 6E) (54). Orthotopic PDX tumors expressed human Vimentin, which we used as a surrogate marker to identify disseminated cancer cells in the lungs, brain and kidneys of mice bearing these tumors. 14% - 51% of disseminated cancer cells were positive for both human vimentin and DKK1 expression (Figure 6E). These data demonstrated DKK1 expression in disseminated tumor cells from orthotopically implanted PDX models.

Progress under Task 6: Mechanism of action of LCC genes and pathways.

Progress Item 6.1. Direct mechanistic link between SOX2 and DKK1 expression. *DKK1* is a direct target of Sox2-mediated transcriptional activation in mesenchymal stem cells, where Sox2 binds to the ~ 75 base pairs upstream of the *DKK1* transcriptional start site (56, 57). Indeed, H2087-LCC1 cells showed Sox2 binding to this promoter region (Figure 6F). Stable shRNA knockdown of Sox2 in LCC cells decreased the expression of DKK1 (Figure 6G). DKK1 knockdown re-sensitized LCC cells to WNT pathway activation, as demonstrated by increased *Axin2* expression upon WNT3A addition (Figure 6H). Dye retention assays demonstrated that DKK1 knockdown stimulated the proliferation of LCC cells under low-mitogen conditions (Figure 6I).

Progress Item 6.2. Autocrine DKK1 enforces a quiescent, immune evasive state in latent metastasis. The preceding results suggested that autocrine DKK1 primes LCC cells to enter quiescence, which leads to downregulation of NK cell activators. One prediction of this model is that autocrine DKK1 is required to protect LCC cells from elimination in athymic mice. In line with this prediction, shRNA-mediated DKK1 depletion in LCC cells significantly decreased the accumulation of LCC cells in the lungs of inoculated athymic mice (Figure 7A). Moreover, Ki-67+ stromal cells surrounded the cancer cells in bronchiolar regions under these conditions. Many of these stromal cells were positive for the leukocyte common antigen CD45, suggesting that DKK1-depleted LCC cells trigger lymphocyte infiltration and for cancer cell clearance. DKK1 knockdown in H2087-LCC cells increased the expression of NK cell activating ligands ULBP1, 2, 4 and 5, and several death signal receptors (Figure 7B). Moreover, depletion of NK cells in athymic mice rescued the formation of macrometastases by DKK1-knockdown H2087-

LCC2 cells (Figure 7C), suggesting that LCC cells liberated from DKK1 growth inhibition can grow as macrometastases in a growth permissive microenvironment.

In contrast to the deleterious effect of DKK1 knockdown on the viability of LCC cells in athymic mice, DKK1 knockdown increased the metastatic growth of LCC cells in NSG mice (Figure 7D-E). Conversely, overexpressing DKK1 in H2087-LCC cells inhibited their growth in NSG mice. As a corollary, depletion of Sox2 in H2087-LCC or Sox9 in HCC1954-LCC cells inhibited the ability of these cells to form metastasis in NSG mice (Figure 7F) as it did in athymic mice. These data confirmed the essential role of Sox transcription factors for metastatic growth of LCC cells, and the ability of NK cells to restrain LCC outgrowth but spare quiescent LCC cells (Figure 7G).

Progress under Task 7: Define the feasibility of targeting residual disease genes and pathways in pre-clinical trials

Two lines of work that we conducted in parallel with the above studies, and partly supported with this Award, have begun to address the feasibility of targeting different aspects of residual metastatic disease based on our basic research findings.

Progress Item 7.1. Pharmacologic inhibition of gap junction activity against brain metastasis. Brain metastasis represents a substantial source of morbidity and mortality in various cancers, and is characterized by high resistance to chemotherapy. The role of the most abundant cell type in the brain, the astrocyte, in brain metastasis has remained ambiguous. In ongoing studies we have demonstrated that breast cancer and lung cancer cells express protocadherin 7 (PCDH7) to favor the assembly of carcinoma-astrocyte gap junctions composed of connexin 43 (Cx43). Once engaged with the astrocyte gap-junctional network, brain metastatic cancer cells employ these channels to pass cytosolic dsDNA to the astrocytes, activating the cGAS-STING pathway and production of inflammatory cytokines IFN α and TNF α . As paracrine signals, these factors activate the STAT1 and NF- κ B pathways in brain metastatic cells, which support tumor growth and chemoresistance.

The evidence that genetic inhibition of gap junction components decreased brain metastatic outgrowth provided a rationale for testing pharmacologic suppressors of gap junction activity against brain metastasis. To this end, we selected two orally bioavailable compounds for pre-clinical trials. In addition to anti-inflammatory activity, meclofenamate inhibits Cx43 gap junction gating (58), inhibits epileptogenesis in animal models (59), passes the BBB after systemic administration (58), is well tolerated systemically (60) and is currently an FDA-approved NSAID. Tonabersat is an benzopyran derivative that binds to a unique stereoselective binding site in astrocytes (61, 62), inhibits gap-junction-mediated pathophysiological processes including cortical spreading depression (63) and trigeminal ganglion neuronal-satellite cell signaling in animal models (64), and was systemically well-tolerated and safe in patients with migraine (65).

Both Tonabersat and meclofenamate inhibited dye transfer from astrocytes to cancer cells as measured by flow cytometry (Fig. 8A), and the release of IFN α and TNF α in co-cultures of these cells (Fig. 8B), recapitulating the phenotype seen in knockdown of Cx43 or PCDH7. Mice were treated with either vehicle or with these compounds from day 1 following arterial inoculation of MDA231-BrM2 cells or H2030-BrM3 cells in immunodeficient mice, or KRas/p53-393N1 cells

in immunocompetent mice (Fig. 8C). Both drugs prevented the emergence of brain metastases, consistent with our evidence that gap junction activity is relevant for metastatic outgrowth. However, this treatment did not restrict growth of MDA231-BrM2 cells as lung metastatic lesions or as orthotopic tumors.

Progress Item 7.2. Gap junction directed therapy. To test the effect of Cx43 or PCDH7 depletion in established metastases, we transduced MDA231-BrM2 cells with Tet-inducible shRNA expression vectors (Fig. 8E). A red fluorescence protein (RFP) under the control of the same promoter provided a marker of hairpin expression *in vivo*. Cells transduced with inducible Cx43 or PCDH7 shRNA vectors showed doxycycline-dependent depletion of Cx43 or PCDH7, respectively. These cells were injected intracardially and allowed to form brain metastases for 14 days. At this stage, brain lesions are apparent by BLI in all mice; the aggressive lesions engulf the microvasculature (Fig. 8D) and will result in death of the animals in 2-3 weeks (15). Doxycycline administration starting on day 14 resulted in reduced brain metastatic burden three weeks later, compared to controls (Fig. 8F,G).

Brain metastases are distinguished by pronounced resistance to chemotherapy (66, 67). Carboplatin crosses the BBB (68), with modest improvement in overall survival in patients with brain metastases from breast (69) or lung cancer (70). Carboplatin alone (50 mg/kg/5 days) starting on day 14 inhibited brain metastasis to a similar extent as depletion of Cx43 or PCDH7 (Fig. 8F,G); combination carboplatin and doxycycline reduced the metastatic burden further (Fig. 8F,G). Therefore, we assessed the effectiveness of combination gap junction modulatory therapy with chemotherapy (Fig. 8H). Treatment with carboplatin alone minimally inhibited brain metastasis growth (Fig. 8I). Either Tonabersat (10 mg/kg) or meclofenamate (20 mg/kg) as single agents (Fig. 8I) significantly inhibited progression of metastatic lesions at the 35-day end point. The combination of carboplatin with either Tonabersat or meclofenamate profoundly inhibited brain metastasis (Fig. 8I).

Progress Item 7.3. Pilot Clinical Trial NCT 02429570. With these results we introduce a therapeutic strategy based on existing modulators of gap junctions, meclofenamate and Tonabersat, that breaks this paracrine loop, and provide proof-of-principle for its applicability to treat established brain metastasis. Based on these results, the co-first author of the submitted manuscript, Dr. Adrienne Boire, MD, PhD, and a neurooncologist, has initiated a Pilot Clinical Trial (NCT 02429570) of Meclofenamate in subjects with recurrent or progressive brain metastasis from solid tumor primary <https://clinicaltrials.gov/ct2/show/NCT02429570>

Progress Item 7.4. Therapy-induced tumor secretomes and resistance and tumor progression. Drug resistance invariably limits the clinical efficacy of targeted therapy with kinase inhibitors against cancer. In recently published work (71) we show that targeted therapy with BRAF, ALK, or EGFR kinase inhibitors induces a complex network of secreted signals in drug-stressed melanoma and lung adenocarcinoma cells. This therapy-induced secretome (TIS) stimulates the outgrowth, dissemination, and metastasis of drug-resistant cancer cell clones and supports the survival of drug-sensitive cancer cells, contributing to incomplete tumour regression. The vemurafenib reactive secretome in melanoma is driven by down-regulation of the transcription factor FRA1. *In situ* transcriptome analysis of drug-resistant melanoma cells responding to the regressing tumour microenvironment revealed hyperactivation of multiple signalling pathways, most prominently the AKT pathway. Dual inhibition of RAF and

PI3K/AKT/mTOR pathways blunted the outgrowth of the drug-resistant cell population in *BRAF* mutant melanoma tumours, suggesting this combination therapy as a strategy against tumour relapse. Thus, therapeutic inhibition of oncogenic drivers induces vast secretome changes in drug-sensitive cancer cells, paradoxically establishing a tumour microenvironment that supports the expansion of drug-resistant clones, but is susceptible to combination therapy. (**Refer to Appendix – Publication**).

KEY RESEARCH ACCOMPLISHMENTS

- Selection for phenotypically representative models of latent metastasis from early-stage lung and breast cancers, Latency Competent Cancer (LCC) cells
- LCC cells shown to have stem-like properties, are prone to enter quiescence, and highly express Sox2 or Sox9 stem/progenitor identity factors. Disseminated cancer cells with these characteristics can persist long-term as latent seeds of metastasis.
- Demonstration that LCC cells can initiate metastasis after infiltrating distant organs
- Demonstration that NK cell-mediated immune surveillance prevents the accumulation of LCC progeny, but spare LCC cells that enter quiescence.
- Discovery that LCC cells express DKK1 as an autocrine promoter of cell quiescence.
- Finding that LCC quiescence leads to downregulation of NK cell activators and evasion of NK cell-mediated killing.
- Proof of principle that gap junction modulators tonabersat and meclofenamate can inhibit brain metastasis
- Initiation of Clinical Trial NCT 02429570, Meclofenamate in subjects with recurrent or progressive brain metastasis from solid tumor primary

CONCLUSION

The overall goals of this project are to biologically dissect, molecularly deconstruct, and conceptually understand latent metastasis of breast cancer, in order to target its viability for the prevention of metastasis. Our progress towards this goal is on schedule. We have accomplished the tasks that were scheduled for the period of this Progress Report. We have encountered new and unexpected findings. There have been no major unforeseen problems in the development of this work.

CHANGES IN PERSONNEL

- Saloni Agrawal has been added to the project as a Research Technician

PUBLICATIONS, ABSTRACTS AND PRESENTATIONS

a. Publications

1. Lay Press: Nothing to report
2. Peer-Reviewed Scientific Journals:
 - Obenauf, A.C., Zou, Y., Ji, A.L., Vanharanta, S., Shu, W., Shi, H., Kong, X., Bosenberg, M.C., Wiesner, T., Rosen, N., Lo, R.S., and Massagué, J. Therapy induced tumour

secretomes promote resistance and tumour progression. **Nature** 520, 368-372 (2015) PMC 4507807

This paper attracted widespread attention as illustrated by the following editorial commentaries on the significance of our findings: Bernards, R. **Cell Res.** 25, 763-764 (2015); Killock, D. **Nat. Rev. Clin. Oncol.** 12, 309 (2015); Gough, N. R. **Sci. Signal.** ec102 (2015)

- Chen, Q., Boire, A., Jin, X., Valiente, M., Er, E.E., Lopez-Soto, A., Pawta, R., Shah, H., Xu, K., Cross, J.R., and Massagué, J. Cancer cell-astrocyte gap junctions mediate brain metastasis through the cytosolic dsDNA response pathway. *Submitted for publication*

3. Invited Articles:

- Obenauf, A. and Massagué, J. Surviving at a distance: organ specific metastasis. **Trends in Cancer**, in press NIHMS714178

4. Abstracts: Nothing to report

b. Presentations made during the last year.

b.1. International:

- Charles Rodolphe Brupbacher Symposium, *Breakthroughs in Cancer Research and Therapy*, Zurich Switzerland
- Gordon Research Conference on *Stem Cells & Cancer*, Ventura, CA
- ISPEN Cancer Series Meeting, *Tumor Heterogeneity and Tumor Microenvironment*, Mysore, India
- EMBO/EMBL Symposium, *Frontiers in Stem Cells & Cancer*, Heidelberg, Germany
- AACR Conference on *Advances in Brain Cancer Research*, Washington, DC

b.2. National:

- *Origins of Metastatic Traits*, Danny Thomas Lecture, St. Jude Children's Hospital, Memphis, TN
- *Deconstructing Metastasis*, Distinguished Guest Lecture, Baylor College of Medicine, Houston, TX
- *Deconstructing CNS Metastasis*, Neurology Grand Rounds, Albert Einstein College of Medicine, NY
- *Scientific Perspectives on Cancer*, Surgery Grand Rounds, MSKCC, New York, NY
- *Stock Lecture*, Medicine Grand Rounds, MSKCC, New York, NY

- *Metastasis Initiating Cells*, Cell Press Lab Links Intersections of Stem Cell Biology and Cancer, NYU, NY

INVENTIONS, PATENTS AND LICENSES

- Massagué, J, Boire, A., and Chen, Q., Methods For Treating Brain Metastasis. United States Provisional Patent Application No. 62/052,966 Filed September 19, 2014.

REPORTABLE OUTCOMES

- Identification of DKK1 and NK activators as potential therapeutic targets to eliminate disseminated cancer cells.
- Proof of principle that gap junction modulators tonabersat and meclofenamate can inhibit brain metastasis, and initiation of a clinical trial.

OTHER ACHIEVEMENTS

Joan Massagué:

2014	National Prize for Research in Biology, Spain
2015	Charles Rodolphe Brupbacher Prize for Cancer Research
2015	Keynote address, Stem Cells and Cancer Gordon Conference
2015	Member, External Advisory Board, Salk Institute Cancer Center

REFERENCES

1. W. Janni, B. Rack, C. Schindlbeck, B. Strobl, D. Rjosk, S. Braun, H. Sommer, K. Pantel, B. Gerber, K. Friese, The persistence of isolated tumor cells in bone marrow from patients with breast carcinoma predicts an increased risk for recurrence. *Cancer* **103**, 884-891 (2005).
2. S. Braun, F. D. Vogl, B. Naume, W. Janni, M. P. Osborne, R. C. Coombes, G. Schlimok, I. J. Diel, B. Gerber, G. Gebauer, J. Y. Pierga, C. Marth, D. Oruzio, G. Wiedswang, E. F. Solomayer, G. Kundt, B. Strobl, T. Fehm, G. Y. Wong, J. Bliss, A. Vincent-Salomon, K. Pantel, A pooled analysis of bone marrow micrometastasis in breast cancer. *The New England journal of medicine* **353**, 793-802 (2005).
3. H. G. Welch, W. C. Black, Using autopsy series to estimate the disease "reservoir" for ductal carcinoma in situ of the breast: how much more breast cancer can we find? *Annals of internal medicine* **127**, 1023-1028 (1997).
4. C. A. Klein, Framework models of tumor dormancy from patient-derived observations. *Current opinion in genetics & development* **21**, 42-49 (2011).
5. H. Wikman, R. Vessella, K. Pantel, Cancer micrometastasis and tumour dormancy. *APMIS : acta pathologica, microbiologica, et immunologica Scandinavica* **116**, 754-770 (2008).
6. P. E. Goss, A. F. Chambers, Does tumour dormancy offer a therapeutic target? *Nature reviews. Cancer* **10**, 871-877 (2010).
7. M. S. Sosa, P. Bragado, J. A. Aguirre-Ghiso, Mechanisms of disseminated cancer cell dormancy: an awakening field. *Nature reviews. Cancer* **14**, 611-622 (2014).
8. A. F. Gazdar, J. D. Minna, NCI series of cell lines: an historical perspective. *Journal of cellular biochemistry. Supplement* **24**, 1-11 (1996).
9. A. F. Gazdar, V. Kurvari, A. Virmani, L. Gollahon, M. Sakaguchi, M. Westerfield, D. Kodagoda, V. Stasny, H. T. Cunningham, Wistuba, II, G. Tomlinson, V. Tonk, R. Ashfaq, A. M. Leitch, J. D. Minna, J. W. Shay, Characterization of paired tumor and non-tumor cell lines established from patients with breast cancer. *International journal of cancer. Journal international du cancer* **78**, 766-774 (1998).
10. R. Maeda, J. Yoshida, T. Hishida, K. Aokage, M. Nishimura, Y. Nishiwaki, K. Nagai, Late recurrence of non-small cell lung cancer more than 5 years after complete resection: incidence and clinical implications in patient follow-up. *Chest* **138**, 145-150 (2010).
11. R. Duchnowska, R. Dziadziuszko, B. Czartoryska-Arlukowicz, B. Radecka, B. Szostakiewicz, K. Sosinska-Mielcarek, A. Karpinska, E. Staroslawska, T. Kubiatowski, C. Szczylik, Risk factors for brain relapse in HER2-positive metastatic breast cancer patients. *Breast cancer research and treatment* **117**, 297-303 (2009).
12. M. Pelleitier, S. Montplaisir, The nude mouse: a model of deficient T-cell function. *Methods and achievements in experimental pathology* **7**, 149-166 (1975).
13. Y. Kang, P. M. Siegel, W. Shu, M. Drobniak, S. M. Kakonen, C. Cordon-Cardo, T. A. Guise, J. Massague, A multigenic program mediating breast cancer metastasis to bone. *Cancer cell* **3**, 537-549 (2003).
14. D. X. Nguyen, A. C. Chiang, X. H. Zhang, J. Y. Kim, M. G. Kris, M. Ladanyi, W. L. Gerald, J. Massague, WNT/TCF signaling through LEF1 and HOXB9 mediates lung adenocarcinoma metastasis. *Cell* **138**, 51-62 (2009).

15. M. Valiente, A. C. Obenauf, X. Jin, Q. Chen, X. H. Zhang, D. J. Lee, J. E. Chaft, M. G. Kris, J. T. Huse, E. Brogi, J. Massague, Serpins promote cancer cell survival and vascular co-option in brain metastasis. *Cell* **156**, 1002-1016 (2014).
16. E. Lim, D. Wu, B. Pal, T. Bouras, M. L. Asselin-Labat, F. Vaillant, H. Yagita, G. J. Lindeman, G. K. Smyth, J. E. Visvader, Transcriptome analyses of mouse and human mammary cell subpopulations reveal multiple conserved genes and pathways. *Breast cancer research : BCR* **12**, R21 (2010).
17. M. Al-Hajj, M. S. Wicha, A. Benito-Hernandez, S. J. Morrison, M. F. Clarke, Prospective identification of tumorigenic breast cancer cells. *Proceedings of the National Academy of Sciences of the United States of America* **100**, 3983-3988 (2003).
18. B. Treutlein, D. G. Brownfield, A. R. Wu, N. F. Neff, G. L. Mantalas, F. H. Espinoza, T. J. Desai, M. A. Krasnow, S. R. Quake, Reconstructing lineage hierarchies of the distal lung epithelium using single-cell RNA-seq. *Nature* **509**, 371-375 (2014).
19. A. Sarkar, K. Hochedlinger, The sox family of transcription factors: versatile regulators of stem and progenitor cell fate. *Cell stem cell* **12**, 15-30 (2013).
20. K. Arnold, A. Sarkar, M. A. Yram, J. M. Polo, R. Bronson, S. Sengupta, M. Seandel, N. Geijsen, K. Hochedlinger, Sox2(+) adult stem and progenitor cells are important for tissue regeneration and survival of mice. *Cell stem cell* **9**, 317-329 (2011).
21. W. Guo, Z. Keckesova, J. L. Donaher, T. Shibue, V. Tischler, F. Reinhardt, S. Itzkovitz, A. Noske, U. Zurrer-Hardi, G. Bell, W. L. Tam, S. A. Mani, A. van Oudenaarden, R. A. Weinberg, Slug and Sox9 cooperatively determine the mammary stem cell state. *Cell* **148**, 1015-1028 (2012).
22. K. Takahashi, S. Yamanaka, Induction of pluripotent stem cells from mouse embryonic and adult fibroblast cultures by defined factors. *Cell* **126**, 663-676 (2006).
23. A. J. Bass, H. Watanabe, C. H. Mermel, S. Yu, S. Perner, R. G. Verhaak, S. Y. Kim, L. Wardwell, P. Tamayo, I. Gat-Viks, A. H. Ramos, M. S. Woo, B. A. Weir, G. Getz, R. Beroukhim, M. O'Kelly, A. Dutt, O. Rozenblatt-Rosen, P. Dziunycz, J. Komisarof, L. R. Chirieac, C. J. Lafargue, V. Scheble, T. Wilbertz, C. Ma, S. Rao, H. Nakagawa, D. B. Stairs, L. Lin, T. J. Giordano, P. Wagner, J. D. Minna, A. F. Gazdar, C. Q. Zhu, M. S. Brose, I. Cecconello, U. R. Jr, S. K. Marie, O. Dahl, R. A. Shviddasani, M. S. Tsao, M. A. Rubin, K. K. Wong, A. Regev, W. C. Hahn, D. G. Beer, A. K. Rustgi, M. Meyerson, SOX2 is an amplified lineage-survival oncogene in lung and esophageal squamous cell carcinomas. *Nature genetics* **41**, 1238-1242 (2009).
24. C. M. Rudin, S. Durinck, E. W. Stawiski, J. T. Poirier, Z. Modrusan, D. S. Shames, E. A. Bergbower, Y. Guan, J. Shin, J. Guillory, C. S. Rivers, C. K. Foo, D. Bhatt, J. Stinson, F. Gnad, P. M. Haverty, R. Gentleman, S. Chaudhuri, V. Janakiraman, B. S. Jaiswal, C. Parikh, W. Yuan, Z. Zhang, H. Koeppen, T. D. Wu, H. M. Stern, R. L. Yauch, K. E. Huffman, D. D. Paskulin, P. B. Illei, M. Varella-Garcia, A. F. Gazdar, F. J. de Sauvage, R. Bourgon, J. D. Minna, M. V. Brock, S. Seshagiri, Comprehensive genomic analysis identifies SOX2 as a frequently amplified gene in small-cell lung cancer. *Nature genetics* **44**, 1111-1116 (2012).
25. U. Kordes, C. Hagel, Expression of SOX9 and SOX10 in central neuroepithelial tumor. *Journal of neuro-oncology* **80**, 151-155 (2006).
26. G. Dontu, W. M. Abdallah, J. M. Foley, K. W. Jackson, M. F. Clarke, M. J. Kawamura, M. S. Wicha, In vitro propagation and transcriptional profiling of human mammary stem/progenitor cells. *Genes & development* **17**, 1253-1270 (2003).

27. Y. Hayakawa, M. J. Smyth, Innate immune recognition and suppression of tumors. *Advances in cancer research* **95**, 293-322 (2006).

28. M. Paolino, A. Choidas, S. Wallner, B. Pranjic, I. Uribesalgo, S. Loeser, A. M. Jamieson, W. Y. Langdon, F. Ikeda, J. P. Fededa, S. J. Cronin, R. Nitsch, C. Schultz-Fademrecht, J. Eickhoff, S. Menninger, A. Unger, R. Torka, T. Gruber, R. Hinterleitner, G. Baier, D. Wolf, A. Ullrich, B. M. Klebl, J. M. Penninger, The E3 ligase Cbl-b and TAM receptors regulate cancer metastasis via natural killer cells. *Nature* **507**, 508-512 (2014).

29. M. J. Smyth, G. P. Dunn, R. D. Schreiber, Cancer immunosurveillance and immunoediting: the roles of immunity in suppressing tumor development and shaping tumor immunogenicity. *Advances in immunology* **90**, 1-50 (2006).

30. L. D. Shultz, B. L. Lyons, L. M. Burzenski, B. Gott, X. Chen, S. Chaleff, M. Kotb, S. D. Gillies, M. King, J. Mangada, D. L. Greiner, R. Handgretinger, Human lymphoid and myeloid cell development in NOD/LtSz-scid IL2R gamma null mice engrafted with mobilized human hemopoietic stem cells. *Journal of immunology* **174**, 6477-6489 (2005).

31. D. K. Sojka, B. Plougastel-Douglas, L. Yang, M. A. Pak-Wittel, M. N. Artyomov, Y. Ivanova, C. Zhong, J. M. Chase, P. B. Rothman, J. Yu, J. K. Riley, J. Zhu, Z. Tian, W. M. Yokoyama, Tissue-resident natural killer (NK) cells are cell lineages distinct from thymic and conventional splenic NK cells. *eLife* **3**, e01659 (2014).

32. M. Kasai, T. Yoneda, S. Habu, Y. Maruyama, K. Okumura, T. Tokunaga, In vivo effect of anti-asialo GM1 antibody on natural killer activity. *Nature* **291**, 334-335 (1981).

33. J. C. Sun, L. L. Lanier, Cutting edge: viral infection breaks NK cell tolerance to "missing self". *Journal of immunology* **181**, 7453-7457 (2008).

34. M. M. Winslow, T. L. Dayton, R. G. Verhaak, C. Kim-Kiselak, E. L. Snyder, D. M. Feldser, D. D. Hubbard, M. J. DuPage, C. A. Whittaker, S. Hoersch, S. Yoon, D. Crowley, R. T. Bronson, D. Y. Chiang, M. Meyerson, T. Jacks, Suppression of lung adenocarcinoma progression by Nkx2-1. *Nature* **473**, 101-104 (2011).

35. C. J. Aslakson, F. R. Miller, Selective events in the metastatic process defined by analysis of the sequential dissemination of subpopulations of a mouse mammary tumor. *Cancer research* **52**, 1399-1405 (1992).

36. M. D. Vesely, M. H. Kershaw, R. D. Schreiber, M. J. Smyth, Natural innate and adaptive immunity to cancer. *Annual review of immunology* **29**, 235-271 (2011).

37. J. Wu, L. L. Lanier, Natural killer cells and cancer. *Advances in cancer research* **90**, 127-156 (2003).

38. H. G. Ljunggren, K. J. Malmberg, Prospects for the use of NK cells in immunotherapy of human cancer. *Nature reviews. Immunology* **7**, 329-339 (2007).

39. G. P. Dunn, L. J. Old, R. D. Schreiber, The immunobiology of cancer immunosurveillance and immunoediting. *Immunity* **21**, 137-148 (2004).

40. T. O'Sullivan, R. Saddawi-Konefka, W. Vermi, C. M. Koebel, C. Arthur, J. M. White, R. Uppaluri, D. M. Andrews, S. F. Ngiow, M. W. Teng, M. J. Smyth, R. D. Schreiber, J. D. Bui, Cancer immunoediting by the innate immune system in the absence of adaptive immunity. *The Journal of experimental medicine* **209**, 1869-1882 (2012).

41. J. M. Reiman, M. Kmiecik, M. H. Manjili, K. L. Knutson, Tumor immunoediting and immunosculpting pathways to cancer progression. *Seminars in cancer biology* **17**, 275-287 (2007).

42. L. L. Lanier, NKG2D Receptor and Its Ligands in Host Defense. *Cancer immunology research* **3**, 575-582 (2015).

43. L. Martinet, M. J. Smyth, Balancing natural killer cell activation through paired receptors. *Nature reviews. Immunology* **15**, 243-254 (2015).

44. M. Bradley, A. Zeytun, A. Rafi-Janajreh, P. S. Nagarkatti, M. Nagarkatti, Role of spontaneous and interleukin-2-induced natural killer cell activity in the cytotoxicity and rejection of Fas+ and Fas- tumor cells. *Blood* **92**, 4248-4255 (1998).

45. K. Takeda, M. J. Smyth, E. Cretney, Y. Hayakawa, N. Yamaguchi, H. Yagita, K. Okumura, Involvement of tumor necrosis factor-related apoptosis-inducing ligand in NK cell-mediated and IFN-gamma-dependent suppression of subcutaneous tumor growth. *Cellular immunology* **214**, 194-200 (2001).

46. X. H. Zhang, Q. Wang, W. Gerald, C. A. Hudis, L. Norton, M. Smid, J. A. Foekens, J. Massague, Latent bone metastasis in breast cancer tied to Src-dependent survival signals. *Cancer cell* **16**, 67-78 (2009).

47. T. C. He, A. B. Sparks, C. Rago, H. Hermeking, L. Zawel, L. T. da Costa, P. J. Morin, B. Vogelstein, K. W. Kinzler, Identification of c-MYC as a target of the APC pathway. *Science* **281**, 1509-1512 (1998).

48. J. Massague, TGF-beta signaling in development and disease. *FEBS letters* **586**, 1833 (2012).

49. J. A. Aguirre-Ghiso, Y. Estrada, D. Liu, L. Ossowski, ERK(MAPK) activity as a determinant of tumor growth and dormancy; regulation by p38(SAPK). *Cancer research* **63**, 1684-1695 (2003).

50. I. Malanchi, A. Santamaria-Martinez, E. Susanto, H. Peng, H. A. Lehr, J. F. Delaloye, J. Huelsken, Interactions between cancer stem cells and their niche govern metastatic colonization. *Nature* **481**, 85-89 (2012).

51. T. Oskarsson, S. Acharyya, X. H. Zhang, S. Vanharanta, S. F. Tavazoie, P. G. Morris, R. J. Downey, K. Manova-Todorova, E. Brogi, J. Massague, Breast cancer cells produce tenascin C as a metastatic niche component to colonize the lungs. *Nature medicine* **17**, 867-874 (2011).

52. H. Clevers, R. Nusse, Wnt/beta-catenin signaling and disease. *Cell* **149**, 1192-1205 (2012).

53. C. Fuerer, R. Nusse, Lentiviral vectors to probe and manipulate the Wnt signaling pathway. *PloS one* **5**, e9370 (2010).

54. Y. S. DeRose, G. Wang, Y. C. Lin, P. S. Bernard, S. S. Buys, M. T. Ebbert, R. Factor, C. Matsen, B. A. Milash, E. Nelson, L. Neumayer, R. L. Randall, I. J. Stijleman, B. E. Welm, A. L. Welm, Tumor grafts derived from women with breast cancer authentically reflect tumor pathology, growth, metastasis and disease outcomes. *Nature medicine* **17**, 1514-1520 (2011).

55. J. R. Whittle, M. T. Lewis, G. J. Lindeman, J. E. Visvader, Patient-derived xenograft models of breast cancer and their predictive power. *Breast cancer research : BCR* **17**, 17 (2015).

56. S. B. Park, K. W. Seo, A. Y. So, M. S. Seo, K. R. Yu, S. K. Kang, K. S. Kang, SOX2 has a crucial role in the lineage determination and proliferation of mesenchymal stem cells through Dickkopf-1 and c-MYC. *Cell death and differentiation* **19**, 534-545 (2012).

57. E. Seo, U. Basu-Roy, P. H. Gunaratne, C. Coarfa, D. S. Lim, C. Basilico, A. Mansukhani, SOX2 regulates YAP1 to maintain stemness and determine cell fate in the osteo-adipo lineage. *Cell reports* **3**, 2075-2087 (2013).

58. E. G. Harks, A. D. de Roos, P. H. Peters, L. H. de Haan, A. Brouwer, D. L. Ypey, E. J. van Zoelen, A. P. Theuvenet, Fenamates: a novel class of reversible gap junction blockers. *J Pharmacol Exp Ther* **298**, 1033-1041 (2001).

59. M. Jin, Y. Dai, C. Xu, Y. Wang, S. Wang, Z. Chen, Effects of meclofenamic acid on limbic epileptogenesis in mice kindling models. *Neurosci Lett* **543**, 110-114 (2013).

60. E. L. Holmes, Experimental observations on flufenamic, mefenamic, and meclofenamic acids. IV. Toleration by normal human subjects. *Ann Phys Med Suppl*, 36-49 (1966).

61. H. J. Herdon, J. C. Jerman, T. O. Stean, D. N. Middlemiss, W. N. Chan, A. K. Vong, J. M. Evans, M. Thompson, N. Upton, Characterization of the binding of [³H]-SB-204269, a radiolabelled form of the new anticonvulsant SB-204269, to a novel binding site in rat brain membranes. *Br J Pharmacol* **121**, 1687-1691 (1997).

62. W. N. Chan, J. M. Evans, M. S. Hadley, H. J. Herdon, J. C. Jerman, A. A. Parsons, S. J. Read, T. O. Stean, M. Thompson, N. Upton, Identification of (-)-cis-6-acetyl-4S-(3-chloro-4-fluoro-benzoylamino)- 3,4-dihydro-2,2-dimethyl-2H-benzo[b]pyran-3S-ol as a potential antimigraine agent. *Bioorg Med Chem Lett* **9**, 285-290 (1999).

63. S. J. Read, M. I. Smith, A. J. Hunter, N. Upton, A. A. Parsons, SB-220453, a potential novel antimigraine agent, inhibits nitric oxide release following induction of cortical spreading depression in the anaesthetized cat. *Cephalgia* **20**, 92-99 (2000).

64. S. Damodaram, S. Thalakoti, S. E. Freeman, F. G. Garrett, P. L. Durham, Tonabersat inhibits trigeminal ganglion neuronal-satellite glial cell signaling. *Headache* **49**, 5-20 (2009).

65. C. G. Dahlof, A. W. Hauge, J. Olesen, Efficacy and safety of tonabersat, a gap-junction modulator, in the acute treatment of migraine: a double-blind, parallel-group, randomized study. *Cephalgia* **29 Suppl 2**, 7-16 (2009).

66. J. F. Deeken, W. Loscher, The blood-brain barrier and cancer: transporters, treatment, and Trojan horses. *Clinical cancer research : an official journal of the American Association for Cancer Research* **13**, 1663-1674 (2007).

67. R. D. Zhang, J. E. Price, T. Fujimaki, C. D. Bucana, I. J. Fidler, Differential permeability of the blood-brain barrier in experimental brain metastases produced by human neoplasms implanted into nude mice. *Am J Pathol* **141**, 1115-1124 (1992).

68. M. W. Pitz, A. Desai, S. A. Grossman, J. O. Blakeley, Tissue concentration of systemically administered antineoplastic agents in human brain tumors. *Journal of neuro-oncology* **104**, 629-638 (2011).

69. E. Lim, N. U. Lin, Updates on the Management of Breast Cancer Brain Metastases. *Oncology (Williston Park)* **28**, (2014).

70. S. Taimur, M. J. Edelman, Treatment options for brain metastases in patients with non-small-cell lung cancer. *Curr Oncol Rep* **5**, 342-346 (2003).

71. A. C. Obenau, Y. Zou, A. L. Ji, S. Vanharanta, W. Shu, H. Shi, X. Kong, M. C. Bosenberg, T. Wiesner, N. Rosen, R. S. Lo, J. Massague, Therapy-induced tumour secretomes promote resistance and tumour progression. *Nature* **520**, 368-372 (2015).

APPENDICES

Figure 1. Localization and dormancy of disseminated LCC cells.

(A) BLI tracking of mice injected with H2087-LCC1, H2087-LCC2, or the aggressive metastatic lung cancer line H2030-BrM for comparison. Each line represents an individual mouse tracked over the indicated time period. Mice with BLI signal above the dotted red line (whole body photon flux average radiance $>10^6$ photons/sec/cm²/sr) were euthanized.

(B) BLI tracking of mice injected with HCC1954-LCC1 over 5 months, including the aggressive metastatic breast cancer line MDA231-BrM for comparison.

(C) Representative images of BLI signal in mice injected with the indicated LCC cell lines. The number of mice represented by each image is indicated at the bottom.

(D) Representative immunofluorescence staining of disseminated LCC cells (green) next to capillaries (red) in the parenchyma of BLI-negative organ sites.

(E) H2087-LCC2 cells (green) infrequently detected as cell clusters in the lung (top panel) or kidney (bottom panel) remain associated with the vasculature (red).

(F) Spatial localization of single H2087-LCC1 cells (arrows) in BLI-negative organs 3 months post-injection by H&E staining. LCC cells were stochastically distributed in the renal tubule (top-left) or glomeruli (top-right) of the kidney, within alveolar walls of the lung (bottom-left), or capillaries in the brain (bottom-right).

(G) Immunohistochemical staining of disseminated H2087-LCC1 cells from panel 1F with human vimentin (brown) to confirm the presence of human cancer cells in these BLI-negative organs.

(H) Time-course analysis of HCC1954-LCC1 cell morphology (green) as they extravasate and colonize the brain. LCC cells were intimately associated with brain capillaries (red), initially spread along capillaries (left inset) followed by quick adoption of a rounded phenotype (right-inset).

(I) Quantification of HCC1954-LCC1 cell morphology in the brain 3 days and 14 days post-injection. Data are mean percentage of coopting cells per brain \pm S.E.M. N = 3 mice per group, scoring representative serial sections of the entire brain for each mouse. $P < 0.001$ (***)^{***}, Student's t-test. Scale bars, 10 μ m (D), 100 μ m (E), 20 μ m (F and G), and 50 μ m (H).

• Figure 2. LCC cells adopt a slow-cycling state *in vitro* and *in vivo*.

(A) Experimental design for EdU pulse-chase experiment. LCC cells were labeled with EdU for 24hr *in vitro*, and injected into mice by tail-vein injection. Lungs were harvested after 2 weeks, and representative serial sections for each lung were quantitated for EdU+ LCC cells.

(B) LCC cells (green) efficiently labeled *in vitro* with EdU (red).

(C) Detection of double-positive EdU+/GFP+ LCC cells versus parental counterparts in lungs harvested 2 weeks post-injection. Data are mean percentage of EdU+ cells per lung \pm S.E.M. N = 3 mice per group, scoring representative serial sections of the entire lung for each mouse.

- (D) Representative immunofluorescence images of double-positive GFP+/EdU+ LCC cells (green, red) quantified in Figure 2C. $P < 0.05$ (*), $P < 0.01$ (**), Mann-Whitney Test.
- (E) Representative immunofluorescence images of proliferating Ki-67+ (red) H2087-LCC1 (in lung) and HCC1954-LCC1 cells (in brain) 3 months post-injection.
- (F) Quantification of LCC cells from Figure 2E. Data are percentage of total cells that are Ki67⁺ per organ \pm S.E.M. N = 5 per group, scoring representative serial sections of the entire organ of each mouse. $P < 0.001$ (***) Student's t-test.
- (G) Retention of eFluor670 dye by H2087 and HCC1954 derivatives after 6 days of *in vitro* culture in MRM or MLM conditions.
- (H) Cell cycle analysis of H2087 and HCC1954 derivatives by BrdU/APC after 3 days of *in vitro* culture under MRM or MLM conditions. Scale bars, 10 μ m (B and D), and 15 μ m (E).

• **Figure 3. LCC cells are enriched for stem cell-like characteristics.**

- (A) Principal Component Analysis (PCA) of HCC1954 derivatives and normal breast cell populations of human or mouse origin (16) plotted in the same space. HCC1954-LCC cells resemble mammary stem cell (MaSC) gene expression profiles.
- (B) Flow cytometry analysis of cell surface CD24 and CD44 expression in HCC1954 parental and LCC1 cells. HCC1954-LCC1 cells show marked enrichment in the CD44^{Hi}/CD24^{Lo} compartment, indicative of breast cancer stem cells.
- (C) PCA of H2087 derivatives and mouse bronchiolar and alveolar cell lineages (Treutlein, 2014). H2087-LCC cells cluster with the stem-like alveolar type 1 (AT) and bipotent progenitor (BP) cells.
- (D) *Sox2* and *Sox9* mRNA expression levels in H2087 and HCC1954 derivatives.
- (E) *Sox2* and *Sox9* protein expression levels in H2087 and HCC1954 derivatives.
- (F) *Sox2* depletion attenuates survival of H2087-LCC cells in athymic mice. Data are total number of LCC cells scored in the lung 3 months post-injection, with whisker plots representing minimum and maximum values. N = 5-6 mice per group, scoring representative serial sections of the entire lung for each mouse. $P < 0.001$ (***) Mann-Whitney Test.
- (G) *Sox9* depletion attenuates survival of HCC1954-LCC1 cells in athymic mice. Data are total number of LCC cells scored in the brain 2 months post-injection, with whisker plots representing minimum and maximum values. N = 5 mice per group, scoring representative serial sections of the entire brain for each mouse. $P < 0.05$ (*), Mann-Whitney Test.
- (H) *Sox2* expression (red; white arrows) in oncospheres generated from H2087 Parental (top panel) or LCC1 (lower panel) cells.
- (I) Oncosphere-forming capacity is upon *Sox2* depletion in H2087-LCC derivatives. Side panel depicts representative control or *Sox2*-depleted H2087-LCC cell oncospheres. $P < 0.01$ (**), Student's t-test. Scale bars, 25 μ m (H) and 20 μ m (I).

• **Figure 4. LCC cells are in equilibrium with the innate immune system.**

(A-B) BLI tracking of NSG mice injected with HCC1954-LCC (A) or H2087-LCC (B) cells, with aggressive metastatic lines MDA231-LM2 or H2030-BrM shown for comparison. Each line represents one mouse tracked over the indicated time period.

(C) Representative images of BLI signal in NSG mice injected with the indicated LCC cell lines over the indicated time period.

(D) Metastatic outgrowth of HCC1954-LCC1 (green) in the liver, brain, kidney and lungs of NSG mice 2 months post-injection. Vasculature visualized in red with isolectin-B4.

(E) Depletion of NK cells by either anti-NK1.1 (PK136) or anti-asialo-GM1 antibody regimen allows outgrowth of HCC1954-LCC1 cells injected in athymic nude mice. Outgrowth quantified by whole body photon flux at 2 months post-injection, with whisker plots representing minimum and maximum values. N = 5-7 mice per group. $P < 0.001$ (**), Mann-Whitney Test.

(F) Representative *ex vivo* brain BLI images of mice from Figure 4E. Frozen brain tissue sections from these mice show massive outgrowth of HCC1954-LCC1 cells (green) upon NK depletion.

(G) NK cell depletion regimens also allow for outgrowth of H2087-LCC2 cells in athymic nude mice. Outgrowth quantified by whole body photon flux at 2 months post-injection, with whisker plots representing minimum and maximum values. N = 5-7 mice per group. $P < 0.05$ (*), $P < 0.01$ (**), Mann-Whitney Test.

(H) NK cell depletion by anti-asialo GM1 allows liver outgrowth of the non-metastatic cell line T-nonMet intra-splenically injected into syngeneic B6129SF1 mice. The metastatic line T-Met is shown for comparison. Outgrowth quantified by whole body photon flux at 1 month post-injection, with whisker plots representing minimum and maximum values. N = 5-7 mice per group, $P < 0.01$ (**), Mann-Whitney Test.

(I) Representative *ex vivo* gross (top panel) and BLI (bottom panel) liver images from mice in Figure 4H. Scale bars, 100 μ m (D and F).

• **Figure 5. LCC cells evade NK cell mediated immune surveillance.**

(A-B) A diverse set of genes important for NK cell recognition and cytotoxicity are downregulated in both H2087-LCC1 (A) and HCC1954-LCC1 (B) when grown in MLM conditions.

(C) Schematic of *in vitro* NK cell cytotoxicity experiment. Labeled cancer cells grown in MLM conditions are incubated with activated primary NK cells at a 1:5 target:effector ratio for 3 hours, followed by quantification of remaining intact cancer cells.

(D) H2087 and HCC1954-LCC cells are more resistant to NK-cell mediated cytotoxicity compared to parental counterparts. Data are mean percentage of cytolysis \pm S.E.M. for three replicates. $P < 0.01$ (**), $P < 0.001$ (***), Student's t-test.

• **Figure 6. Attenuated WNT signaling enforces quiescence in LCC cells.**

(A) Signaling pathway response signature analysis of H2087 derivatives under MLM conditions shows marked reduction in WNT and MYC pathway activity (upper panel). *MYC* mRNA z score of these derivatives was scored from RNA-seq data (lower panel).

(B) H2087-LCC cells are less responsive to WNT pathway activation by WNT3A stimulation. Relative mRNA expression of *Axin2* upon WNT3A stimulation used as marker for activation of WNT pathway.

(C) DKK1 protein expression levels in H2087 and HCC1954-LCC derivatives relative to Parental. Conditioned media from respective cell lines was assayed for DKK1 expression by ELISA. Data are mean amount of secreted DKK1 protein \pm S.E.M. N = 3 technical replicates per group.

(D) HCC1954-LCC1 cells (green) detected in the brain parenchyma 1 month post-injection in athymic nude mice express DKK1 (red).

(E) Disseminated double-positive DKK1+ (green) and human vimentin+ (red) cells were detected in the lung and kidneys of NSG mice implanted with human breast PDX tumor chunks at the mammary fat pad. SOI: Surgical Orthotopic Implantation.

(F) Sox2 binding to the DKK1 promoter assayed by Sox2 ChIP followed by qRT-PCR analysis of the DKK1 promoter in H2087 derivatives. Error bars \pm S.D.

(G) *Dkk1* mRNA expression diminished in H2087-LCC cells depleted of Sox2.

(H) WNT pathway activation by WNT3a stimulation in H2087-LCC cells depleted of DKK1. Relative mRNA expression of *Axin2* used as marker for WNT pathway activation.

(I) Dye retention assay on H2087-LCC1 cells depleted for DKK1 assayed by flow cytometry after 6 days of *in vitro* culture in MLM conditions. Scale bars, 50 μ m (D and E).

• **Figure 7. DKK1 enforces a quiescent immune evasive state.**

(A) Growth of H2087-LCC cells depleted of DKK1 in the restrictive environment of athymic nude mice. Data are total number of LCC cells detected per lung after 3 months post-tail vein injection \pm S.E.M. N = 5-6 mice per group, scoring representative serial sections of the entire lung for each mouse.

(B) Relative mRNA expression of several NK cell activating ligands and death receptors in H2087-LCC cells upon DKK1 depletion. Relative Quantification is normalized to LCC1 or LCC2 Control.

(C) Depletion of NK cells by anti-asialo-GM1 in athymic nude mice injected with shDKK1 bearing H2087-LCC2 cells. Data are whole body photon flux 2 months post-injection with whisker plots representing minimum and maximum values. N = 5-6 mice per group. $P < 0.01$ (**), Mann-Whitney Test.

(D) Growth of H2087-LCC cells depleted of DKK1 in NSG mice. Data are whole body photon flux 2 months post-injection with whisker plots representing minimum and maximum values. N = 5-6 mice per group. $P < 0.01$ (**), $P < 0.001$ (***), Mann-Whitney Test.

(E) Representative immunofluorescence images of metastatic lesions in the lungs of NSG mice in Figure 7D.

(F) Growth of H2087-LCC cells depleted of SOX2 in NSG mice. Data are whole body photon flux 2 months post-injection with whisker plots representing minimum and maximum values. N = 5-6 mice per group. $P < 0.05$ (*), $P < 0.001$ (**), Mann-Whitney Test.

(G) A model summarizing central tenets of latency recapitulated in our latency competent cancer cell models. Disseminated LCC cells enriched for Sox2/Sox9 stem cell-like programs remain associated with the vasculature, maintain their slow-cycling status by inhibition of proliferative WNT signaling through secretion of autocrine DKK1, and avoid NK cell mediated cell death.

Scale bars, 75 μ m (D) and 50 μ m (F).

• **Figure 8. Inhibition of gap junction activity controls brain metastatic outgrowth.**

(A) Schematic summary of gap junction mediated anti-dsDNA response, production of IFN α and TNF α in astrocytes, and consequent activation of STAT1 and NF- κ B pathways in cancer cells to support brain metastasis.

(B) Dye transfer from astrocytes to MDA231-BrM2 cells in the presence of the indicated concentrations of Tonabersat or meclofenamate. $n \geq 3$ independent experiments.

(C) ELISA of IFN α and TNF α in conditioned media from co-cultured MDA231-BrM2 cell and astrocytes in the presence of Tonabersat (Tona) or meclofenamate (Meclo) with indicated concentrations. All graphs shown are mean \pm S.E.M. ($n=4$ technical replicates). $n=2$ independent experiments.

(D) Tonabersat or meclofenamate was administered daily starting one day after cancer cell inoculation in mice. Brain metastatic lesions were quantified based on BLI. $n=2$ independent experiments.

(E) GFP staining of 14-day brain metastatic lesions. Representative images show large, progressive lesions. DAPI, nuclear staining. Scale Bar, 40 μ m. $n=10$ experimental mice.

(F) 14 days after inoculation with MDA231-BrM2 cells transduced with inducible control, CX43 or *PCDH7* shRNAs, mice were treated with doxycycline and carboplatin, as illustrated in the scheme.

(G, H) Brain metastatic lesions were quantified based on BLI. Representative images of matched *ex vivo* brain BLI and red fluorescence imaging. $n=2$ independent experiments.

(I, J) 14 days after inoculation with MDA231-BrM2 cells, mice were treated with Tonabersat, meclofenamate, and carboplatin. Following the indicated regimens (I), brain metastatic lesions were quantified based on BLI (J). $n=2$ independent experiments.

• **Publication:** Obenauf, A.C., Zou, Y., Ji, A.L., Vanharanta, S., Shu, W., Shi, H., Kong, X., Bosenberg, M.C., Wiesner, T., Rosen, N., Lo, R.S., and Massagué, J. Therapy induced tumour secretomes promote resistance and tumour progression. **Nature** 520, 368-372 (2015) PMC4507807

Figure 1

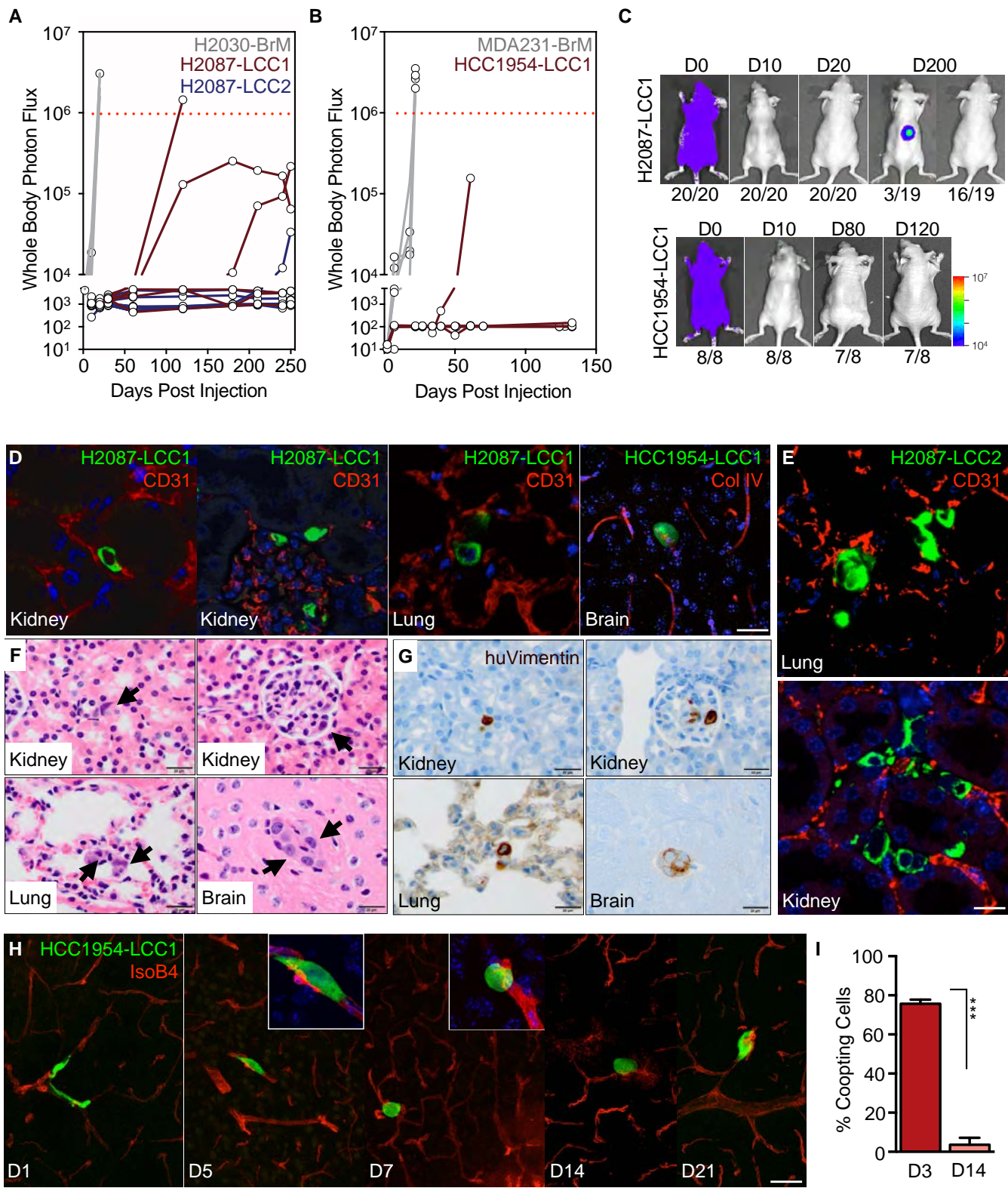


Figure 2

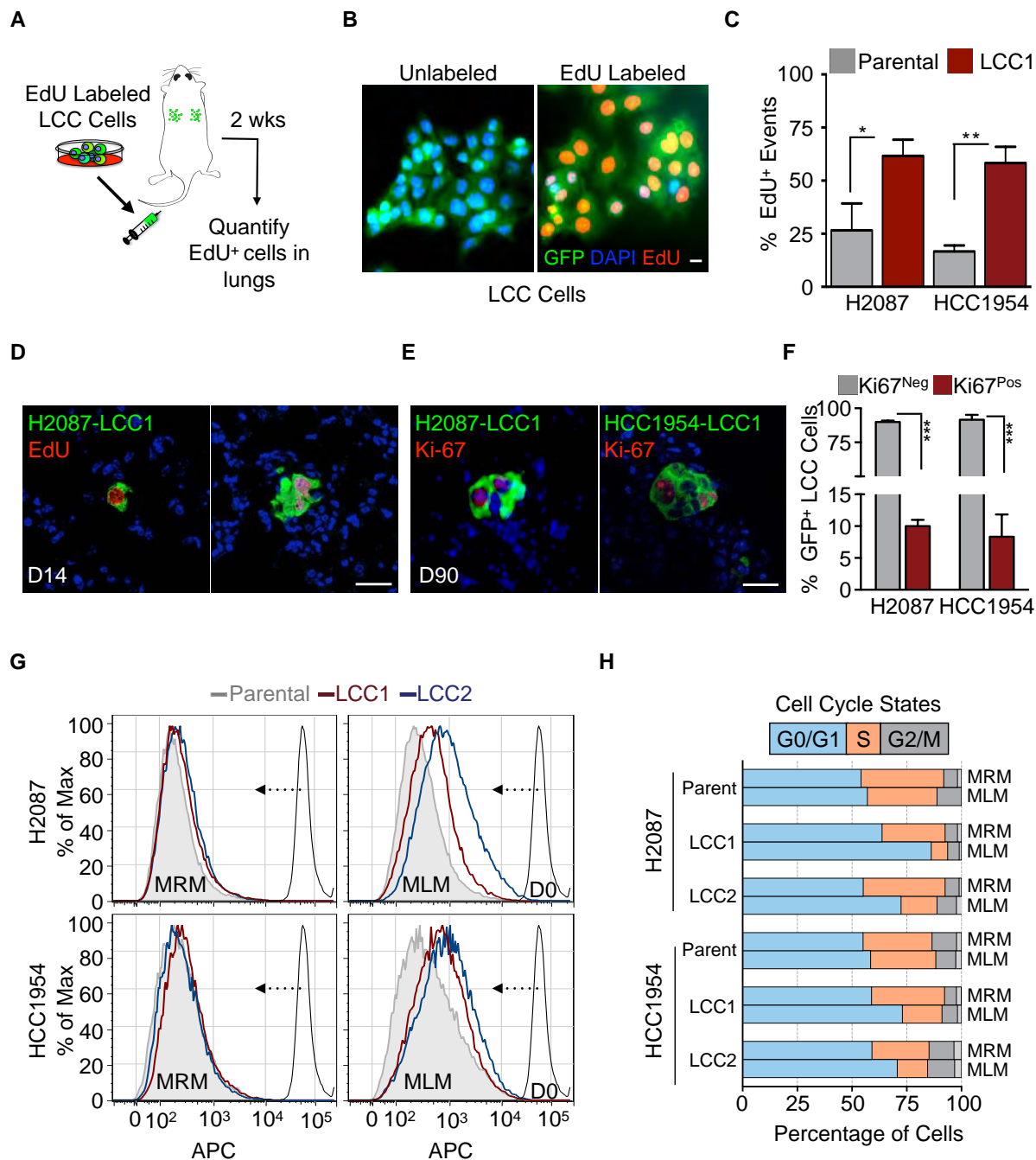


Figure 3

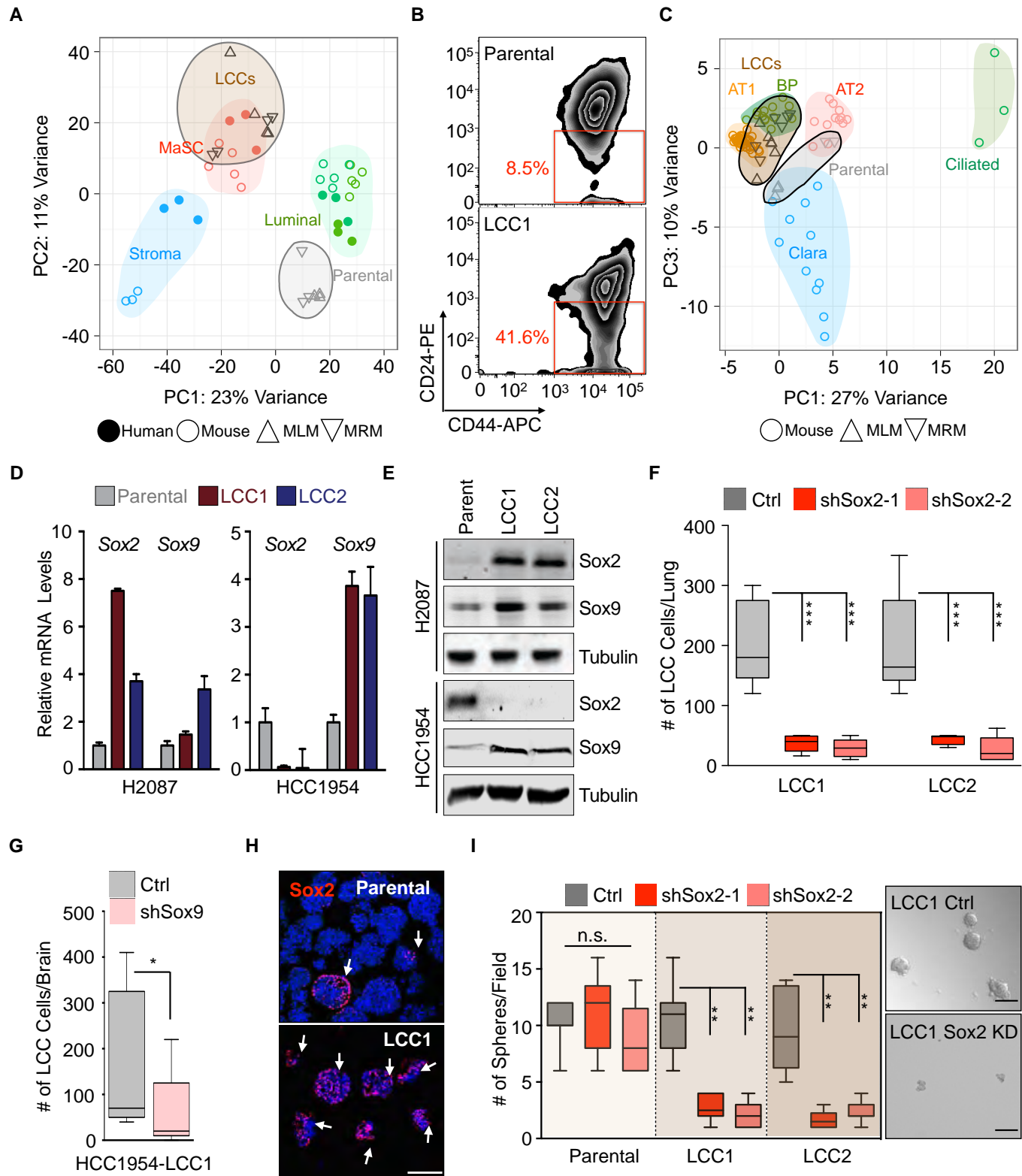


Figure 4

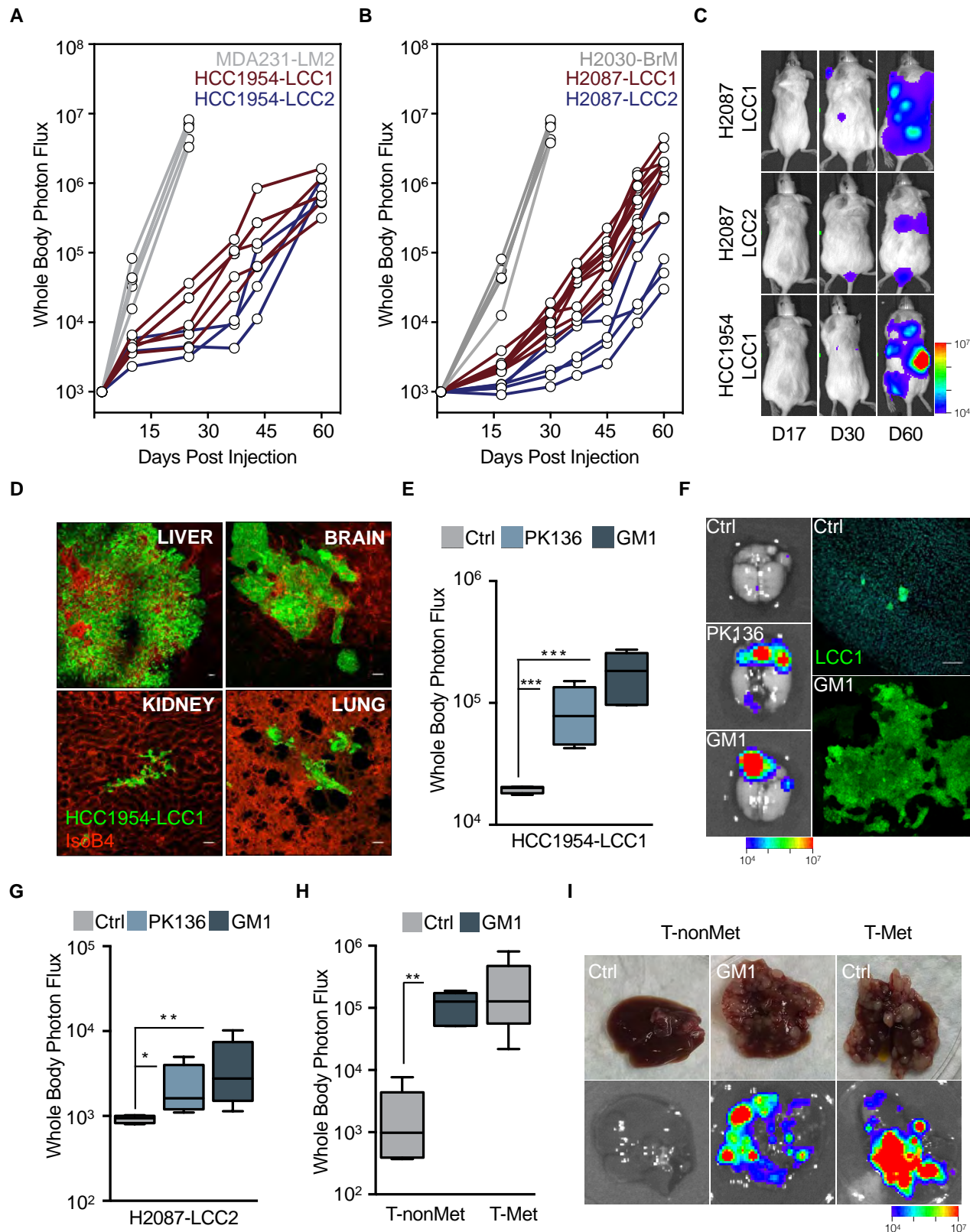


Figure 5

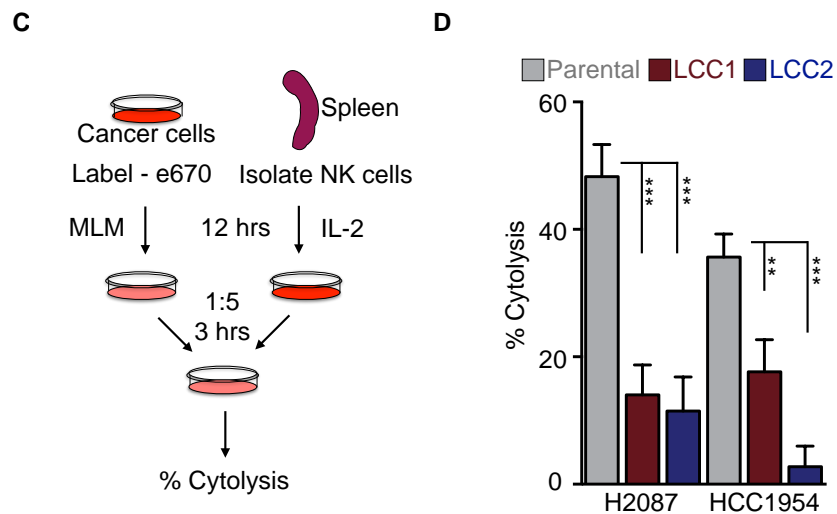
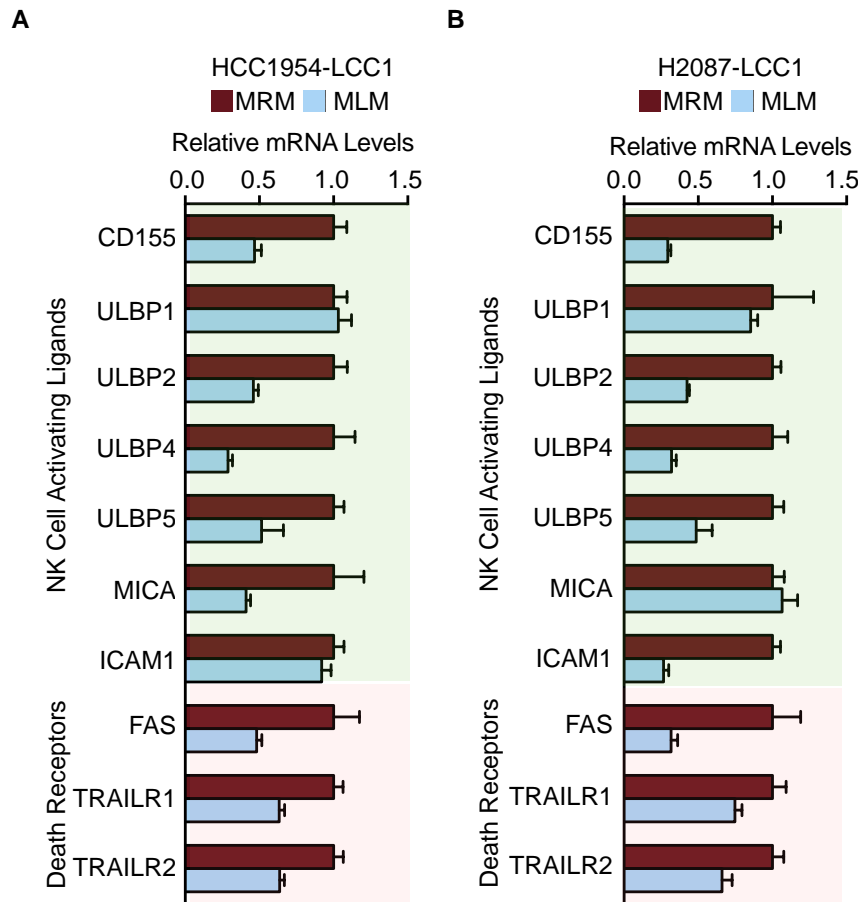


Figure 6

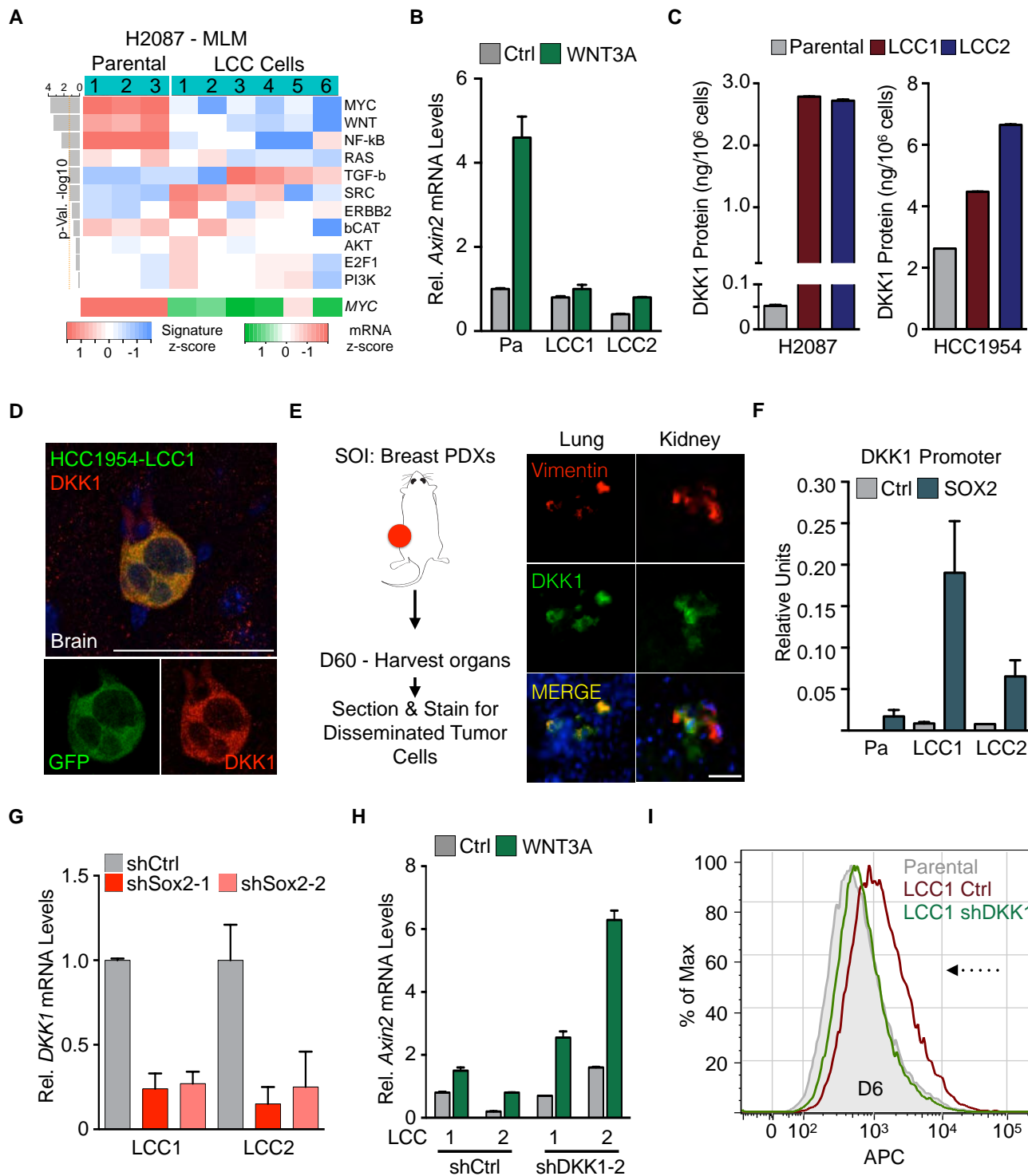


Figure 7

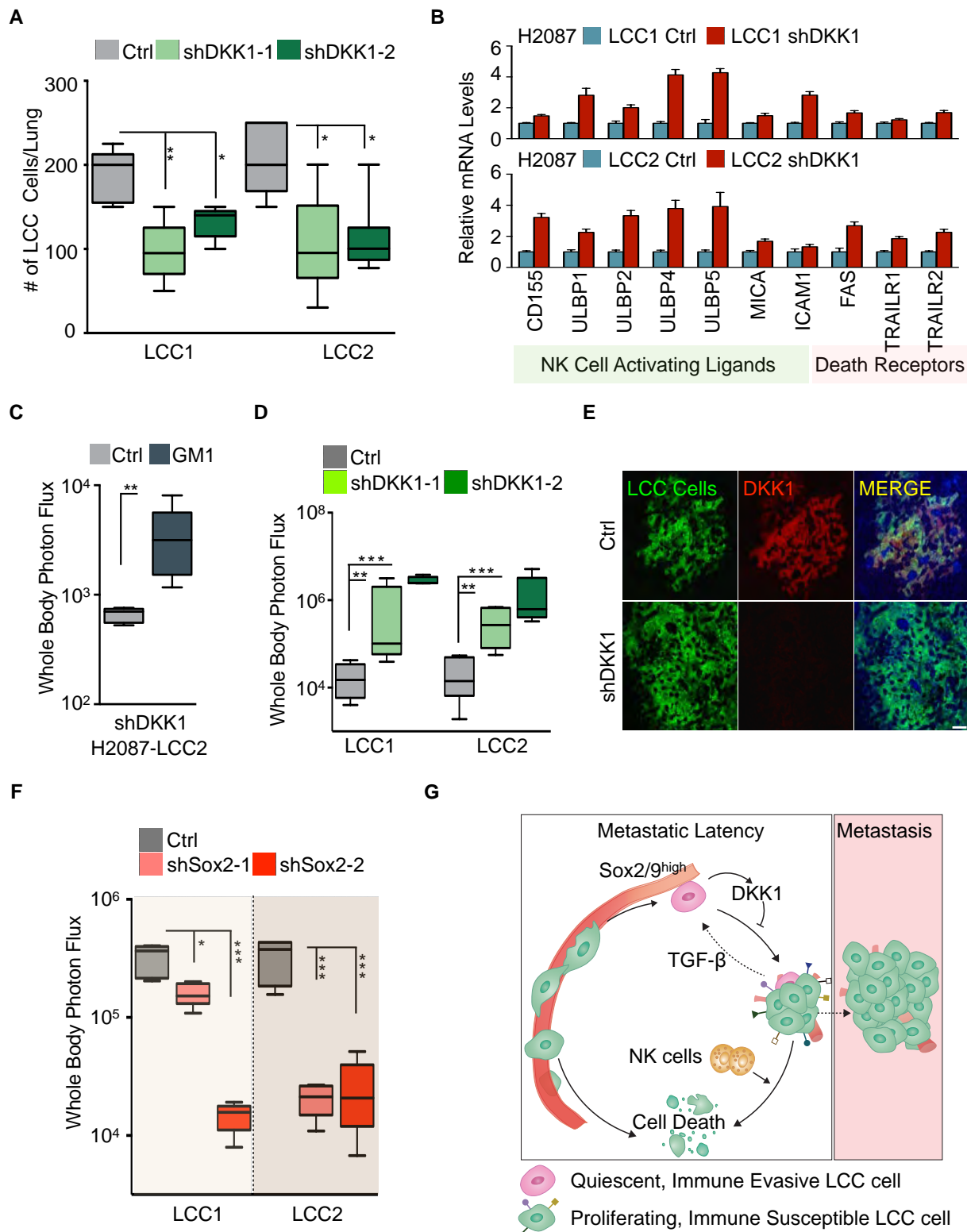
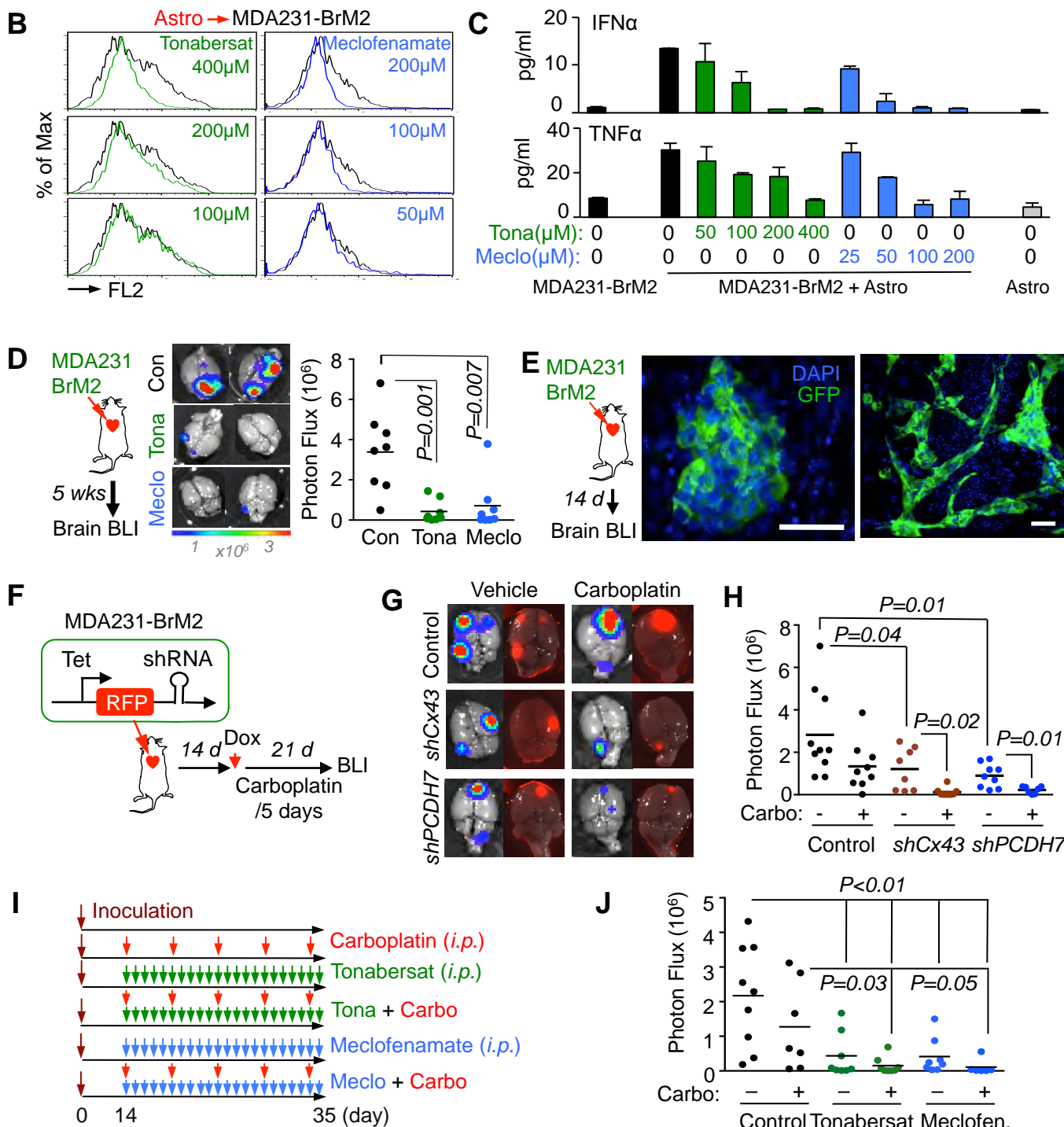
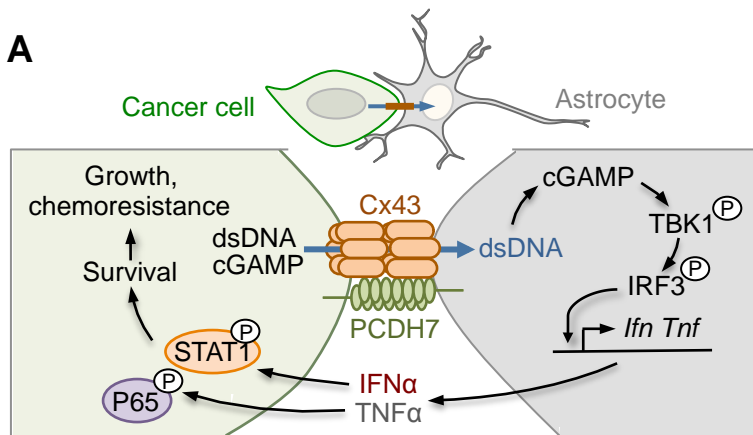


Figure 8



Therapy-induced tumour secretomes promote resistance and tumour progression

Anna C. Obenauf¹, Yilong Zou^{1,2*}, Andrew L. Ji^{1*}, Sakari Vanharanta^{1,3}, Weiping Shu¹, Hubing Shi⁴, Xiangju Kong⁴, Marcus C. Bosenberg^{5,6}, Thomas Wiesner⁷, Neal Rosen⁸, Roger S. Lo⁴ & Joan Massagué¹

Drug resistance invariably limits the clinical efficacy of targeted therapy with kinase inhibitors against cancer^{1,2}. Here we show that targeted therapy with BRAF, ALK or EGFR kinase inhibitors induces a complex network of secreted signals in drug-stressed human and mouse melanoma and human lung adenocarcinoma cells. This therapy-induced secretome stimulates the outgrowth, dissemination and metastasis of drug-resistant cancer cell clones and supports the survival of drug-sensitive cancer cells, contributing to incomplete tumour regression. The tumour-promoting secretome of melanoma cells treated with the kinase inhibitor vemurafenib is driven by down-regulation of the transcription factor FRA1. *In situ* transcriptome analysis of drug-resistant melanoma cells responding to the regressing tumour microenvironment revealed hyperactivation of several signalling pathways, most prominently the AKT pathway. Dual inhibition of RAF and the PI(3)K/AKT/mTOR intracellular signalling pathways blunted the outgrowth of the drug-resistant cell population in BRAF mutant human melanoma, suggesting this combination therapy as a strategy against tumour relapse. Thus, therapeutic inhibition of oncogenic drivers induces vast secretome changes in drug-sensitive cancer cells, paradoxically establishing a tumour microenvironment that supports the expansion of drug-resistant clones, but is susceptible to combination therapy.

Kinase inhibitors such as vemurafenib, erlotinib or crizotinib have shown clinical efficacy in melanoma with BRAF mutations, or in lung adenocarcinoma with EGFR mutations or ALK translocations, respectively^{3–6}. Although complete responses are rare, the vast majority of patients show partial tumour regression or disease stabilization. However, drug resistance invariably develops, and most patients progress within 6–12 months^{3–16}, representing a common complication of targeted therapies that hampers long-term treatment success. The rapid emergence of clinical drug resistance may be facilitated by a small number of pre-existing cancer cells that are intrinsically resistant or poised to adapt to drug treatment quickly^{17–19}. How these minority clones of drug-resistant cells react to the marked changes in the microenvironment during tumour regression is not known. A better understanding of this process could lead to treatments that improve the efficacy of current targeted anti-cancer drugs.

To model therapeutic targeting of heterogeneous tumour cell populations *in vivo*, we mixed a small percentage of vemurafenib-resistant A375 human melanoma cells (A375^R), labelled with a TK-GFP-luciferase (TGL) vector, together with mostly non-labelled, vemurafenib-sensitive A375 cells, and injected the admixture (A375/A375^R, 99.95/0.05%) subcutaneously in mice (Extended Data Fig. 1a). After the tumours were established, we treated the mice with vemurafenib or vehicle, and monitored the growth of resistant cells by bioluminescent imaging (BLI) *in vivo* (Fig. 1a). Although vemurafenib treatment decreased the volume of sensitive tumours (A375 alone) (Extended Data Fig. 1b), the

number of admixed resistant cells in regressing tumours (A375/A375^R) significantly increased compared to vehicle-treated controls (Fig. 1b). Green fluorescent protein (GFP) staining confirmed increased numbers of resistant cells in regressing tumours, and EdU or BrdU staining confirmed their increased proliferation rate compared to the vehicle-treated controls (Fig. 1c and Extended Data Fig. 1c, d). Tumours comprising only resistant cells showed no growth difference when treated with vehicle or vemurafenib (Fig. 1d), indicating that the growth advantage of resistant cells in regressing tumours was not caused by direct effects of vemurafenib on cancer or stromal cells.

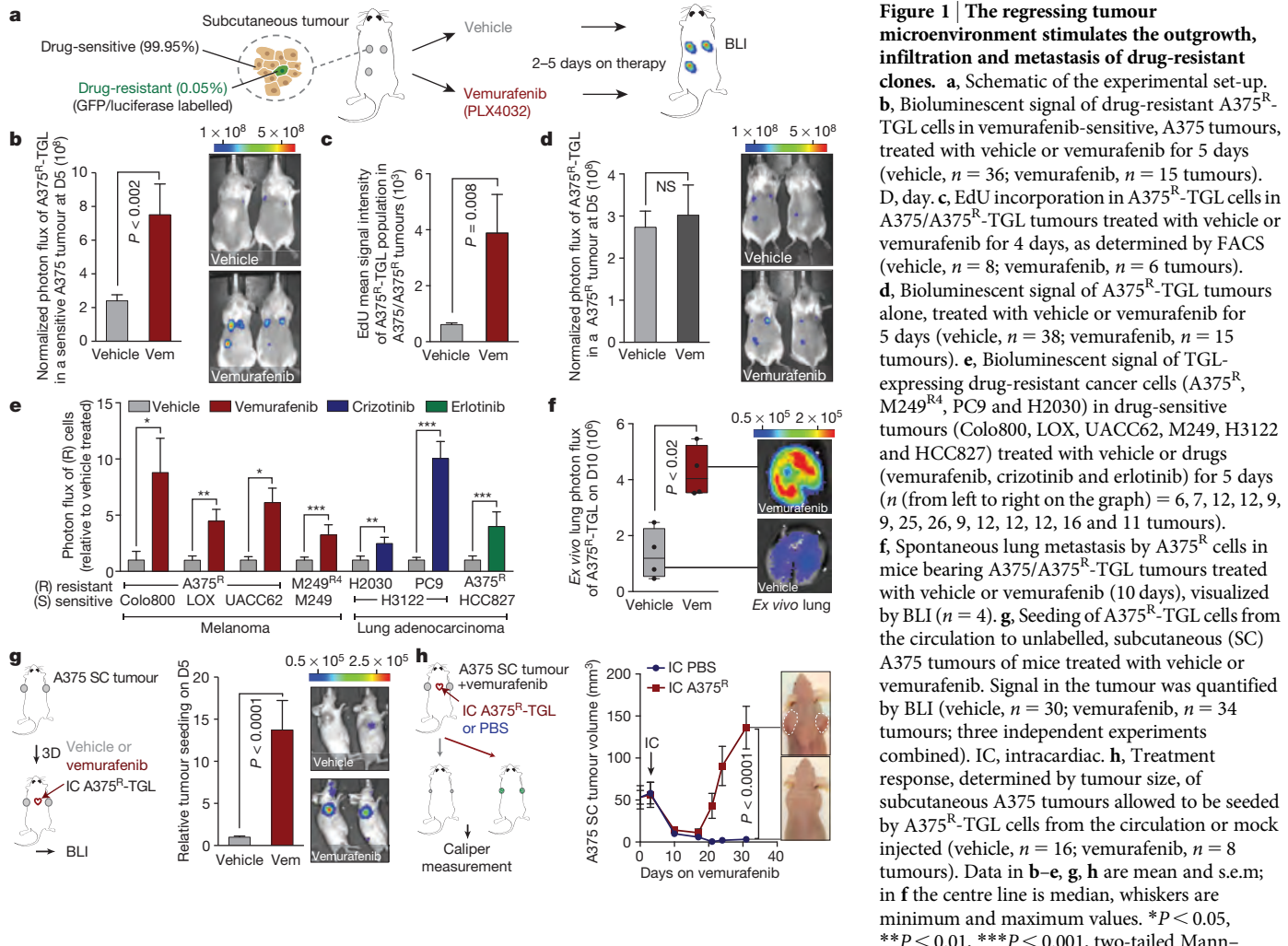
Treatment of mixed A375 and A375^R tumours with dabrafenib, another BRAF inhibitor (RAFi), or doxycycline-induced knockdown of BRAF had similar effects (Extended Data Fig. 1e–g). In line with these findings, A375^R cells co-implanted with other vemurafenib-sensitive melanoma cell lines (Colo800, LOX and UACC62) also showed an up to eightfold growth increase compared to vehicle-treated control groups (Fig. 1e). Growth acceleration of the resistant population in a regressing tumour was also observed in the patient-derived⁸ melanoma cell line M249 and its vemurafenib-resistant derivative M249^{R4}, driven by an NRAS mutation, a clinically relevant resistance mechanism (Fig. 1e and Extended Data Fig. 1h). In immunocompetent mice, vemurafenib treatment of tumours formed by melanoma cell lines derived from *Braf*^{V600E *Cdkn2a*^{−/−} *Pten*^{−/−} mice (YUMM1.1, YUMM1.7) also promoted growth of the admixed vemurafenib-resistant cells (YUMM1.7^R, B16) (Extended Data Fig. 1i, j).}

Crizotinib- or erlotinib-treated mice containing tumours formed by ALK-driven (H3122) or EGFR-driven (HCC827) human lung adenocarcinoma cells, respectively, admixed with minority clones of intrinsically resistant cells from the same cell lineage (lung adenocarcinoma cells H2030 and PC9) or melanoma cells (A375^R) also led to increased outgrowth of the resistant cells (Fig. 1e and Extended Data Fig. 1k–m). Local growth acceleration of resistant cells in the regressing subcutaneous tumours resulted in higher lung metastatic burden (Fig. 1f). Thus, drug-resistant cancer cells benefit from therapeutic targeting of surrounding drug-sensitive cells.

Circulating tumour cells can infiltrate and colonize tumours. This phenomenon, termed self-seeding²⁰, may contribute to the distribution of resistant clones to several metastatic sites. Mice implanted with sensitive A375 tumours were treated with vehicle or vemurafenib, and intracardially injected with TGL-labelled A375^R cells (Fig. 1g). A375^R cells were more efficiently attracted to vemurafenib-treated regressing tumours compared to vehicle-treated controls, with 95% (21 out of 22) and 12.5% (2 out of 16) efficiency, respectively, exhibiting substantial accumulation of resistant cells in regressing tumours by day 5 (Fig. 1g and Extended Data Fig. 1n). To evaluate the contribution of seeding by resistant circulating tumour cells to disease relapse, we intracardially injected resistant A375^R cells or vehicle into tumour-bearing mice and compared

¹Cancer Biology and Genetics Program, Memorial Sloan Kettering Cancer Center, New York, New York 10065, USA. ²Gerstner Sloan Kettering School of Biomedical Sciences, Memorial Sloan Kettering Cancer Center, New York, New York 10065, USA. ³MRC Cancer Unit, University of Cambridge, Cambridge CB2 0XZ, UK. ⁴Division of Dermatology, Department of Medicine and Jonsson Comprehensive Cancer Center, University of California, Los Angeles, California 90095, USA. ⁵Department of Pathology, Yale University School of Medicine, New Haven, Connecticut 06520, USA. ⁶Department of Dermatology, Yale University School of Medicine, New Haven, Connecticut 06520, USA. ⁷Human Oncology and Pathogenesis Program, Memorial Sloan Kettering Cancer Center, New York, New York 10065, USA. ⁸Molecular Pharmacology and Chemistry Program, Memorial Sloan Kettering Cancer Center, New York, New York 10065, USA.

*These authors contributed equally to this work.



the tumour volume during vemurafenib treatment (Fig. 1h). Whereas the unseeded tumours in the control group showed extensive tumour regression, seeding by A375^R cells led to rapid tumour relapse (Fig. 1h). These results suggest that tumours regressing on targeted therapy are potent attractors of resistant circulating tumour cells that may contribute to rapid tumour progression.

Tumours consist of a complex microenvironment composed of immune, stromal and cancer cells²¹. Soluble mediators from this microenvironment can foster cancer growth and therapy resistance^{13,14,22–24}. Considering that drug-sensitive cancer cells are the main population affected by targeted therapy, we proposed that signals derived from sensitive cancer cells in response to kinase inhibitors drive the outgrowth of drug-resistant cells. To test this hypothesis, we established an *in vitro* co-culture system and monitored the growth of TGL-expressing resistant cells (A375^R, H2030) in the absence or presence of sensitive cells treated with kinase inhibitors or vehicle (Fig. 2a). Mimicking our *in vivo* findings, co-culture with vemurafenib-, crizotinib- or erlotinib-treated sensitive cells significantly enhanced the growth of resistant cancer cells (Fig. 2a and Extended Data Fig. 2a–c).

We derived conditioned media (CM) from vemurafenib-sensitive melanoma cells cultured in the absence (CM-vehicle) or presence of vemurafenib (CM-vemurafenib). CM-vemurafenib accelerated the proliferation of drug-resistant cells, with different clinically relevant resistance mechanisms, as determined by cell viability assays and Ki67 staining (Fig. 2b and Extended Data Fig. 2d–f). Similarly, conditioned media from crizotinib- or erlotinib-treated sensitive lung adenocarcinoma cells stimulated proliferation of lung adenocarcinoma cells with intrinsic or

acquired resistance (Fig. 2c) and across different cell lineages (Extended Data Fig. 2g). In addition, CM-vemurafenib elicited increased cell migration in transwell migration and monolayer gap-closing assays (Fig. 2d and Extended Data Fig. 2h–k). CM-vemurafenib was also active on vemurafenib-sensitive cancer cells, increasing survival and suppressing the apoptotic caspase activity up to 100-fold in these cells when treated with vemurafenib *in vitro* (Fig. 2e, f). Because all biologically active conditioned media was collected before cell death or senescence, it is likely that the secretome is actively produced as a result of oncogene inhibition (Extended Data Fig. 2l, m). These results demonstrate that BRAF, ALK and EGFR mutant cells respond to therapeutic stress under targeted therapy by secreting factors that support the survival of drug-sensitive cells and accelerate the growth of drug-resistant minority clones. The effects of this reactive secretome may augment previously reported resistance mechanisms including relief of feedback inhibition of intracellular signalling^{11,25}, upregulation of receptor tyrosine kinases²⁶, or release of stromal cytokines¹⁴ that protect the drug-sensitive cells.

To identify relevant components and regulators of the reactive secretome, we analysed gene expression changes in sensitive A375 melanoma cells at different time points after vemurafenib exposure *in vitro*. After 6 h on vemurafenib, 473 genes showed altered expression, and pathway analysis revealed that these genes were enriched for transcriptional regulators (Fig. 3a, b, Extended Data Fig. 3a, b and Supplementary Table 1). After 48 h, more than one-third of the transcriptome was differentially expressed ($>5,000$ genes; 405 genes encoding for proteins in the extracellular region, Gene Ontology (GO) accession 0005576), significantly overlapping with the gene expression changes of A375

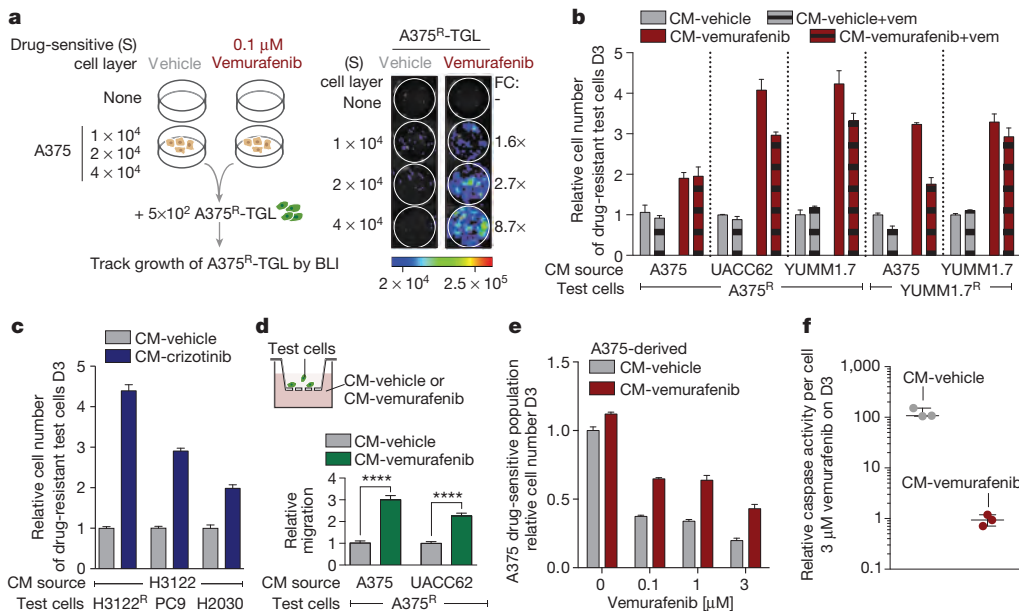


Figure 2 | The secretome of RAF and ALK inhibitor-treated tumour cells increases proliferation and migration of drug-resistant cells and supports the survival of drug-sensitive cells. **a**, Schematic (left) and representative BLI images (right) after 7 days of co-culture. Average fold change (FC) of BLI signal from A375^R-TGL cells in vemurafenib-treated wells relative to vehicle-treated control wells is depicted on the right ($n = 4$ biological replicates). **b, c**, Conditioned media (CM) was derived from drug-sensitive cells, treated with vehicle, vemurafenib or crizotinib. Drug-resistant cells were grown in this conditioned media and the cell number was determined on day 3. Drug-sensitive and drug-resistant cell lines and drugs used to generate

conditioned media as indicated. $n = 3$ (**b**) and 6 (**c**) biological replicates. **d**, Schematic diagram of the migration assay (top) and relative migration of A375^R cells towards conditioned media from different sources as indicated (bottom, $n = 10$ fields of vision (FOV)). $****P < 0.0001$, two-tailed Mann-Whitney U test. **e**, Survival assay of drug-sensitive A375 cells cultured in conditioned media and treated with vemurafenib, assessed on day 3 ($n = 3$ biological replicates). **f**, Apoptosis rate of A375 cells cultured in conditioned media and treated with vemurafenib (3 μ M) ($n = 3$ biological replicates). Data are mean and s.e.m.

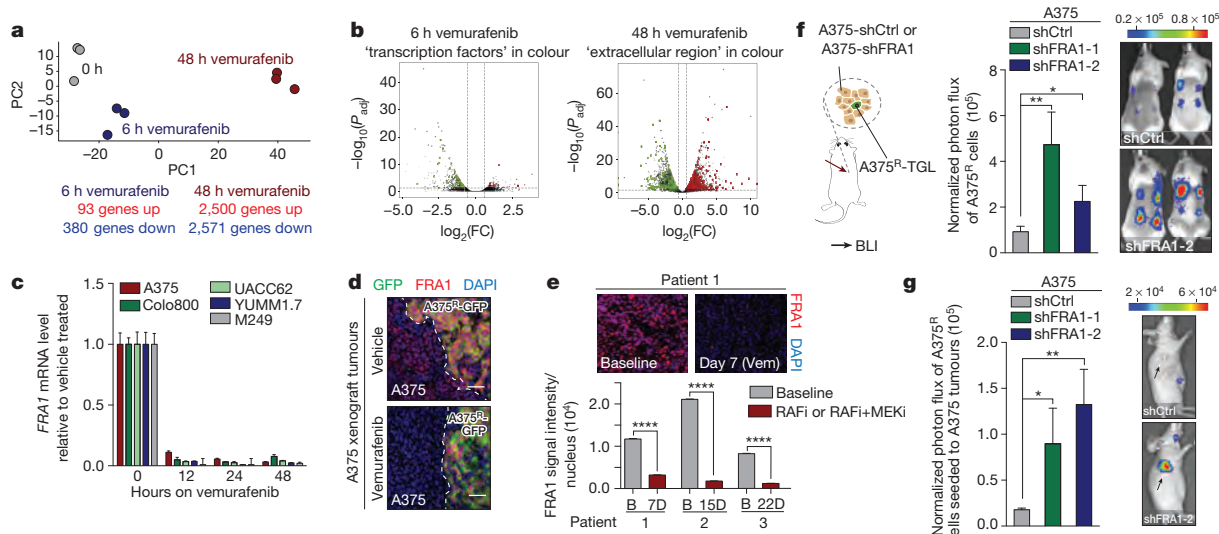


Figure 3 | FRA1 downregulation during RAFi treatment drives the reactive secretome. **a**, Principal component (PC) analysis of drug-sensitive A375 cells treated *in vitro* with vehicle or vemurafenib for 6 or 48 h. **b**, Volcano plots show genes significantly deregulated by vemurafenib treatment after 6 h (left) or 48 h (right). Transcription factors (TF) and gene products in the extracellular region are depicted in green (downregulated) and red (upregulated) ($n = 3$ tumours). P_{adj} , adjusted P value. **c**, Relative mRNA levels of FRA1 during vemurafenib exposure [0.1–1 μ M]. **d**, Representative immunofluorescence staining of A375/A375^R tumours for GFP (A375^R, green) and FRA1 (red) after vehicle or vemurafenib treatment (5 days). DAPI, 4',6-diamidino-2-phenylindole. Scale bars, 50 μ m. **e**, Top, representative

immunofluorescence staining for FRA1 (red) of melanoma biopsy sections of patient 1. Original magnification, $\times 20$. Bottom, nuclear FRA1 staining was quantified in three melanoma patients before (B) and early-on therapy. RAFi and MEKi denote RAF and MEK inhibitors, respectively. **f**, Bioluminescent signal of A375^R-TGL cells 6 days after subcutaneous co-implantation with A375 cells expressing control (shCtrl) or two independent shRNAs for FRA1 (shFRA1-1 and shFRA1-2) ($n = 16$ tumours). **g**, Seeding of A375^R-TGL cells to unlabelled tumours expressing control or two independent shRNAs for FRA1, determined by BLI (vehicle, $n = 10$; shFRA1-1, $n = 10$; shFRA1-2, $n = 8$ tumours). Data are mean and s.e.m. $*P < 0.05$, $**P < 0.01$, $****P < 0.0001$, Student's t -test.

tumours *in vivo* after 5 days of vemurafenib treatment (Fig. 3a, b and Extended Data Fig. 3c). Similar extensive gene expression changes were observed in Colo800 and UACC62 melanoma cells treated with vemurafenib and H3122 lung adenocarcinoma cells treated with crizotinib (Extended Data Fig. 3d). Despite different cell lineages, different oncogenic drivers, and different targeted therapies we observed a significant overlap between the secretome of melanoma and lung adenocarcinoma cells ($P < 9.11 \times 10^{-5}$) (Extended Data Fig. 3e-h and Supplementary Table 1). Furthermore, changes in the secretome of vemurafenib-sensitive melanoma cells coincided with changes in the immune cell composition (Extended Data Fig. 4a, b), and with changes of soluble mediators derived from murine stromal cells such as IGF1 and HGF (Extended Data Fig. 4c, d). These data indicate a therapy-induced secretome (TIS), a response that consists of many up- and downregulated secreted factors, permeates the regressing tumour microenvironment and stimulates cancer cells, probably also stromal cells.

To identify molecular drivers of the A375-TIS in response to vemurafenib, we integrated the data of differentially expressed transcription factors after 6 h of vemurafenib treatment with the transcription factor binding motifs that were enriched at the promoters of differentially expressed genes in the secretome after 48 h (Fig. 3a, b). This analysis highlighted FRA1 (also known FOSL1), a member of the AP1 transcription factor complex and effector of the ERK pathway²⁷, as one of the putative upstream regulators of the TIS (Extended Data Fig. 5a). *FRA1* was downregulated in all drug-sensitive cells, but not in resistant cells, treated with vemurafenib, crizotinib and erlotinib (Fig. 3c, d and Extended Data Fig. 5b-d). Biopsies from melanoma patients early during RAFi treatment confirmed RAFi-induced *FRA1* downregulation in clinical samples (Fig. 3e, Extended Data Fig. 5e and Extended Data Table 1).

To test the functional role of *FRA1* in modulating the TIS, we used RNA interference (RNAi) to inhibit *FRA1* expression. Co-culture and conditioned media assays using A375 cells expressing short hairpin

RNAs targeting *FRA1* (sh*FRA1*) showed similar growth-accelerating and chemotactic activity on A375^R cells as vemurafenib treatment (Extended Data Fig. 6a-d). In line with these results, *FRA1* knockdown in A375 cells induced transcriptional changes similar to those induced by vemurafenib (Extended Data Fig. 6e). A375^R cells co-implanted with A375 or UACC62 cells expressing sh*FRA1* also demonstrated increased growth *in vivo* (Fig. 3f and Extended Data Fig. 6f). A375-sh*FRA1* tumours attracted significantly more resistant cells from the circulation than tumours expressing the control vector (Fig. 3g). Thus, *FRA1* downregulation drives the induction of the tumour-promoting secretome of vemurafenib-treated cancer cells.

To determine the effect of the reactive secretome on the drug-resistant tumour subpopulation in a regressing tumour, we expressed the ribosomal protein L10a (RPL10a) fused to enhanced green fluorescent protein (eGFP-RPL10a) in A375^R cells, allowing the specific retrieval of transcripts from A375^R cells by polysome immunoprecipitation for subsequent RNA-sequencing (RNA-seq) analysis²⁸ (Fig. 4a). In line with the *in vivo* phenotype of accelerated growth, the gene expression pattern of resistant cells in the regressing microenvironment was enriched for biological processes involved in cell viability, proliferation and cell movement (Extended Data Fig. 7a). Pathway analysis of the expression data suggested activation of several pathways including PI(3)K/AKT, BMP-SMAD and NF κ B (Fig. 4b). The hyperactivity of the PI(3)K/AKT pathway in this context also suggested a potential vulnerability of the cells to PI(3)K/mTOR inhibitors (Extended Data Fig. 7b). The pathway-analysis-based prediction of PI(3)K/AKT activation was also reflected at the protein level in both resistant and sensitive cells in the presence of CM-vemurafenib *in vitro* and under vemurafenib treatment *in vivo* (Fig. 4c and Extended Data Fig. 7c, d). Moreover, PI(3)K/AKT emerged as the dominant TIS responsive pathway in a targeted immunoblot analysis of survival pathways *in vitro* (Extended Data Fig. 7e).

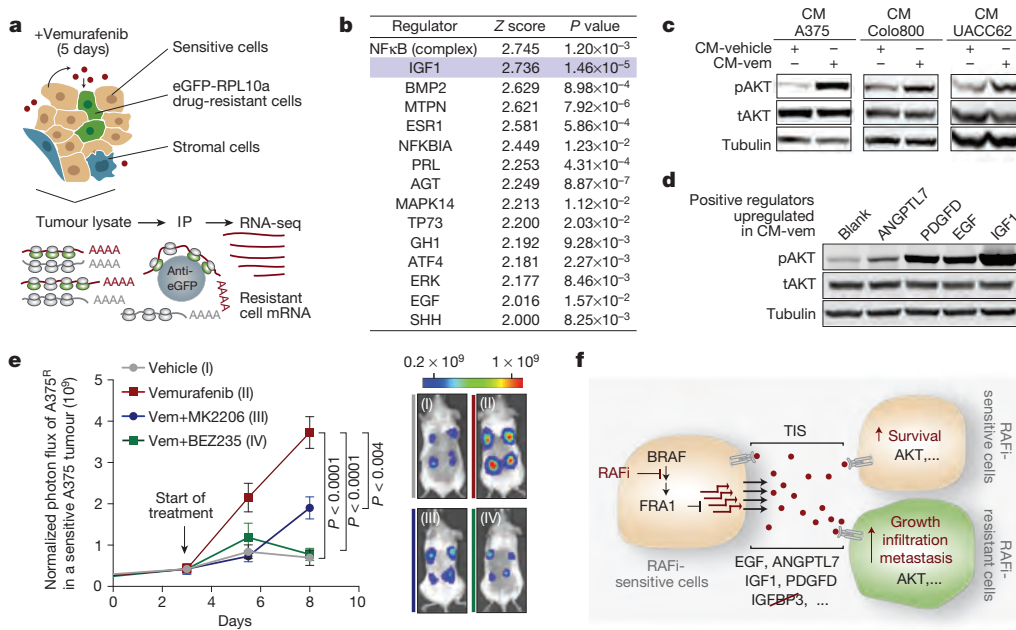


Figure 4 | The therapy-induced secretome in melanoma promotes relapse by activating the AKT pathway in resistant cells. a, Schematic diagram showing the isolation of polysome-associated transcripts from resistant cells by translating ribosome affinity profiling (TRAP) from tumours during treatment. IP, immunoprecipitation. b, Ingenuity upstream regulator analysis of gene expression profiles from A375^R cells responding to a regressing tumour microenvironment (5 days of treatment; $n = 3$ tumours). c, Phosphorylation status of AKT^{S473} (pAKT) in A375^R cells, stimulated for 15 min with various conditioned media, as indicated by immunoblotting. tAKT, total AKT. d, Phosphorylation status of AKT^{S473} in A375^R cells after stimulation with

positive regulators of the AKT pathway, upregulated in the melanoma TIS; ANGPTL7 (5 μ g ml⁻¹, 30 min; upregulated in A375, Colo800, UACC62), PDGFD (10 ng ml⁻¹, 10 min; upregulated in Colo800), EGF (10 ng ml⁻¹, 10 min; upregulated in A375) and IGF1 (10 ng ml⁻¹, 10 min; upregulated in UACC62). e, Mice bearing A375/A375^R-TGL tumours were treated with drugs, and growth of A375^R cells was followed by BLI (vehicle, $n = 14$; vemurafenib, $n = 16$; vemurafenib and BEZ235, $n = 16$; vemurafenib and MK2206, $n = 8$ tumours). f, Graphical summary of the findings. Data are mean and s.e.m. P values calculated using a two-tailed Mann-Whitney U test.

The TIS contained many mediators directly or indirectly activating the AKT pathway. Positive mediators that were upregulated during therapy included IGF1, EGF, ANGPTL7 and PDGFD, each of which activated the AKT pathway *in vitro* (Fig. 4d). IGF1, one of the most potent activators of the AKT pathway, is also abundantly expressed in the tumour stroma and is further upregulated during targeted therapy (Extended Data Figs 4c and 7f). In addition, levels of IGFBP3, a negative regulator of IGF1, were markedly reduced in the TIS of all investigated cell lines, favouring increased AKT pathway activation in the presence of IGF1 and stimulation of proliferation of resistant cells *in vivo* (Extended Data Fig. 7f–k).

To test the role of AKT activation as a mediator of TIS-induced tumour proliferation, we combined vemurafenib with AKT/PI(3)K/mTOR inhibitors. In co-culture and proliferation experiments using conditioned media, dual inhibition of the MAPK and AKT pathway diminished the growth benefit of the TIS (Extended Data Fig. 8a, b). We then treated mice with A375/A375^R or A375^R tumours with vemurafenib and AKT (MK2206) or PI(3)K/mTOR inhibitors (BEZ235). The combined inhibition of MAPK and PI(3)K/AKT/mTOR pathways significantly blunted the outgrowth of vemurafenib-resistant cells in the A375/A375^R tumours (Fig. 4e). The growth inhibition was specific for the amplified proliferation in the regressing tumour microenvironment and had no effects on the growth of resistant cells alone (Extended Data Fig. 8c). Furthermore, the outgrowth of resistant A375^R cells in tumour seeding assays was significantly reduced when regressing tumours were co-treated with BEZ235 (Extended Data Fig. 8d). Thus, the TIS-induced proliferation is susceptible to therapeutic targeting.

The limited effectiveness of targeted therapies has been attributed to intracellular feedback loops and specific cytokines that support the survival of drug-sensitive cells. From these residual tumours, clones emerge that are intrinsically resistant to targeted therapy and are ultimately responsible for clinical relapse. Our work demonstrates that targeted inhibition of a cancer driver pathway can paradoxically promote these two aspects of drug resistance via induction of a complex, reactive secretome. This TIS not only enhances the survival of drug-sensitive cells, but also acutely accelerates the expansion and dissemination of drug-resistant clones. Rather than a cell death by-product^{29,30}, the TIS is a live-cell response to inhibition of an oncogenic driver pathway, mediated by a concrete transcriptional program, and defined by specific alterations of intracellular signalling networks (Fig. 4f).

Our identification of AKT signalling as a mediator of TIS-induced tumour progression in BRAF-driven melanoma is in line with AKT activation in tumours observed in the clinic during vemurafenib treatment¹⁶. Patients treated with BRAF inhibitor rarely show full tumour regression^{3,4}, and the remaining drug-responsive tumour cells may remain a source of TIS for the duration of the treatment. Our results provide a rationale for combining PI(3)K/AKT/mTOR pathway inhibitors with inhibitors of the MAPK pathway in the treatment of these tumours. However, the breadth of the TIS and the generality of our findings across different cell lineages, drugs (vemurafenib, crizotinib and erlotinib), and resistance mechanisms suggest that durable responses may require the combination of this type of agents with a radically different therapeutic modality.

Online Content Methods, along with any additional Extended Data display items and Source Data, are available in the online version of the paper; references unique to these sections appear only in the online paper.

Received 26 August 2014; accepted 12 February 2015.

Published online 25 March 2015.

1. Engelman, J. A. & Settleman, J. Acquired resistance to tyrosine kinase inhibitors during cancer therapy. *Curr. Opin. Genet. Dev.* **18**, 73–79 (2008).
2. Holohan, C., Van Schaeybroeck, S., Longley, D. B. & Johnston, P. G. Cancer drug resistance: an evolving paradigm. *Nature Rev. Cancer* **13**, 714–726 (2013).
3. Chapman, P. B. et al. Improved survival with vemurafenib in melanoma with BRAF V600E mutation. *N. Engl. J. Med.* **364**, 2507–2516 (2011).

4. Sosman, J. A. et al. Survival in BRAF V600-mutant advanced melanoma treated with vemurafenib. *N. Engl. J. Med.* **366**, 707–714 (2012).
5. Shaw, A. T. & Engelman, J. A. ALK in lung cancer: past, present, and future. *J. Clin. Oncol.* **31**, 1105–1111 (2013).
6. Zhou, C. et al. Erlotinib versus chemotherapy as first-line treatment for patients with advanced EGFR mutation-positive non-small-cell lung cancer (OPTIMAL, CTONG-0802): a multicentre, open-label, randomised, phase 3 study. *Lancet Oncol.* **12**, 735–742 (2011).
7. Villanueva, J. et al. Acquired resistance to BRAF inhibitors mediated by a RAF kinase switch in melanoma can be overcome by cotargeting MEK and IGF-1R/PI3K. *Cancer Cell* **18**, 683–695 (2010).
8. Nazarian, R. et al. Melanomas acquire resistance to B-RAF(V600E) inhibition by RTK or N-RAS upregulation. *Nature* **468**, 973–977 (2010).
9. Poulikakos, P. I. et al. RAF inhibitor resistance is mediated by dimerization of aberrantly spliced BRAF(V600E). *Nature* **480**, 387–390 (2011).
10. Wagle, N. et al. Dissecting therapeutic resistance to RAF inhibition in melanoma by tumor genomic profiling. *J. Clin. Oncol.* **29**, 3085–3096 (2011).
11. Lito, P. et al. Relief of profound feedback inhibition of mitogenic signalling by RAF inhibitors attenuates their activity in BRAFV600E melanomas. *Cancer Cell* **22**, 668–682 (2012).
12. Shi, H. et al. Melanoma whole-exome sequencing identifies V600EB-RAF amplification-mediated acquired B-RAF inhibitor resistance. *Nature Commun.* **3**, 724–728 (2012).
13. Wilson, T. R. et al. Widespread potential for growth-factor-driven resistance to anticancer kinase inhibitors. *Nature* **487**, 505–509 (2012).
14. Straussman, R. et al. Tumour micro-environment elicits innate resistance to RAF inhibitors through HGF secretion. *Nature* **487**, 500–504 (2012).
15. Johannessen, C. M. et al. A melanocyte lineage program confers resistance to MAP kinase pathway inhibition. *Nature* **504**, 138–142 (2013).
16. Shi, H. et al. A novel AKT1 mutant amplifies an adaptive melanoma response to BRAF inhibition. *Cancer Discovery* **4**, 69–79 (2014).
17. Diaz, L. A. Jr et al. The molecular evolution of acquired resistance to targeted EGFR blockade in colorectal cancers. *Nature* **486**, 537–540 (2012).
18. Shi, H. et al. Acquired resistance and clonal evolution in melanoma during BRAF inhibitor therapy. *Cancer Discovery* **4**, 80–93 (2014).
19. Sharma, S. V. et al. A chromatin-mediated reversible drug-tolerant state in cancer cell subpopulations. *Cell* **141**, 69–80 (2010).
20. Kim, M. Y. et al. Tumor self-seeding by circulating cancer cells. *Cell* **139**, 1315–1326 (2009).
21. Villanueva, J. & Herlyn, M. Melanoma and the tumor microenvironment. *Curr. Oncol. Rep.* **10**, 439–446 (2008).
22. Acharya, S. et al. A CXCL1 paracrine network links cancer chemoresistance and metastasis. *Cell* **150**, 165–178 (2012).
23. Sun, Y. et al. Treatment-induced damage to the tumor microenvironment promotes prostate cancer therapy resistance through WNT16B. *Nature Med.* **18**, 1359–1368 (2012).
24. Lee, H. J. et al. Drug resistance via feedback activation of Stat3 in oncogene-addicted cancer cells. *Cancer Cell* **26**, 207–221 (2014).
25. Lito, P., Rosen, N. & Sotir, D. B. Tumor adaptation and resistance to RAF inhibitors. *Nature Med.* **19**, 1401–1409 (2013).
26. Sun, C. et al. Reversible and adaptive resistance to BRAF(V600E) inhibition in melanoma. *Nature* **508**, 118–122 (2014).
27. Joseph, E. W. et al. The RAF inhibitor PLX4032 inhibits ERK signaling and tumor cell proliferation in a V600E BRAF-selective manner. *Proc. Natl. Acad. Sci. USA* **107**, 14903–14908 (2010).
28. Heiman, M. et al. A translational profiling approach for the molecular characterization of CNS cell types. *Cell* **135**, 738–748 (2008).
29. Fuchs, Y. & Steller, H. Programmed cell death in animal development and disease. *Cell* **147**, 742–758 (2011).
30. Kurtova, A. V. et al. Blocking PGE₂-induced tumour repopulation abrogates bladder cancer chemoresistance. *Nature* **517**, 209–213 (2015).

Supplementary Information is available in the online version of the paper.

Acknowledgements We thank members of the Massagué laboratory for discussions; L. Sevenich and L. Akkari for technical advice. This work was supported by grants from the AACR (SU2C) to R.S.L., the MSK Metastasis Research Center, the NIH (CA163167 and CA129243), the Congressionally Directed Medical Research Program of the Department of Defense, the Howard Hughes Medical Institute, and the Cancer Center Support Grant P30 CA008748 to J.M., A.C.O. was an Erwin Schrödinger Fellowship awardee (J3013, FWF, Austrian Science Fund). A.L.J. was a Medical Research Fellow of the Howard Hughes Medical Institute. S.V. is supported by the Medical Research Council.

Author contributions A.C.O. and J.M. conceived the project, designed the experiments and wrote the paper. A.C.O. performed experiments and computational analysis. A.L.J., Y.Z., W.S. and T.W. assisted with experiments. Y.Z. and S.V. performed computational analysis. M.C.B. provided cell lines. X.K., H.S. and R.S.L. provided patient samples. N.R. provided clinical expertise, cell lines and drugs. All authors interpreted data, discussed results, and revised the manuscript.

Author Information All RNA-seq data has been deposited in the Gene Expression Omnibus database under accession number GSE64741. Reprints and permissions information is available at www.nature.com/reprints. The authors declare no competing financial interests. Readers are welcome to comment on the online version of the paper. Correspondence and requests for materials should be addressed to J.M. (j-massague@ski.mskcc.org).

METHODS

Cell culture. A375, M249 (ref. 8) and B16 cells were cultured in DMEM media; Colo800, UACC62, SKMEL239-clone3, LOX, PC9, H2030, H3122 and HCC827 cells were cultured in RPMI media. YUMM1.1 and YUMM1.7 were cultured in DMEM/F12 media. GPG29 and 293T cells were used for retrovirus and lentivirus production, respectively. Both were maintained in DMEM media. All media contained 10% FBS, 2 mM L-glutamine, 100 IU ml⁻¹ penicillin/streptomycin and 1 µg ml⁻¹ amphotericin B, the media for GPG29 contained in addition 0.3 mg ml⁻¹ G418, 20 ng ml⁻¹ doxycycline and 2 µg ml⁻¹ puromycin. All cells were grown in a humidified incubator at 37 °C with 5% CO₂ and were tested regularly for mycoplasma contamination. All cell lines used were negative for mycoplasma.

To generate vemurafenib-resistant melanoma cell lines, vemurafenib-sensitive cell lines were seeded at low density and exposed to 1–3 µM vemurafenib (LC-Labs). After approximately 8 weeks of continuous vemurafenib exposure, we derived resistant cell clones that were maintained on vemurafenib (1 µM vemurafenib for M249^R, Colo800^R, LOX^R, UACC62^R; 2 µM vemurafenib for A375^R, YUMM1.7^R). The same protocol was performed to generate a crizotinib-resistant cell line from H3122 lung adenocarcinoma cells, which were selected and maintained with 300 nM crizotinib. Drug-sensitive and resistant melanoma cell lines from A375, Colo800, UACC62 and YUMM1.7 and the drug sensitive lung adenocarcinoma cell lines H3122 and HCC827 were exposed to increasing doses of vemurafenib and the number of cells was determined after 3 days and pERK levels after 1 h of vemurafenib, crizotinib or erlotinib exposure (Extended Data Fig. 9a–j). Receptor status was determined by western blot and showed an increase in EGFR expression levels in all resistant lines examined as well as an increase in MET receptor expression in A375^R and UACC62^R cells compared to their parental, drug-sensitive cells (Extended Data Fig. 9k).

For co-culture assays sensitive cells were plated in 12-well or 24-well plates and allowed to adhere overnight in regular growth media. Media was then replaced with low serum (2% FBS) media containing vehicle, 0.1 µM vemurafenib, 0.3 µM crizotinib or 0.01 µM erlotinib. For control wells media containing vehicle or 0.1 µM vemurafenib, 0.3 µM crizotinib, or 0.01 µM erlotinib was plated at the same time. After 48 h, TGL-expressing, resistant cells were plated on top of the vehicle/drug treated cells or in media-only control wells. Media containing vehicle/drug was replenished every 48 h. After 7 days, luciferin [150 µg ml⁻¹] was added to the wells and luciferase-signal of resistant cells was determined by BLI using a Xenogen Spectrum imaging machine (Perkin Elmer). Co-culture experiments were independently performed at least twice and a representative experiment is shown.

To generate conditioned media, 2.3 × 10⁶ and 6.4 × 10⁶ drug-sensitive cells were plated on 15-cm dishes in regular growth media and allowed to adhere overnight. The media was then replaced by low serum media containing vehicle or vemurafenib (0.1 µM for A375 cells, 1 µM for all other cell lines), on dishes containing 2.3 × 10⁶ and 6.4 × 10⁶ drug-sensitive cells, respectively. The same procedure was followed for generation of conditioned media from H3122 (crizotinib, 0.3 or 1 µM) or HCC827 (erlotinib 0.01 µM) lung adenocarcinoma cells. After 72 h, cells on both plates had reached equal confluence of ~80% and conditioned media was collected, centrifuged at 1,000 r.p.m. for 5 min, filtered, and aliquots were stored at –80 °C until further use. Key proliferation and migration experiments yielded the same results when performed with conditioned media in which the same number of drug-sensitive cells (3.2 × 10⁶) was plated initially, which resulted in higher cell confluence in the vehicle-treated dish at time of conditioned media collection.

Proliferation, survival and apoptosis assays. Around 1,000–3000 cells were plated in a 96-well plate, allowed to adhere overnight, and then incubated with either fresh or conditioned media containing vemurafenib or additional drugs as indicated. After 72 h, the number of cells was determined using a CelltiterGlo assay and the caspase 3/7 activity using a CaspaseGlo assay (Promega) according to the manufacturer's instructions. Caspase 3/7 activity was normalized to the number of cells present. All experiments with melanoma test cells and melanoma conditioned media were performed at least three times, experiments with lung adenocarcinoma cell lines were performed at least twice. Representative experiments are shown.

Boyden chamber transwell migration assay/gap closure assay. Transwell migration assays were performed as described previously with minor modifications³¹. In brief, serum-starved cells (0.2% FBS, overnight) were labelled with cell tracker green (Invitrogen) for 30 min at 37 °C and allowed to recover for 1 h. Cells (25,000–50,000) were then seeded onto membrane inserts with 8-µm pores and fluorescence blocking filters (Falcon). The number of cells migrated through the pores of the membrane was scored after 5–24 h using an Evos microscope (AMG). Gap closing assay was performed according to standard protocols. In brief, cells were seeded and grown until confluent. A tip was used to generate a gap, cells were washed and conditioned media was added. Images were acquired over time to monitor for gap closure in different conditions. All experiments were performed independently at least twice. Representative experiments are shown.

xCELLigence migration assay. Experiments were performed using the xCELLigence RTCA DP instrument (Roche Diagnostics GmbH) placed in a humidified incubator at 37 °C with 5% CO₂. Cell migration experiments were performed using modified 16-well plates (CIM-16, Roche Diagnostics GmbH) according to the manufacturer's instructions. The experiment was performed twice. A representative experiment is shown.

Animal studies. All experiments using animals were performed in accordance to our protocol approved by MSKCC's Institutional Animal Care and Use Committee (IACUC). 5–7-week-old, female NOD-SCID NCR (NCI) or athymic NCR-NU-NU (NCI) mice were used for animal experiments with human cell lines. Primary YUMM1.1 and YUMM1.7 cell lines were isolated from melanomas developed in mice (*Tyr*:*CreER*; *Braf*^{C4}; *Cdkn2a*^{−/−}; *Pten*^{lox/lox}) treated with 4-hydroxytamoxifen and were subsequently implanted in female C57BL/6 (JAX) mice aged between 5 and 7 weeks. Tumour formation, outgrowth and metastasis were monitored by BLI of TGL-labelled tumour cells as described previously²². In brief, anaesthetized mice (150 mg kg⁻¹ ketamine, 15 mg kg⁻¹ xylazine or isoflurane) were injected retro-orbitally with D-luciferin (150 mg kg⁻¹) and imaged with an IVIS Spectrum Xenogen machine (Caliper Life Sciences). Bioluminescence analysis was performed using Living Image software, version 4.4. For co-implantation assays, mice were anaesthetized (150 mg kg⁻¹ ketamine, 15 mg kg⁻¹ xylazine) and 1 × 10³ TGL-labelled resistant tumour cells were injected subcutaneously with 2 × 10⁶ sensitive tumour cells in 50 µl growth-factor-reduced Matrigel/PBS (1:1) (BD Biosciences). For the control groups in which the effects of drug treatment on resistant cells alone were tested, 2 × 10⁶ resistant cells were injected in growth-factor-reduced Matrigel/PBS. Two-to-four sites on the flanks were injected per mouse. After tumours reached a size of 50–150 mm³, the BLI signal of resistant cells was determined. To compensate for minor growth differences of the GFP⁺ resistant cell population between mice, the mice were assigned to the cohorts so that the overall BLI intensity (and consequently the cell number) was equal in the treatment and control group. Each group received vehicle or drug treatment as indicated (vemurafenib/PLX4032, 25 mg kg⁻¹ twice daily for YUMM1.1 and YUMM1.7 tumours, and 75 mg kg⁻¹ twice daily for all other BRAF mutant tumours, LC-Labs or Selleckchem; 100 mg kg⁻¹ crizotinib once daily, LC-Labs; 50 mg kg⁻¹ erlotinib once daily, LC-Labs; 100 mg kg⁻¹ MK-2206 once daily, Chemietek; 50 mg kg⁻¹ BEZ235 once daily, LC-Labs). Growth of the resistant population in the different groups was monitored by BLI, quantified and normalized to BLI signal at start of treatment. Tumour seeding and metastasis assays were performed as described with minor modifications²⁰. In brief, sensitive tumour cells were injected subcutaneously on two sites per mouse. Once tumours were established (50–150 mm³) mice were treated with vehicle or vemurafenib (75 mg kg⁻¹ twice daily) for 3 days, and 1 × 10⁵ TGL-labelled drug-resistant cells were injected in the left cardiac ventricle. Treatment was continued, and metastatic burden and tumour seeding were determined *in vivo* and *ex vivo* by BLI. Tumour volume was determined using caliper measurements and calculated using the following formula: tumour volume = (D × d²)/2, in which D and d refer to the long and short tumour diameter, respectively. All experiments with A375 cells were independently performed at least three times, except animal experiments in Fig. 3, which were performed twice. All other animal experiments were independently performed at least twice. Representative experiments are shown, except where noted and where instead the average of three experiments is presented.

Gene expression analysis. Whole RNA was isolated from cells using RNAeasy Mini Kit (QIAGEN). The Transcriptor First Strand cDNA synthesis kit (Roche) was used to generate cDNA. Differential RNA levels were assessed using Taqman gene expression assays (Life technologies). Assays used for human genes are: Hs04187685, Hs00365742, Hs00605382, Hs00601975, Hs01099999, Hs00959010, Hs01029057, Hs00234244, Hs00905117, Hs00180842, Hs00989373, Hs00234140, Hs00195591, Hs00207691, Hs99999141, Hs01117294, Mm0607939, Mm9999915 and Mm04207958. Relative gene expression was normalized to internal control genes: *B2M* (Hs9999907_m1), *GAPDH* (Hs9999905_m1) and *ACTB* (Mm0607939_s1). Quantitative PCR reactions were performed on a VIIA7 Real-Time PCR system and analysed using VIIA7 software (Life Technologies). All data points represent at least four technical replicates and experiments were performed independently three times. A representative experiment is shown.

Cancer-cell-specific TRAP and sequencing. To investigate the gene expression changes specifically of drug-sensitive tumours during vemurafenib treatment, or gene expression changes of resistant cells exposed to a regressing tumour microenvironment, A375 and A375^R cells, respectively, were modified to express eGFP-RPL10a. Tumours derived from implanted A375-eGFP-RPL10a and A375^R-eGFP-RPL10a cells were homogenized and processed with the TRAP protocol as previously described^{28,32,33} with the following modifications: fresh tumour was homogenized with a Model PRO 200 homogenizer at speed 5 for four cycles of 15 s, RNasin Plus RNase inhibitor (Promega, N2615) was used as RNase inhibitor, and anti-eGFP antibody coated sepharose beads (GE Healthcare) were used for immunoprecipitation. Polysome-associated RNA was purified with RNAqueous micro kit (Life

Technologies, AM1931). Ribogreen and the Agilent BioAnalyzer technologies were used to quantify and control the quality of RNA; 500 ng RNA (RNA integrity number (RIN) > 8.5) from each sample was used for library construction with TruSeq RNA Sample Prep Kit v2 (Illumina) according to the manufacturer's instructions. The samples were barcoded and run on a Hiseq 2000 platform in a 50-base-pair (bp)/50-bp or 75-bp/75-bp paired-end run, using the TruSeq SBS Kit v3 (Illumina). An average of 40 million paired reads was generated per sample.

RNA-seq analysis. For drug-sensitive A375, Colo800, UACC63 and H3122 cells, *in vitro*, raw paired-end sequencing reads were mapped to the human genome (build hg19) with STAR2.3.0e (ref. 34) using standard options. Uniquely mapped reads were counted for each gene using HTSeq v0.5.4 (ref. 35) with default settings. Read counts of each sample were normalized by library size using the 'DESeq' package of Bioconductor. Differential gene expression analysis between any two conditions was performed based on a model using the negative binomial distribution³⁵. Genes with false discovery rate (FDR) < 0.05, fold change larger than 1.5 or smaller than 0.667-fold, and average read counts larger than 10 were treated as differentially expressed genes. RNA-seq data from *in vivo* xenograft TRAP samples were processed with the following modifications to avoid potential mRNA contamination from host mouse tissue: raw sequencing reads were mapped to a hybrid genome consisting indexes of both human (build hg19) and mouse (build mm9) genomes. Only reads that uniquely mapped to human genome indexes were preserved and counted using HTSeq v0.5.4 (ref. 35).

Bioinformatics analysis. Heatmap visualization of data matrices was performed using the 'gplots' package of R. Principle component analysis of RNA-seq results was performed with the variance stabilizing transformation methods in 'DESeq' package of Bioconductor and the first two principal components were plotted. Volcano plots were derived from 'DESeq'-based differential gene expression analysis. Differentially expressed genes with transcription factor activity (GO:00037000) at 6 h of vemurafenib treatment and gene products located in the extracellular region (GO: 00005576) at 48 h of vemurafenib treatment were identified using the Database for Annotation, Visualization and Integrated Discovery (DAVID)³⁶ v6.7 (<http://david.abcc.ncifcrf.gov/>) and enriched GO terms were visualized using REVIGO³⁷ (<http://revigo.irb.hr>). Enriched transcriptional regulators for the list of differentially expressed gene products in the extracellular region were predicted with DAVID v6.7 and this list compared to the gene expression levels of transcription factors after 6 h of vemurafenib treatment in A375 cells. Upstream regulators, functions associated with the gene expression profile and potential drug vulnerabilities were determined by interpretative phenomenological analysis (IPA) analysis on differentially expressed genes from A375^R-eGFP-RPL10a cells in different tumour microenvironments *in vivo*.

Immunoblotting. RIPA buffer (Cell Signaling) was used for cell lysis, according to the manufacturer's instructions, and the protein concentrations were determined by BCA Protein Assay kit (Pierce). Proteins were separated by SDS-PAGE using Bis-Tris 4–12% gradient polyacrylamide gels in the MOPS buffer system (Invitrogen) and transferred to nitrocellulose membranes (BioRad) according to standard protocols. Membranes were immunoblotted with antibodies against pERK^{T202/Y204} (4370), tERK (4696), pAKT^{S473} (4060), pAKT^{T308} (4056), tAKT (2920), EGFR (4267), MET (8198), PDGFR β (3169), pFRA1 (3880), caspase3 (9662), pPRAS40^{T246} (13175), p70S6K^{T389} (9205), pFAK^{Y397} (3283), pPKC β II^{S660} (9371), pNF κ B^{S536} (3033), p β -Catenin^{S33/37/T41} (9561), pSTAT-3^{Y705} (9145), pSTAT-5^{C11C5} (9359), pGSK3 α / β ^{S219} (9327), pCREB^{S133}/pATF-1 (9196) (Cell Signaling, 1:1,000), FRA1 (sc-605, Santa Cruz Biotechnology, 1:200) and tubulin (T6074, Sigma-Aldrich, 1:5,000) in Odyssey blocking buffer (LI-COR). After primary antibody incubation, membranes were probed with IRDye 800CW donkey-anti-mouse IgG (LI-COR) or IRDye 680RD goat-anti-rabbit IgG (LI-COR) secondary antibody (1:20,000) and imaged using the LI-COR Odyssey system. All immunoblots were performed independently at least twice. Tubulin served as a loading control.

Plasmids, recombinant protein and ELISA. Identifiers for shRNAs used in this study are: V3LHS-644610 (shFRA1-1), V3LHS-644611 (shFRA1-2), V3LHS-320021 (shIGFBP3-1) and V2LHS-111629 (shIGFBP3-2) (Dharmacon, GE Lifesciences). IGFBP3 ELISA (Raybiotech) was performed according to the manufacturer's instructions with 50 μ g tumour lysate and conditioned media was diluted 1:5. Recombinant proteins were used at the following conditions: 10 ng ml⁻¹ IGFI (Invitrogen), 10 ng ml⁻¹ EGF (Invitrogen), 10 ng ml⁻¹ PDGFD (R&D Systems), 2 μ g ml⁻¹ IGFBP3 (Prospec) for 15 min, or 5 μ g ml⁻¹ ANGPTL7 (R&D Systems) for 30 min.

Patient samples. Melanoma tissues were obtained from clinical trial patients or patients under standard clinical management with approval of the UCLA Institutional Review Board. Patient-informed consent was obtained for the research performed in this study.

Immunofluorescence. Tissues for BrdU-immunofluorescence staining were obtained after overnight fixation with 4% paraformaldehyde (PFA) at 4 °C, embedded in OCT compound (VWR) and stored at -80 °C. 10- μ m thick cryosections on glass slides were used for immunofluorescence staining according to standard

protocols. Tissue for all other immunofluorescence experiments from xenograft tumours was obtained after fixation with 4% PFA at 4 °C and a series of dehydration steps from 15% to 30% sucrose, as described previously³⁸. In brief, tumours were sliced using a sliding microtome (Fisher). Tumour slices (80 μ m) were blocked floating in 10% NGS, 2% BSA, 0.25% Triton in PBS for 2 h at room temperature. Primary antibodies were incubated overnight at 4 °C in the blocking solution and the next day for 30 min at room temperature. After washes in PBS-Triton 0.25%, secondary antibodies were added in the blocking solution and incubated for 2 h. After extensive washing in PBS-Triton 0.25%, nuclei were stained with Bis-Benzamide for 5 min at room temperature, tumour slices were washed and transferred to glass slides. Slices were mounted with ProLong Gold anti-fade reagent (Invitrogen). Primary antibodies: GFP (GFP-1020, Aves Labs, 1:1,000), collagen IV (AP756, Millipore, 1:500), BrdU (ab6326, Abcam, 1:250), FRA1 (sc605, Santa Cruz, 1:200). Secondary antibodies: Alexa-Fluor-488 anti-chicken, Alexa-Fluor-555 anti-rabbit, Alexa-Fluor-555 anti-rat (Invitrogen). Stained sections were visualized using a Carl Zeiss Axioimager Z1 microscope or with a Leica SP5 upright confocal microscope using \times 10 or \times 20 objectives. Images were analysed with ImageJ, and Metamorph software.

Flow cytometry. Flow cytometry was performed as described previously²², with minor modifications. In brief, whole tumours were dissected, cut into smaller sections and dissociated for 1–3 h with 0.5% collagenase type III (Worthington Biochemical) and 1% dispase II (Roche) in PBS. Resulting single cell suspensions were washed with PBS supplemented with 2% FBS and filtered through a 70- μ m nylon mesh. The resulting single cell suspension was incubated for 10 min at 4 °C with anti-mouse Fc-block CD16/32 antibody (2.4G2 BD) in PBS supplemented with 1% BSA. Cells were subsequently washed with PBS/BSA and stained with control antibodies or antibodies to detect immune cells diluted in PBS supplemented with 0.5% BSA and 2 mM EDTA. The following antibodies against mouse antigens were used: CD45-PE-Cy7 (clone 30-F11, BD Pharmingen, 1:200), CD11b-APC (clone: M1/70, BD Pharmingen, 1:100), Gr1-PE (MACS, 1:10), CD31-APC (clone: 390, eBioscience, 1:100), F4/80-PE (clone: BM8, eBioscience, 1:50). To determine the level of EdU incorporation in A375^R cells within vehicle- or vemurafenib-treated A375/A375^R tumours, EdU (50 mg kg⁻¹, Life Technologies) was injected intraperitoneally, after 2 h tumours were collected, single-cell suspensions generated as described above and further processed according to the manufacturer's protocol (Click-iT Plus EdU Alexa Fluor 647 Flow Cytometry Assay Kit, Life Technologies). Data were acquired using a FACS Calibur (BD Biosciences). All experiments were performed independently at least two times. Representative experiments are shown.

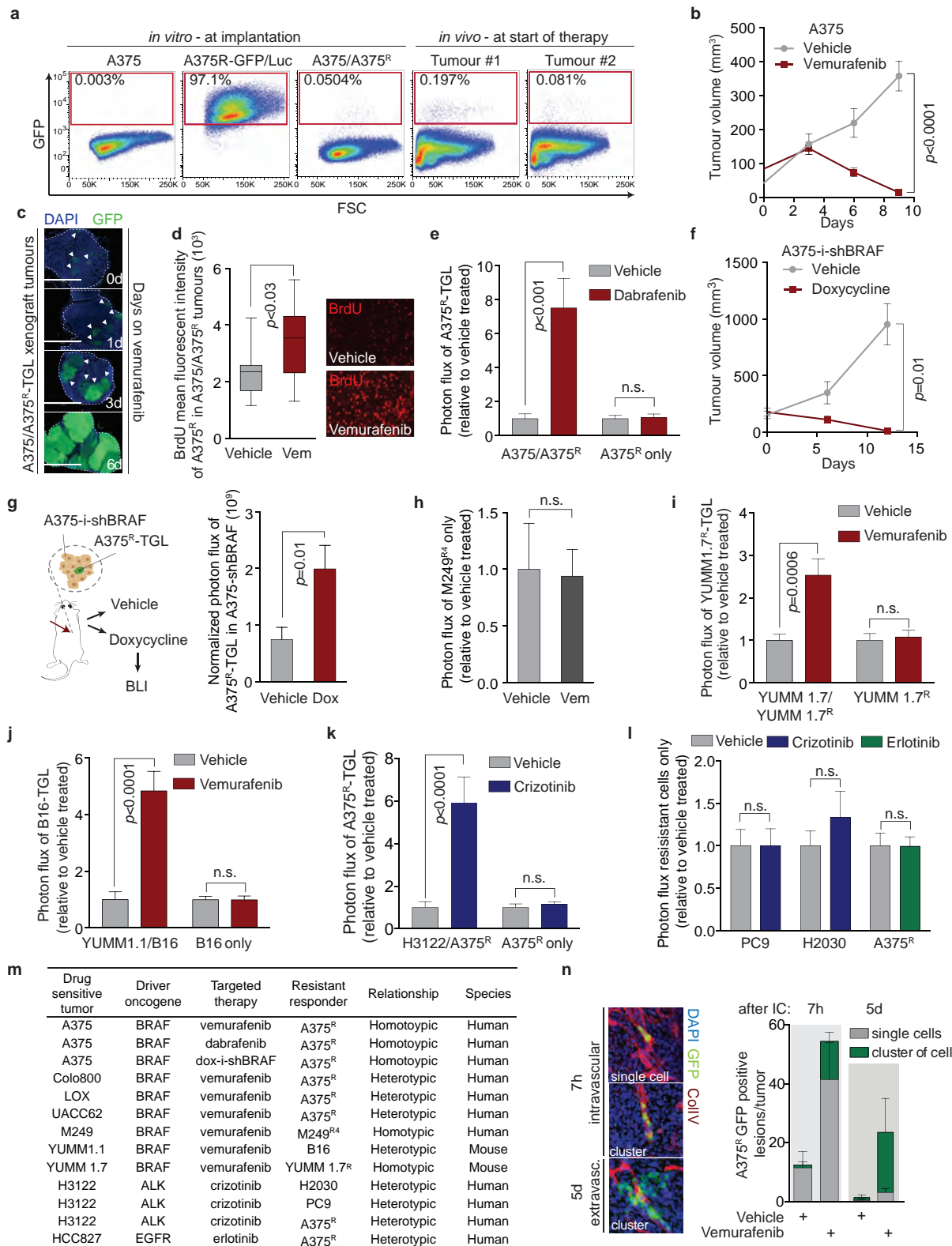
Antibody arrays. Cytokines and cytokine receptors of murine stromal and immune cells, in A375 tumours treated with vehicle or vemurafenib for 5 days, were measured using the Mouse Cytokine Array G2000 (RayBio, AAH-CYT-G2000-8, detecting 174 proteins), according to the recommended protocols. In brief, tumours were homogenized with a Mini Immersion Blender (Pro Scientific) in Raybio Lysis buffer with protease inhibitors. Lysates were centrifuged for 5 min at 10,000g, the supernatant was collected and protein concentration was measured using the BCA Assay Kit (Pierce). Protein (150 μ g) was hybridized on the antibody arrays overnight at 4 °C. IRDye-labelled streptavidin (LI-COR) at a dilution of 1:5,000 was used for the detection, slides were scanned using an Odyssey CLx scanner (LI-COR) and analysed using Image Studio 2.0 software. The results were then normalized using internal controls, and the relative protein levels determined across four biological replicates.

Senescence β -galactosidase staining. A375 cells were grown in low-serum media and treated with vehicle or vemurafenib (0.1 μ M) for 3 or 8 days, β -galactosidase staining was performed according to the manufacturer's instructions (Cell Signaling). All experiments were performed independently three times. Representative experiments are shown.

Statistical analysis. Data are generally expressed as mean \pm s.e.m., or in box plots in which the centre line is the median, and whiskers are minimum to maximum values. Group sizes were determined based on the results of preliminary experiments and no statistical method was used to predetermine sample size. Group allocation and outcome assessment were not performed in a blinded manner. All samples that met proper experimental conditions were included in the analysis. Statistical significance was determined using a two-tailed Mann-Whitney *U* test or Student's *t*-test using Prism 6 software (GraphPad Software), or using a hypergeometric variability test (<http://www.geneprof.org>). Significance was set at $P < 0.05$.

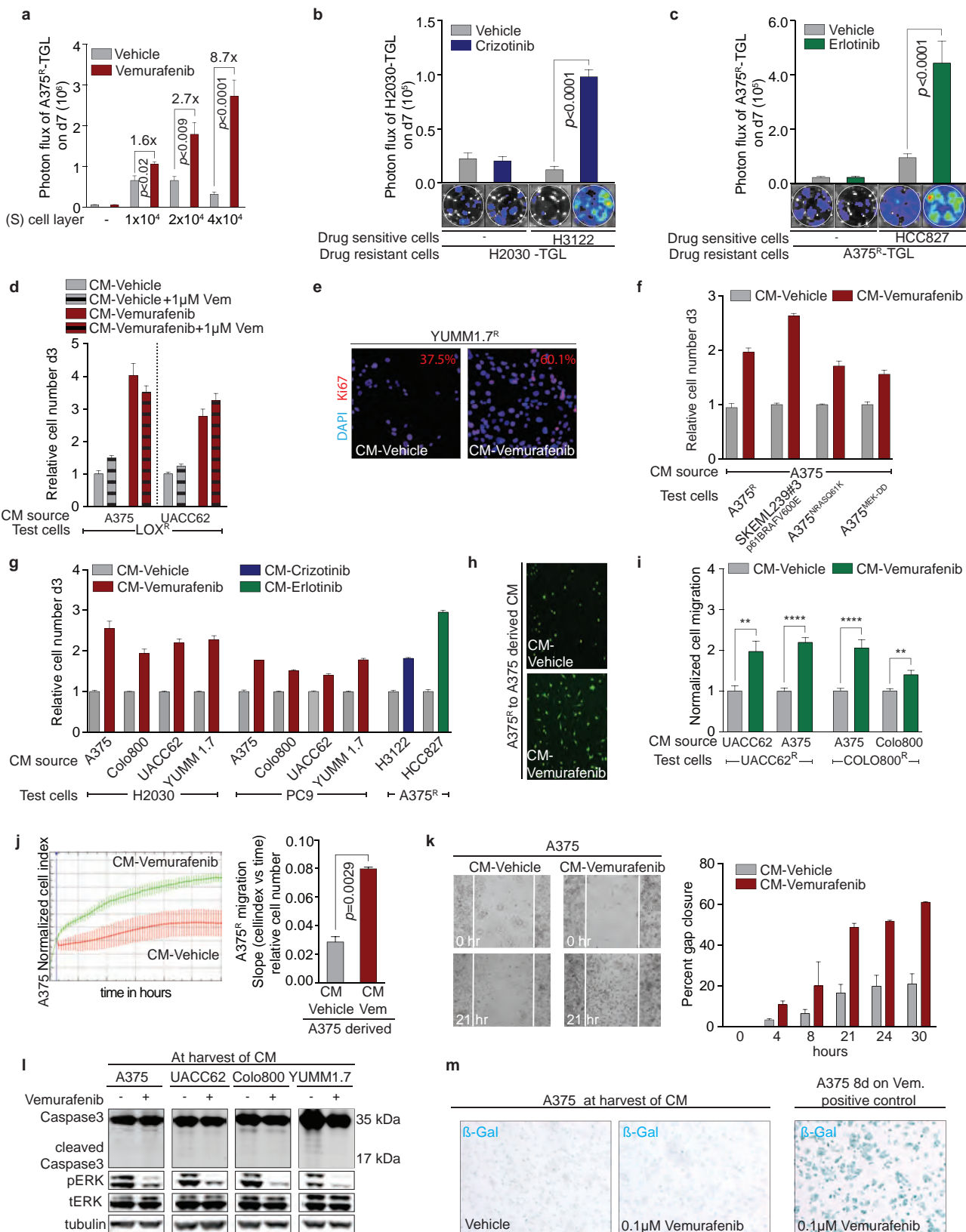
1. Tavazoie, S. F. *et al.* Endogenous human microRNAs that suppress breast cancer metastasis. *Nature* **451**, 147–152 (2008).
2. Doyle, J. P. *et al.* Application of a translational profiling approach for the comparative analysis of CNS cell types. *Cell* **135**, 749–762 (2008).
3. Zhang, X. H. *et al.* Selection of bone metastasis seeds by mesenchymal signals in the primary tumor stroma. *Cell* **154**, 1060–1073 (2013).
4. Dobin, A. *et al.* STAR: ultrafast universal RNA-seq aligner. *Bioinformatics* **29**, 15–21 (2013).

35. Anders, S. & Huber, W. Differential expression analysis for sequence count data. *Genome Biol.* **11**, R106 (2010).
36. Huang da, W., Sherman, B. T. & Lempicki, R. A. Systematic and integrative analysis of large gene lists using DAVID bioinformatics resources. *Nature Protocols* **4**, 44–57 (2009).
37. Supek, F., Bosnjak, M., Skunca, N. & Smuc, T. REVIGO summarizes and visualizes long lists of gene ontology terms. *PLoS ONE* **6**, e21800 (2011).
38. Valiente, M. et al. Serpins promote cancer cell survival and vascular co-option in brain metastasis. *Cell* **156**, 1002–1016 (2014).



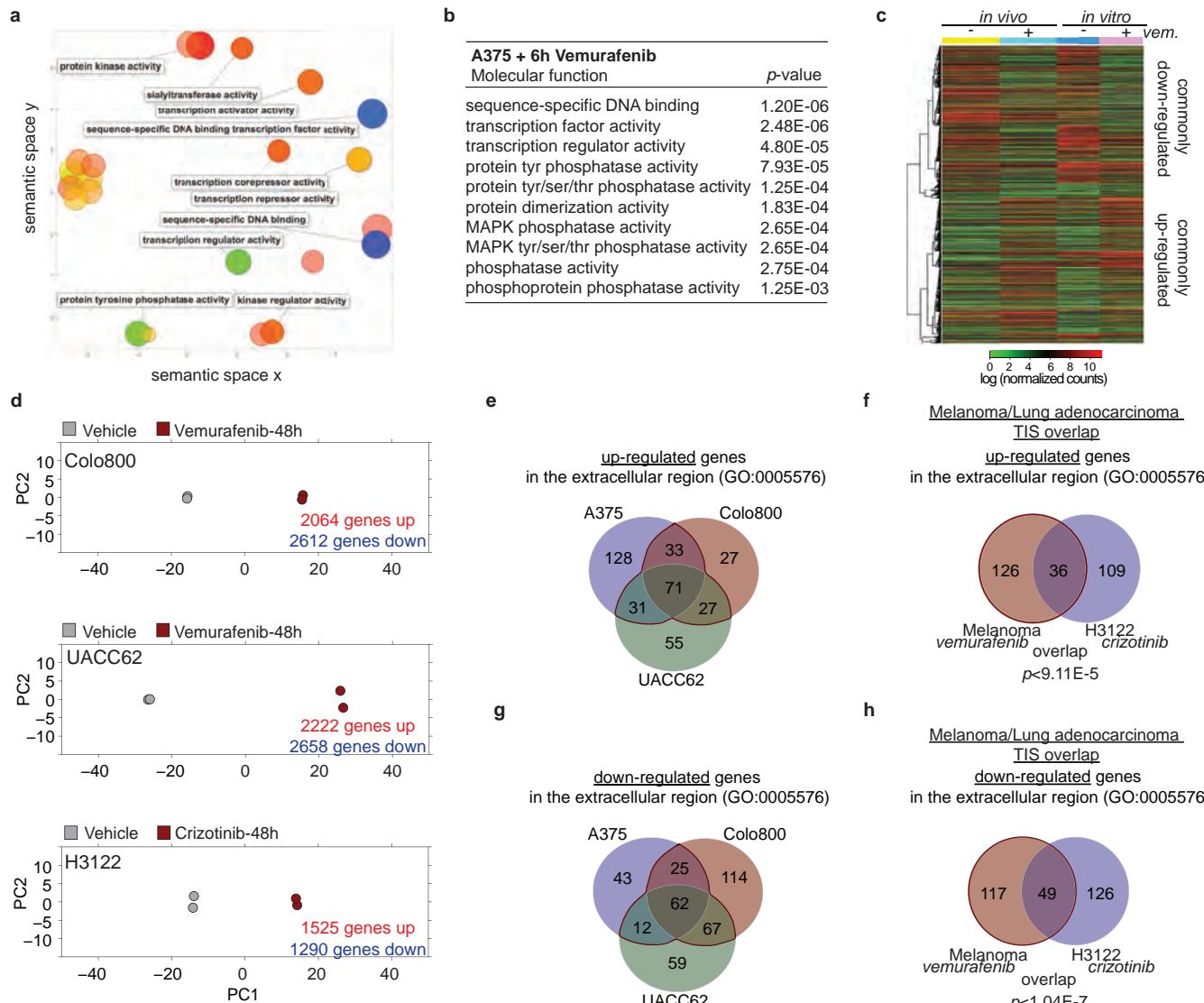
Extended Data Figure 1 | Targeted therapy or oncogene knockdown leads to regression of sensitive melanoma and lung adenocarcinoma tumours but accelerates the proliferation and seeding of residual drug-resistant cells *in vivo*. **a**, FACS analysis of sensitive A375 and vemurafenib-resistant A375^R cells expressing TGL, at tumour implantation and after 2 weeks at start of therapy ($n = 8$ tumours). Plots depict representative images. **b**, Tumour volume of A375 cells treated with vehicle or vemurafenib over time (vehicle, $n = 8$; vemurafenib, $n = 12$ tumours). **c**, Representative sections of A375/A375-TGL tumours at 0, 1, 3 and 6 days of vemurafenib treatment analysed with immunofluorescence against GFP. Arrowheads indicate emerging clusters of GFP⁺ resistant cells. Scale bars, 2 mm. **d**, Quantification of BrdU incorporation into vemurafenib-resistant A375^R-TGL cells in A375/A375^R tumours treated with vehicle or vemurafenib for 6 days (vehicle, $n = 13$ FOV of 3 tumours; vemurafenib $n = 18$ FOV of 4 tumours). Original magnification, $\times 20$. **e**, Fold change of photon flux of TGL-expressing A375^R cells in A375 tumours or A375^R tumours alone treated with vehicle or dabrafenib for 8 days (A375/A375^R: vehicle, $n = 15$; dabrafenib, $n = 14$; A375^R: vehicle, $n = 8$; dabrafenib, $n = 7$ tumours). **f**, Tumour volume of doxycycline-inducible BRAF knockdown A375-i-shBRAF-derived xenograft tumours (in which 'A375-i' denotes expression of doxycycline-inducible hairpin) treated with vehicle or doxycycline over time (vehicle, $n = 5$; doxycycline, $n = 4$ tumours). **g**, Photon flux of TGL-expressing A375^R cells mixed in A375-i-shBRAF tumours treated with vehicle or doxycycline (vehicle, $n = 10$; doxycycline, $n = 11$ tumours). **h**, Fold change of photon flux of TGL-expressing vemurafenib-resistant M249^{R4} tumours treated with vehicle or vemurafenib ($n = 16$ tumours).

i–k, Co-implantation assay of tumours treated with vehicle or corresponding targeted therapy with BLI quantification after 5–8 days. **i**, Fold change of photon flux of TGL-expressing vemurafenib-resistant YUMM1.7^R cells mixed in unlabelled, vemurafenib-sensitive YUMM1.7 tumours or YUMM1.7^R tumours alone (YUMM1.7/YUMM1.7^R: $n = 24$; YUMM1.7^R: $n = 20$ tumours). **j**, Fold change of photon flux of TGL-expressing, intrinsically vemurafenib-resistant B16 cells mixed in vemurafenib-sensitive YUMM1.1 tumours or B16 tumours alone (YUMM1.1/B16: vehicle, $n = 12$; vemurafenib, $n = 16$; B16: $n = 20$ tumours). **k**, A375^R mixed in crizotinib-sensitive H3122 cells or A375^R tumours alone (H3122/A375^R: vehicle, $n = 14$; crizotinib, $n = 13$; A375^R: $n = 12$ tumours). **l**, Photon flux of tumours established from intrinsically resistant drug-resistant cells alone, treated with vehicle, crizotinib or erlotinib (crizotinib-resistant PC9, H2030- or erlotinib-resistant A375^R) (n (from left to right) = 12, 12, 7, 12, 16 and 16 tumours, respectively). **m**, Summary of the model systems and conditions used *in vivo*. **n**, Left, representative immunofluorescence images of vemurafenib-treated, sensitive tumours 7 h or 5 days after intracardiac injection with A375^R-TGL cells; sections stained for GFP (A375^R, green), collagen type IV (blood vessels, red), and DAPI (nuclei, blue). Right, quantification of A375^R single cells and cell clusters (≥ 2 cells) infiltrating an A375 tumour treated with vehicle or vemurafenib after intracardiac injection of A375^R cells (GFP⁺ cells were scored in at least 10 whole sections of at least 4 tumours). Original magnifications, $\times 20$. Data in **b**, **e–l** and **n** are mean and s.e.m., in **f**, centre line is median, whiskers are minimum to maximum. *P* values calculated by a two-tailed Mann–Whitney *U* test.



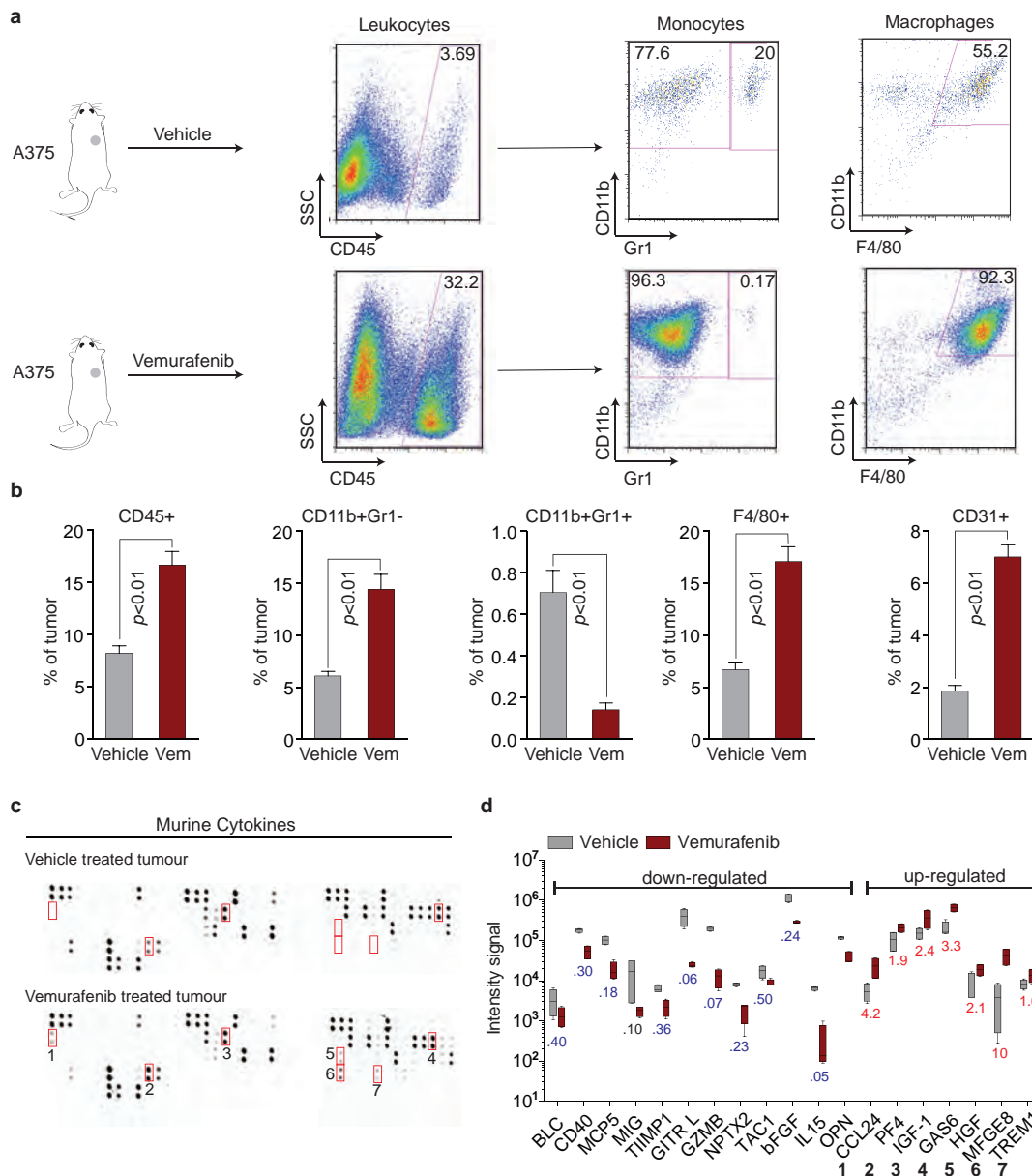
Extended Data Figure 2 | The secretome of vemurafenib-treated melanoma and crizotinib- or erlotinib-treated lung adenocarcinoma cells stimulates the proliferation and migration of drug-resistant cells *in vitro* and occurs before apoptosis and senescence. **a**, Quantification of the co-culture assay, depicted in Fig. 2a, 7 days after addition of resistant A375^R-TGL cells ($n = 4$ biological replicates). P values calculated using a Student's t -test. **b, c**, Drug-sensitive cells were pre-treated with vehicle or drug (crizotinib or erlotinib) for 48 h before 5×10^2 TGL-expressing, drug-resistant cells were added. Growth was monitored by BLI and quantified 7 days after addition of the resistant cell population ($n = 8$ biological replicates), P values calculated using a Student's t -test. **b**, Quantification and representative images of TGL-expressing H2030 cells alone or co-cultured with crizotinib-sensitive H3122 cells and treated with vehicle or crizotinib **c**, Quantification and representative images of TGL-expressing A375^R cells alone or co-cultured with erlotinib-sensitive HCC827 cells and treated with vehicle or erlotinib. **d**, Relative number of vemurafenib-resistant LOX^R cells after 3 days in the presence of conditioned media derived from A375 and UACC62 cells ($n = 3$ biological replicates). **e**, Representative immunofluorescence for Ki67 in drug-resistant YUMM1.7 cells cultured in conditioned media from YUMM1.7 cells. Original magnification, $\times 20$. **f**, Relative number of vemurafenib-resistant melanoma cells with different, clinically relevant resistance mechanisms after 3 days in the presence of conditioned media derived from A375 cells. SKMEL239-3 expressing the p61 BRAFV600E splice variant, A375 expressing NRAS^{Q61K} or

the constitutively active MEK variant MEK-DD ($n = 5$ biological replicates). **g**, Relative cell number of intrinsically vemurafenib-resistant lung adenocarcinoma cells (H2030, PC9) or crizotinib- and erlotinib-resistant melanoma cells (A375^R) after 3 days cultured in the presence of conditioned media from vemurafenib-treated melanoma or crizotinib- and erlotinib-treated lung adenocarcinoma ($n = 6$ in all, except for A375^R with HCC827-CM, $n = 4$ biological replicates). **h**, Representative image of A375^R cells migrated towards A375-derived CM-vehicle or CM-vemurafenib. Original magnification, $\times 10$. **i**, Relative migration towards conditioned media from different sources and different resistant test cells as indicated ($n = 10$ FOV). $**P < 0.01$, $****P < 0.0001$, two-tailed Mann-Whitney U test. **j**, Representative graph and quantification of real-time migration of A375^R cells in the presence of conditioned media derived from A375 cells as measured by the xCELLigence system ($n = 4$ biological replicates). P value calculated using two-tailed Mann-Whitney U test. **k**, Monolayer gap closing assay of A375^R cells in the presence of conditioned media derived from A375 cells with representative light microscopy images and quantification of gap closure over time. **l**, Immunoblotting for cleaved caspase-3 and phosphorylated ERK protein levels in vemurafenib-sensitive melanoma cell lines after 72 h of vemurafenib treatment. **m**, β -galactosidase staining of A375 cells treated with vemurafenib for 72 h or 8 days. Original magnification, $\times 13$. Data are presented mean and s.e.m.



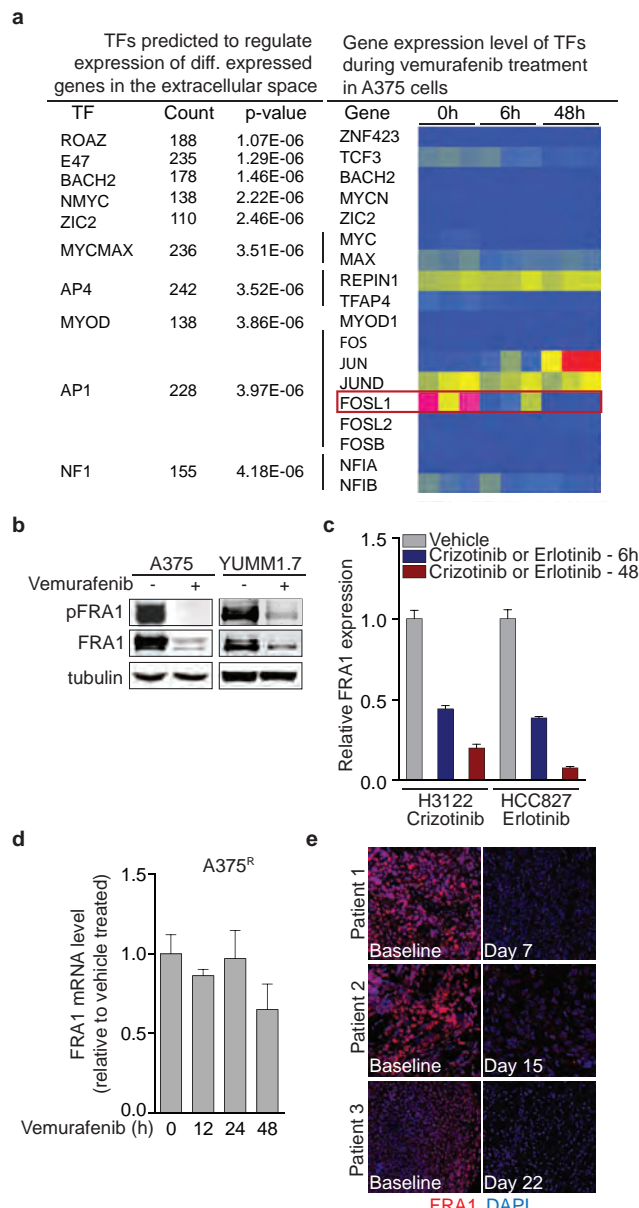
Extended Data Figure 3 | The therapy-induced secretome of sensitive cells overlaps significantly in melanoma and lung adenocarcinoma cells and appears after gene expression changes enriched for transcriptional regulators. **a, b**, GO analysis (<http://revigo.irb.hr>) of gene expression changes after 6 h of vemurafenib treatment of A375 cells with spatial representation of enriched GO terms (**a**) and the molecular functions significantly affected (**b**). **c**, Heat map representing the expression levels of commonly up- and downregulated genes in vemurafenib-treated A375-derived xenograft tumours (5 days) and A375 cells *in vitro* (48 h). **d**, Principal component analysis of vemurafenib-sensitive Colo800 and UACC62 melanoma cells and crizotinib-sensitive H3122 lung adenocarcinoma cells treated *in vitro* with vehicle or vemurafenib or crizotinib for 48 h. **e**, Venn diagram indicating the overlap of genes in the extracellular region (GO:0005576) upregulated after 48 h of

vemurafenib treatment in A375, Colo800 and UACC62 melanoma cell lines. **f**, Venn diagram indicating the overlap of genes in the extracellular region (GO:0005576) upregulated after 48 h of vemurafenib treatment in at least 2 out of 3 melanoma models and after 48 h of crizotinib treatment in the H3122 lung adenocarcinoma cell line. **g**, Venn diagram indicating the overlap of genes in the extracellular region (GO:0005576) downregulated after 48 h of vemurafenib treatment in A375, Colo800 and UACC62 melanoma cell lines. **h**, Venn diagram indicating the overlap of genes in the extracellular region (GO:0005576) downregulated after 48 h of vemurafenib treatment in at least 2 out of 3 melanoma models and after 48 h of crizotinib treatment in the H3122 lung adenocarcinoma cell line. *P* values calculated using a hypergeometric probability test.



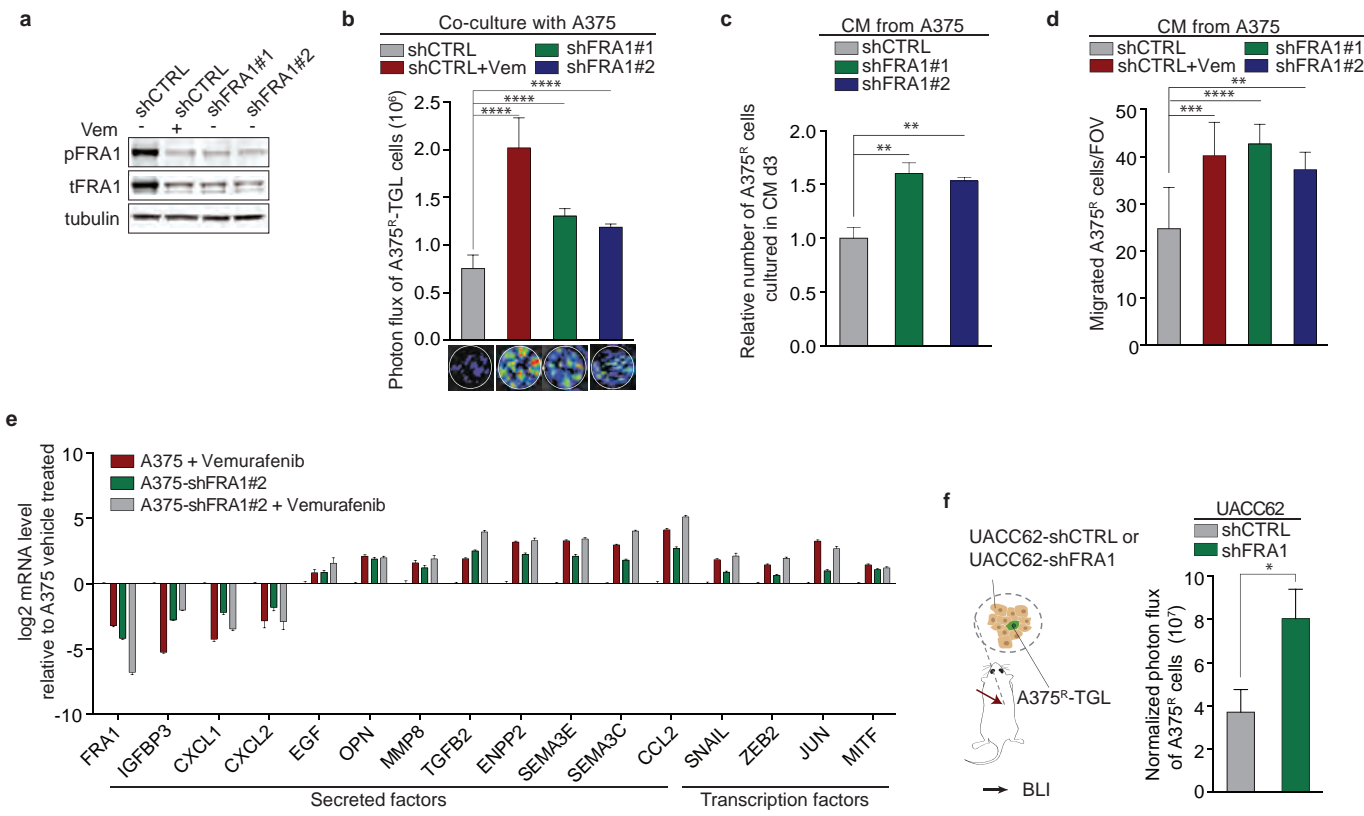
Extended Data Figure 4 | Vemurafenib treatment induces widespread changes in the intra-tumour immune cell composition and stromal cytokine composition in tumours regressing during targeted therapy. **a, b**, FACS analysis of murine immune cell populations in A375-derived xenograft tumours treated with vehicle or vemurafenib for 5 days. **a, b**, Representative image (**a**) and quantification (**b**) of intra-tumour composition of indicated

immune cell populations (vehicle, $n = 4$; vemurafenib, $n = 6$ tumours). **c, d**, Cytokine array of murine stroma-derived cytokines within A375-derived xenograft tumours treated with vehicle or vemurafenib for 5 days. Representative image (**c**) and quantification (**d**) of down- and upregulated cytokines ($n = 4$ tumours). P values calculated by a two-tailed Mann-Whitney U test. Data are mean and s.e.m.



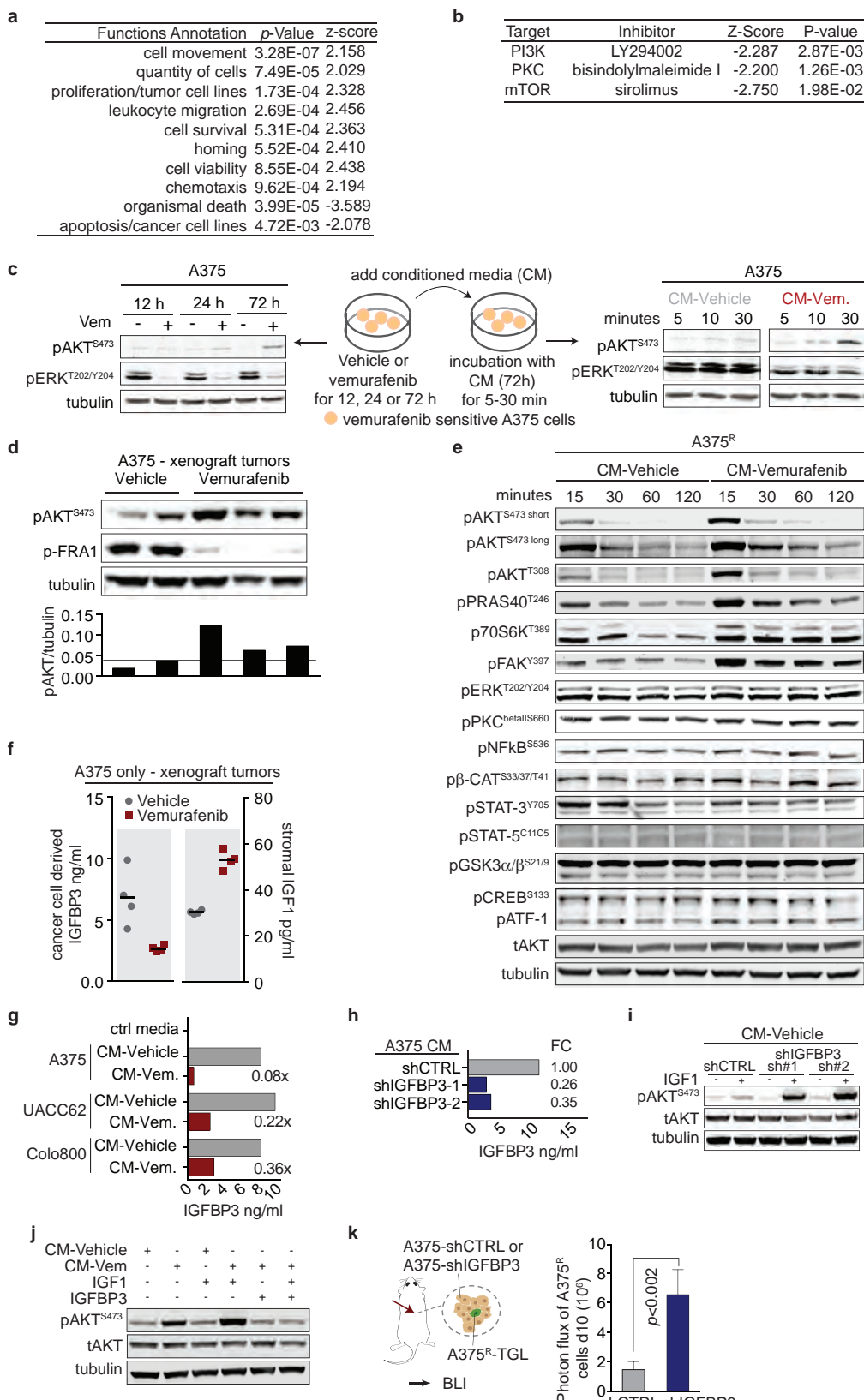
Extended Data Figure 5 | Targeted therapy induces downregulation of FRA1 in drug-sensitive tumour cells. **a**, List of transcription factors predicted to regulate the vemurafenib-induced reactive secretome in A375 cells, and a heat map of the corresponding transcription factor gene expression levels in these cells. Red represents high, yellow medium and blue low relative expression on the colour scale. **b**, Immunoblotting of phosphorylated and total FRA1 protein levels in A375 and YUMM1.7 melanoma cell lines treated with vemurafenib for 24 h. **c**, Relative mRNA levels of *FRA1* in H3122 cells

treated with crizotinib (500 nM) and HCC827 treated with erlotinib (10 nM) at different time points ($n = 4$ technical replicates). **d**, Relative mRNA levels of *FRA1* in A375^R cells treated with vemurafenib at different time points ($n = 4$ technical replicates). **e**, Immunofluorescence staining of FRA1 (red) and DAPI (blue) in biopsies from melanoma patients before and after vemurafenib treatment (clinical information can be found in Extended Data Table 1). Original magnification, $\times 20$.



Extended Data Figure 6 | The secretome of melanoma cells with FRA1 knockdown stimulates proliferation and migration of A375^R cells in vitro and in vivo. **a**, Immunoblotting of phosphorylated and total FRA1 protein levels in A375 cells transduced with control shRNA, with or without additional vemurafenib treatment, or shRNAs targeting FRA1. **b**, Photon flux and representative BLI images of TGL-expressing A375^R cells co-cultured with A375 cells expressing control shRNA (with or without vemurafenib treatment) or FRA1-targeting shRNAs after 7 days ($n = 9$ biological replicates). **c**, Relative number of A375^R cells after 3 days in the presence of conditioned media derived from A375 cells transduced with control shRNA, with or without additional vemurafenib treatment, or FRA1 shRNAs ($n = 3$ biological replicates).

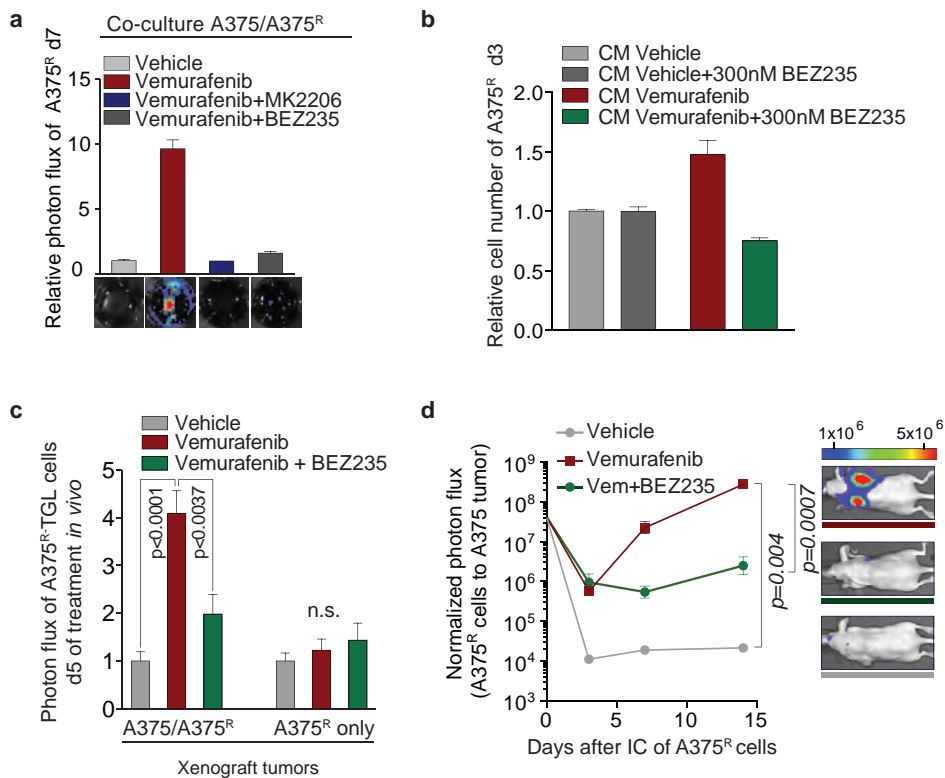
d, Migration of A375^R cells towards conditioned media derived from A375 cells transduced with control shRNA (with or without vemurafenib treatment) or FRA1 shRNAs using a Boyden chamber assay (shCtrl, $n = 15$; all other groups $n = 10$ FOV). **e**, Relative mRNA levels of selected secreted factors and transcription factors of A375 cells expressing control shRNA or an shRNA targeting FRA1 (shFRA1-1), treated with vehicle or vemurafenib (24 h). **f**, Bioluminescent signal of A375^R-TGL cells 8 days after subcutaneous co-implantation with UACC62 cells expressing a control or an shRNA for FRA1 (shCtrl, $n = 12$; shFRA1, $n = 20$ tumours). Data are mean and s.e.m. * $P < 0.05$, ** $P < 0.01$, *** $P < 0.001$, **** $P < 0.0001$, Student's *t*-test.



Extended Data Figure 7 | The TIS includes upregulated positive regulators and a loss of negative regulators of the PI(3)K/AKT/mTOR pathway, which is activated in sensitive and resistant cells *in vitro* and *in vivo*.

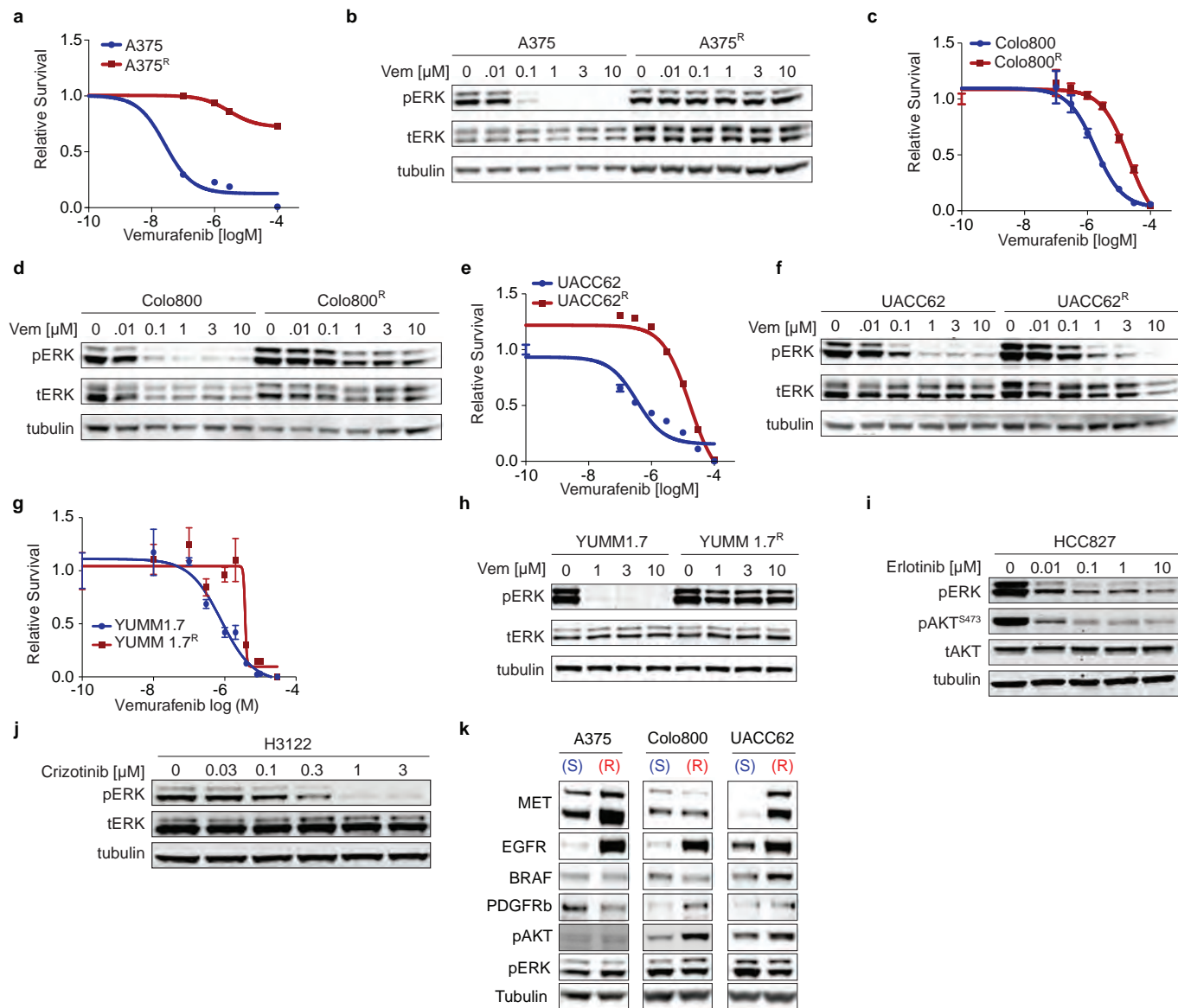
a, b, Enriched biological processes (a) and inferred drug vulnerabilities (b) as determined by Ingenuity pathway analysis of gene expression data from vemurafenib-resistant A375^R cells responding to signals from the reactive tumour microenvironment of a tumour regressing during targeted therapy *in vivo* (for experimental set-up see Fig. 1a and Methods). **c**, Left, immunoblotting of phosphorylated AKT^{S473} and phosphorylated ERK protein levels in A375 cells treated with vehicle or vemurafenib at different time points during the generation of conditioned media. Right, immunoblotting of phosphorylated AKT^{S473} and phosphorylated ERK protein levels in A375 cells after short-term exposure to conditioned media derived from A375 cells treated with vehicle or vemurafenib. **d**, Immunoblotting of phosphorylated AKT^{S473} and phosphorylated FRA1 protein levels in A375-derived xenograft tumours treated with vehicle or vemurafenib for 5 days. Normalized quantification of phospho-AKT^{S473}/tubulin in the bottom panel. **e**, Immunoblotting of a range of pathway nodes in A375^R cells treated with

CM-vehicle or CM-vemurafenib, derived from A375 cells, for 15, 30, 60 or 120 min. **f**, Cancer cell-derived IGFBP3 levels (left) and murine stromal IGF1 levels (right) in A375-derived xenograft tumours treated with vehicle or vemurafenib for 5 days as determined by ELISA ($n = 4$ tumours). **g**, Cancer-cell-derived IGFBP3 levels in conditioned media from indicated melanoma cell lines treated with vehicle or vemurafenib as determined by ELISA ($n = 3$ technical replicates of conditioned media derived from at least two biological replicates). **h**, IGFBP3 levels in conditioned media derived from A375 cells expressing control shRNA or shRNAs targeting *IGFBP3* (shIGFBP3-1 and -2) as determined by ELISA ($n = 3$ technical replicates). **i**, Immunoblotting of phosphorylated AKT^{S473} in A375^R cells after incubation with conditioned media of A375 cells expressing control shRNA or shRNAs targeting *IGFBP3*. **j**, Phosphorylation status of AKT^{S473} in A375^R cells after incubation for 15 min with conditioned media, IGF1 and IGFBP3 as indicated. **k**, Bioluminescent signal of A375^R-TGL cells 10 days after co-implantation with A375 cells expressing a control shRNA or an shRNA targeting *IGFBP3* (shIGFBP3-1) ($n = 10$ tumours). *P* values calculated by a two-tailed Mann-Whitney *U* test. Data are mean and s.e.m.



Extended Data Figure 8 | Dual inhibition of RAF and the AKT/mTOR pathway blunts the effects of the regressing tumour environment on the resistant cell population. **a**, Relative photon flux and representative BLI images of GFP/luciferase expressing A375^R cells co-cultured with A375 cells and treated with vehicle, vemurafenib or the combination of vemurafenib and either MK2206 (AKTi, 2 μ M) or BEZ235 (PI(3)K/mTORi, 300 nM) for 7 days ($n = 2$ –3 biological replicates). **b**, Relative number of A375^R cells after 3 days in the presence of CM-vehicle or CM-vemurafenib with additional BEZ235 (300 nM) ($n = 3$ biological replicates). **c**, Mice bearing tumours consisting of A375/A375^R cells or A375^R cells alone were treated with drugs as indicated.

Bioluminescent signal of TGL-expressing A375^R cells was determined on day 5 of treatment ($n = 16, 16, 12, 12, 12$ and 16 tumours, respectively). **d**, Mice bearing tumours consisting of unlabelled A375 cells were pre-treated for 3 days with drugs as indicated and 1×10^5 TGL-expressing A375^R cells were inoculated in the arterial circulation. Drug treatment was continued and seeding of resistant cells to the primary tumour was quantified by BLI. Representative BLI images on the right (vehicle, $n = 4$; vemurafenib $n = 10$, vemurafenib plus BEZ235, $n = 10$ tumours). P values calculated by a two-tailed Mann-Whitney test. Data are mean and s.e.m.



Extended Data Figure 9 | Characterization of cell lines in response to targeted therapy. **a-h**, Relative survival of human melanoma cell lines (A375, Colo800 and UACC62) (**a, c, e**), and the murine melanoma cell line YUMM1.7 (**g**) and corresponding vemurafenib-resistant derivatives (A375^R, Colo800^R, UACC62^R and YUMM1.7^R) under increasing concentrations of vemurafenib. Immunoblotting of phosphorylated ERK protein levels in indicated melanoma cell lines in the presence of increasing concentrations of vemurafenib (**b, d, f, h**). **i**, Immunoblotting of phosphorylated ERK and

phosphorylated AKT^{S473} protein levels in HCC827 lung adenocarcinoma cells in the presence of increasing concentrations of erlotinib. **j**, Immunoblotting of phosphorylated ERK protein levels in H3122 lung adenocarcinoma cells in the presence of increasing concentrations of crizotinib. **k**, Immunoblotting of protein levels of MET, EGFR, BRAF, PDGFRb, phosphorylated AKT and phosphorylated ERK in vemurafenib-sensitive and -resistant pairs of human melanoma cell lines (A375, Colo800 and UACC62).

Extended Data Table 1 | Clinical data for tissue donor subjects

Study site	Pt #	Bx samples	Age & Sex	Stage	Dose (mg)	BOR	PFS (days)	Bx site
UCLA	1 TG	Baseline Day 7	51M	M1c	960 bid vemurafenib	-21%	108	SC, scalp SC, scalp
	2 JCC	Baseline Day 15	44M	M1c	960 bid vemurafenib +60 qd cobimetinib	-63%	Current response	SC, abdomen SC, abdomen
	3 YAU	Baseline Day 22	26F	M1c	960 bid vemurafenib +60 qd cobimetinib	-46%	145	Dermal/SC, abdomen Dermal/SC, clavicle

bid, twice daily; BOR, best overall response; Bx, biopsy; F, female; M, male; PFS, progression-free survival; Pt, patient; qd, daily; SC, subcutaneous; UCLA, University of California, Los Angeles.